

Synthesis and spectral properties of picenes  
incorporating electron-withdrawing  
functionalities and their application to  
n-type field-effect transistors

2021, 03

Yuxin Guo

The graduate School of  
Natural Science and Technology  
(Doctor Course)  
OKAYAMA University



Synthesis and spectral properties of picenes  
incorporating electron-withdrawing  
functionalities and their application to  
n-type field-effect transistors

2021, 03

Yuxin Guo

The graduate School of  
Natural Science and Technology  
(Doctor Course)  
OKAYAMA University



# Contents

Summary .....	1
Chapter 1 .....	3
1.1 Background of Organic Field-Effect Transistors .....	4
1.1.1 Operation Theory of OFET .....	4
1.1.2 Molecular packing .....	6
1.2 Typical Small Molecule Semiconductor .....	7
1.2.1 Conventional p-type small molecular organic semiconductors .....	7
1.2.2 Conventional n-type small molecular organic semiconductors .....	14
1.3 References .....	19
Chapter 2 .....	25
2.1 Introduction .....	26
2.2 Results and Discussions .....	31
2.2.1 Synthesis of <b>C<sub>n</sub>-PicDI</b> s .....	31
2.2.2 Electronic spectra in solution and crystalline states .....	33
2.2.3 Theoretical analysis for the electronic features .....	37
2.2.4 Structures and electronic properties of <b>C<sub>n</sub>-PicDI</b> s in thin films .....	38
2.2.5 FET characteristics of <b>C<sub>n</sub>-PicDI</b> s .....	42
2.3 Conclusion .....	51
2.4 Experimental Section .....	52
2.5 References .....	57
Chapter 3 .....	61
3.1 Introduction .....	62
3.2 Results and Discussions .....	67
3.2.1 Synthesis of ester-substituted picene .....	67
3.2.2 Electronic spectra in solution and crystalline states .....	70
3.2.3 Theoretical analysis for the electronic features .....	73

3.3 FET characteristics.....	80
3.4 Conclusion .....	83
3.5 Experimental Section .....	84
3.6 References.....	87
List of publications .....	89
Acknowledgements.....	91
Appendix.....	93

## Summary

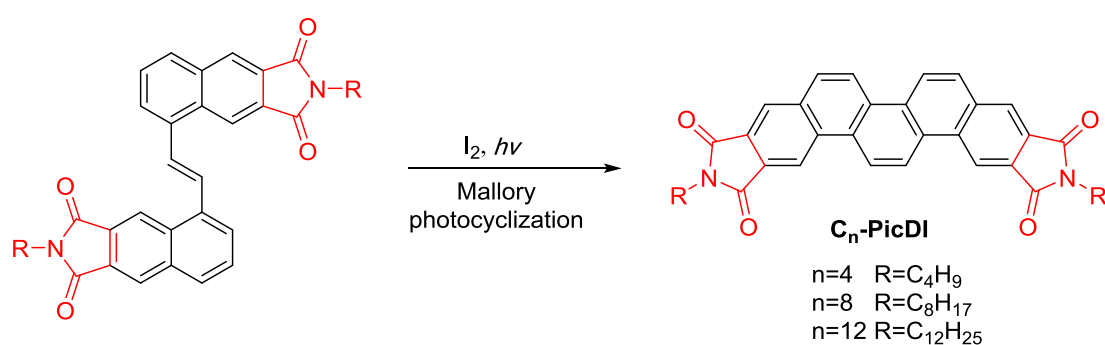
Organic semiconductors have attracted much attention because they can be used in various electronic devices, such as field-effect transistors, photovoltaics, and light-emitting devices. Despite the promising properties of picene and its derivatives towards organic field-effect transistors (OFETs), their use in the devices was limited due to inefficient synthetic routes and molecular design. Through many challenges for constructing high-performance organic semiconductors, it is currently highly desired to develop n-type and ambipolar organic semiconductors because they enable complementary electronic logic circuits.

The aim of the present studies is to synthesize novel n-type and ambipolar organic semiconductor molecules by utilizing the picene  $\pi$  electronic core.

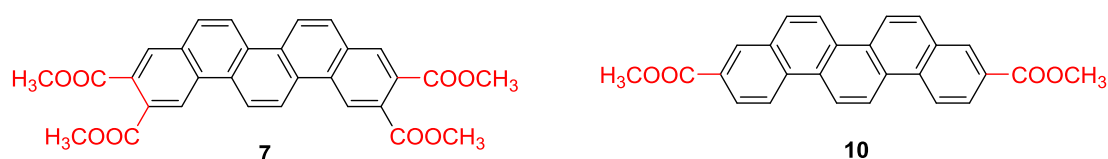
**In chapter 1**, current background into the organic field-effect transistors (FET) including FET operation mechanisms, conventional small molecule organic semiconductor molecules described. Additionally, development of OFETs based on [n]phenacenes, and representative recent synthetic methods of [n]phenacenes are summarized.

**In chapter 2**, in order to construct picene derivatives which serve as n-type organic semiconductors, a series of diimide-substituted picene **C<sub>n</sub>-PicDI**s were designed. Dinaphthylethenes having electron-withdrawing imide functionalities are synthesized as the precursors to the desired functionalized picenes. Subsequently, the details of Mallory photoreaction of the precursors to obtain the target compounds were described. The introduction of two imide groups into the picene backbone induced a noticeable change in its optical natures, *e.g.*, energy levels of molecular orbitals. It was indicated that wider bandgap and deeper LUMO energy level relative to the parent picene were induced by the imide substitution. The electronic spectra of **C<sub>n</sub>-PicDI**s in solution showed the same profiles irrespective of the alkyl chain lengths. In contrast, in thin films, the UV absorption and photoelectron yield spectroscopy (PYS) indicted that the LUMO energy level of **C<sub>n</sub>-PicDI**s gradually changed

depending on the alkyl chains indicating that the alkyl chains modified the intermolecular interactions between the **C<sub>n</sub>-PicDI** molecules in thin film. The FET properties of **C<sub>n</sub>-PicDI** thin-films with ZrO<sub>2</sub> gate dielectric were investigated. N-type properties were observed for the **C<sub>n</sub>-PicDI** thin-film FETs. The FET devices showed normally-off n-type operation, the averaged electron mobility was evaluated to be  $2(1) \times 10^{-4} \text{ cm}^2 \text{ V}^{-1} \text{ s}^{-1}$ ,  $1.0(6) \times 10^{-1} \text{ cm}^2 \text{ V}^{-1} \text{ s}^{-1}$  and  $1.4(3) \times 10^{-2} \text{ cm}^2 \text{ V}^{-1} \text{ s}^{-1}$  for **C<sub>4</sub>-PicDI**, **C<sub>8</sub>-PicDI** and **C<sub>12</sub>-PicDI**, respectively. The maximum electron mobility  $\mu$  as high as  $1.0 \times 10^{-1} \text{ cm}^2 \text{ V}^{-1} \text{ s}^{-1}$  was observed for **C<sub>8</sub>-PicDI**. The present results would contribute to the molecular design of new n-type organic semiconductors which are highly desired in the current organic electronics.



**In chapter 2**, a molecular design to control electronic features of the picene via substitution of the picene  $\pi$ -core with ester groups is presented. It is expected that ester functionalized picenes would display different electronic features than the parent  $\pi$ -core. The ester derivatives **7** and **10** were synthesized by using Mallory photocyclization as the key step. Potentials of the ester derivatives **7** as an active layer of FET devices were examined. From the results, unfortunately, it was observed that compound **7** did not serve as the active layer of the FET devices, under the current device fabrication and measurement conditions.





## **Chapter 1**

## 1.1 Background of Organic Field-Effect Transistors

Field effect transistor (FET) is a fundamental electronic device that switches and amplifies electrical signals.<sup>1-4</sup> Inorganic semiconductor have been intensively developed and widely applied in our daily life. However, fabrication of inorganic semiconductor devices requires their extremely high purity and very precisely controlled device fabrication process under highly demanding conditions. Organic field-effect transistors (OFETs) have been conceptualized and extensively developed over the past two decades since the report of polythiophene by Tsumura in 1986.<sup>5</sup>

While it is expected that a variety of organic devices will be commercialized in the near future, there is few indications that organic electronics will supersede inorganic electronics in many applications. Due to advantages over inorganic ones *e.g.*, lightweight, low-cost, flexibility and large-area, organic semiconductors will be promising materials for the next generation of electronic circuits, such as radio-frequency identification tags (RFIDs), organic light emitting diodes (OLEDs) and chemical/biological sensors.<sup>6-8</sup> Namely, organic electronics will be implemented where inorganic devices would be impractical, for example in a flexible electronic device.

### 1.1.1 Operation Theory of OFET

Organic semiconductors are classified as p-type and n-type based on the transport properties; the charge transporting carrier are holes for the former and electrons for the latter. In order to design novel organic semiconductors, one should get acquainted with principle of operation.

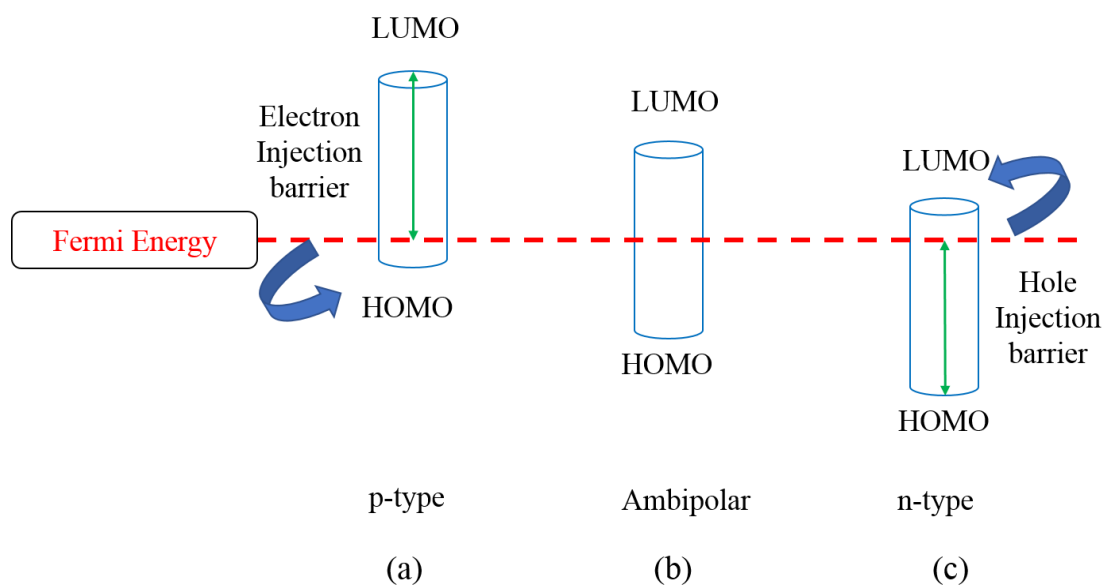


**Fig. 1-1.** A schematic image for concepts of OFET operation.

The schematic and working principle of OFETs are described in Fig. 1-1. OFETs operate as an electronic switch, in which the current flow between the source and drain electrodes is modulated by the gate voltage. Their performance critically depends on how efficiently the carriers can move in the conducting channel. When the highest occupied molecular orbital (HOMO) energy is situated closer to the Fermi energy ( $E_F$ ) of the electrode (Fig 1-1, (a)), hole injection is facilitated because of the small hole injection barrier ( $\phi_h$ ), that enables p-type behavior. For organic semiconductors (OSCs) with smaller band gaps, both hole and electron injection barriers are small or within the limits of operating voltage, resulting in the ambipolar behavior of such materials (Fig. 1-1, (b)). When the lowest unoccupied molecular orbital (LUMO) energy of OSCs is close to the  $E_F$  of the source electrode, injection of electrons into the LUMO of the semiconductor is facilitated because of the small electron injection barrier ( $\phi_e$ ) (Fig1-1, (c)), resulting in n-type operation. For p-type semiconductors, the work function of the metal must match the energy level of the HOMO of the OSCs. Likewise, for n-type OSCs, the work function of the electrode must match the LUMO energy level of the organic molecules.<sup>9</sup> Therefore, the frontier energy level of OSC molecules plays a critical role in determining semiconductor characteristics of a material.<sup>10</sup>

## 1.1.2 Molecular packing

In OSCs, charge carriers transport through the intermolecularly interacting  $\pi$  orbitals of the molecules. Therefore, the overlap degree between the adjacent molecular orbitals significantly determines the mobility of charges. Molecular packing with strong intermolecular overlapping is favorable for efficient charge carrier transport and, thus, resulting in the availability of high field-effect mobility. Fig. 1-2 depicts four common classifications of molecular packing in the solid state for typical  $\pi$ -conjugated aromatic OSCs. Among these, two-dimensional  $\pi$ - $\pi$  stacking is known to facilitate easier charge migration, resulting in good device performance.<sup>10</sup>

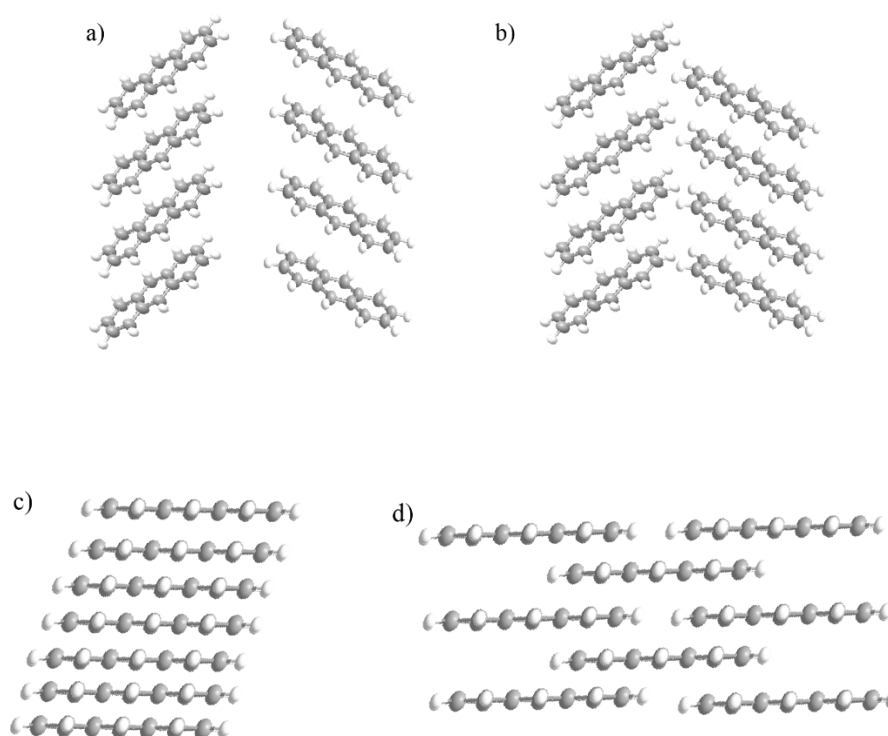


**Fig. 1-2.** Four types of molecular packing in the solid state for typical organic semiconductors. (a) Herringbone packing between adjacent molecules; (b) herringbone packing with  $\pi$ - $\pi$  overlap between adjacent molecules; (c) lamellar motif (1D stacking); (d) lamellar motif (2D stacking).

## 1.2 Typical Small Molecule Semiconductor

Conventionally, small molecule OSCs have been mainly constructed based on polycyclic aromatic hydrocarbons<sup>11</sup>. Small molecule semiconductors based on acene and phenacene (Fig. 1-3) have been widely investigated and well developed because they can be synthesized with high purity and easily form single crystals.<sup>12</sup>

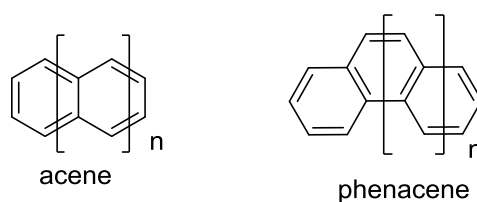


**Fig. 1-3.** General Structures of acene and phenacene.

### 1.2.1 Conventional p-type small molecular organic semiconductors

Acenes are polycyclic aromatic hydrocarbons with linearly fused benzenoid units. They have been of the subject of intense studies in OSCs because of the unique electronic properties derived from their  $\pi$ -bond topology. Acenes and their derivatives have been expected to be key candidates for organic semiconductors. For example, anthracene and tetracene were applied in active layer for single crystals FET devices displaying maximum mobility  $\mu$  values of  $0.02 \text{ cm}^2 \text{ V}^{-1} \text{ s}^{-1}$  and  $0.4 \text{ cm}^2 \text{ V}^{-1} \text{ s}^{-1}$ , respectively.<sup>13, 14</sup> Pentacene has been the benchmark compound of OSCs with high mobility. Numerous researches have focused on its applications in OFETs. A mobility as high as  $40 \text{ cm}^2 \text{ V}^{-1} \text{ s}^{-1}$  has been demonstrated in a single crystal pentacene based transistor with modified device structures.<sup>15,16</sup> Wherein, its efficient charge transport is mainly attributed to the extended  $\pi$ -system with strong intermolecular overlaps as well as the proper HOMO energy level for efficient hole injection and transport. A field-effect transistor fabricated by using a single crystal of non-substituted hexacene

displayed a hole mobility of  $4.28 \text{ cm}^2 \text{ V}^{-1} \text{ s}^{-1}$  with an on/off ratio of  $1 \times 10^5$  and a threshold voltage of 37 V.<sup>17</sup> The pure hexacene can be stored under ambient conditions in the dark.

There is critical drawback for acene molecules: the poor solubility in common organic solvents and instability of acenes with increased number of the fused benzene rings as well as that low environmental stability of acene molecules prevent their practical application. Therefore, it is significance to develop acene derivatives with improved solution-processability and stability under ambient conditions. One of the common approaches is to incorporate judicial substitutions at the edges or side positions of the acene molecules to extend the  $\pi$ -conjugated dimension to improve the planarity and to enhance the solubility. Several examples for making such oligoacenes are shown in Fig. 1-4, extending with two thienyl groups at the ends of anthracene, **DTAnt** exhibited mobility of  $0.06 \text{ cm}^2 \text{ V}^{-1} \text{ s}^{-1}$  being about 3-fold larger than anthracene.<sup>18</sup> With phenyl substituents on 9- and 10- positions of anthracene, compound **DPA** showed high electron mobility of  $13 \text{ cm}^2 \text{ V}^{-1} \text{ s}^{-1}$  and hole mobility of  $3.7 \text{ cm}^2 \text{ V}^{-1} \text{ s}^{-1}$ .<sup>19</sup> Furthermore, **rubrene** having four phenyl substituents on the side positions exhibited hole mobility as high as  $40 \text{ cm}^2 \text{ V}^{-1} \text{ s}^{-1}$  in a single-crystal based transistor.<sup>20</sup>

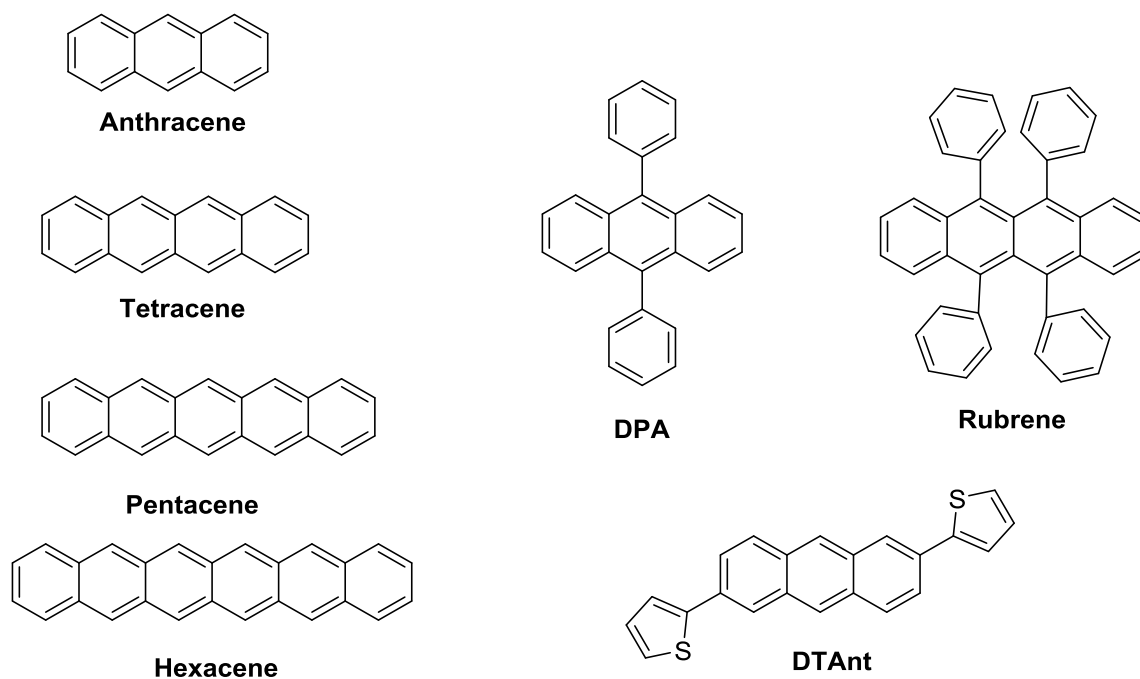


**Fig. 1-4.** Structures of acene and its derivatives.

Without doubt, acene chemistry has been one of the hottest topics in FET, however, the prominent issue is that the molecules are unstable with increasing benzene rings limiting the potential applications in OSCs.

A vast numerous of silylethynyl substituted acenes, such as **TIPS-Pn**<sup>21</sup> and **F<sub>8</sub>TIPS-Pn**<sup>22</sup> (see Fig. 1-5 for molecular structures) have been synthesized and introduced a new outlook in FET devices.

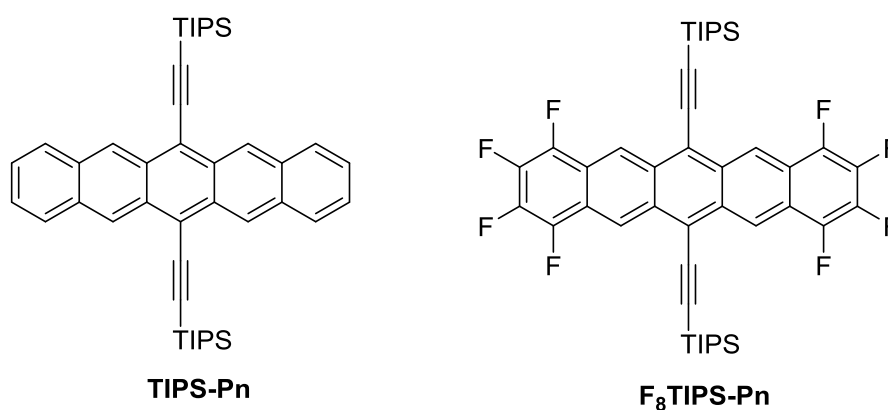


**Fig. 1-5.** Structures of **TIPS-Pn** and **F<sub>8</sub>TIPS-Pn**.

The TIPS functionality improved the solubility of the acene molecules considerably.

Additionally, TIPS groups arranged molecules in the solid state to permit controlling molecular packing, thus, the carrier mobility of **TIPS-Pn** reached to  $0.4 \text{ cm}^2 \text{ V}^{-1} \text{ s}^{-1}$  in thin-films. Halogenated TIPS incorporated acene, **F<sub>8</sub>TIPS-Pn**, displayed a stable and soluble properties. The charge-mobility for **F<sub>8</sub>TIPS-Pn**-based FET devices was shown to be  $0.045 \text{ cm}^2 \text{ V}^{-1} \text{ s}^{-1}$ .

Although new functionalization strategies are being developed to modulate electronic structures of longer acenes such as octacene and nonacene (see Fig. 1-6 for molecular structures), it is much more difficult in applying such molecules to FET devices because of their instability.<sup>23</sup> A more recent functionalization strategy involves the use of extensive substitution around the acene chromophores. In 2011, Anthony's group displayed a TIPS modified nonacene molecules **FTBN** (Fig. 1-6). This strategy provided a novel insight into producing stable larger acenes and their derivatives that enabled investigation of electronic features and detailed molecular structures.<sup>24</sup>

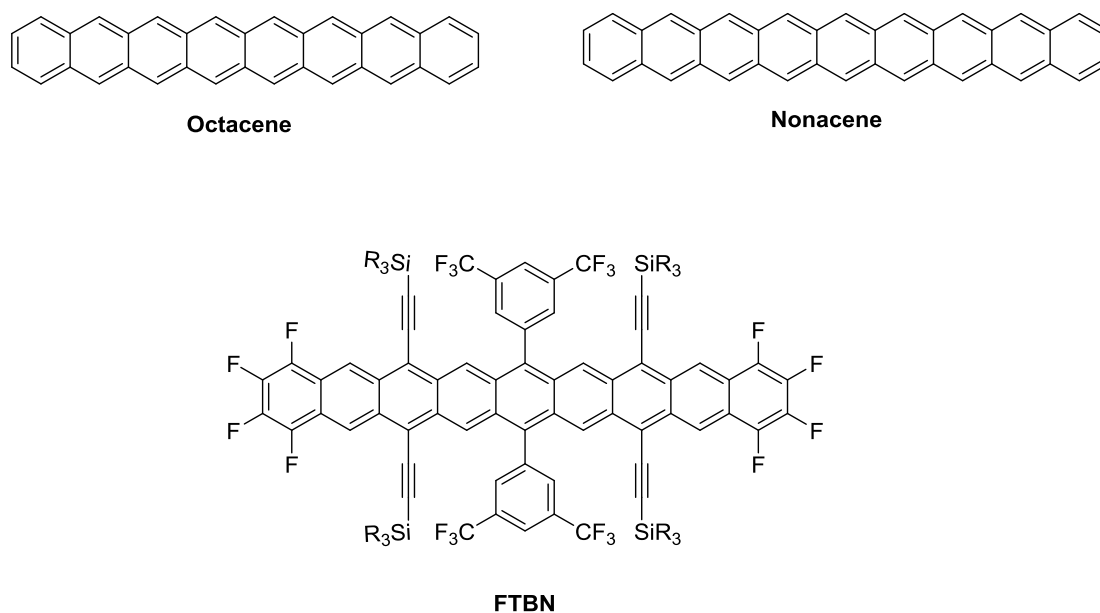


**Fig. 1-6.** Structures of larger acenes and a derivative.

Phenacene is isomeric form of acene that possesses zigzag fused benzene rings. Recently, [5]-[7]phenacene (see Fig. 1-7 for molecular structures) molecules have attracted significant attention for transistor applications because phenacene thin-film and single-crystal OFETs showed very high  $\mu$  values.<sup>25-28</sup> In particular, picene has



been extensively studied because it is easily synthesized and also even commercially available.

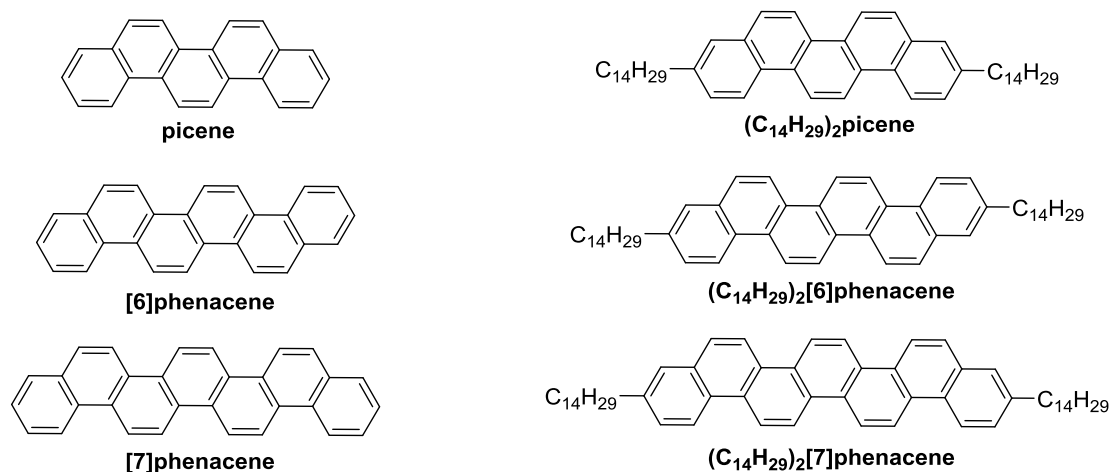


**Fig. 1-7.** Structures of phenacene and alkyl-substituted derivatives.

Picene is quite stable under air because of the unique electronic structures of phenacenes leading to the lower HOMO energy level. Therefore, picene is expected to be a new material in a viewpoint of device application. High performance p-type FET devices with  $\mu$  values larger than  $1 \text{ cm}^2 \text{ V}^{-1} \text{ s}^{-1}$  have been realized with picene thin films, and the FET properties are clearly improved under oxygen containing atmosphere.<sup>29</sup> Thus, the picene-based FET serves as an oxygen sensing device.<sup>25</sup> After this, [6] and [7]phenacenes, which have six and seven benzene rings, respectively, have been investigated as OFET materials and showed clear p-channel FET characteristics with  $\mu$  values being as high as 3.7 and  $0.8 \text{ cm}^2 \text{ V}^{-1} \text{ s}^{-1}$  respectively.<sup>27, 28</sup> Long alkyl chains have generally been utilized to improve the solubility of polycyclic aromatic hydrocarbons in organic solvents and to control molecular stacking between the aromatic cores.<sup>30</sup> This strategy has been successfully applied to phenacene to improve OFET performance. Tetradecyl chains were introduced into picene, [6]phenacene<sup>31</sup> and [7]phenacene<sup>32</sup> along the long-axis direction of the molecules (see Fig. 1-7 for the molecular structures) and the molecules have been applied to active layer of FET devices. The  $\mu$  values of thin film FETs are significantly increased for the alkyl-substituted picene and [7]phenacene. Especially, the highest  $\mu$  value of

(C<sub>14</sub>H<sub>29</sub>)<sub>2</sub>-picene reached to 21 cm<sup>2</sup> V<sup>-1</sup> s<sup>-1</sup> which was much higher than that for the parent picene molecule without alkyl chains.<sup>33</sup>

Compared to aromatic hydrocarbons, oligothienoacenes exhibited weak C-H $\cdots$  $\pi$  interactions, rather than  $\pi$ - $\pi$  stacking due to polarizability of the sulfur atoms in the molecules. Pentathienoacene (**PTA**)<sup>34</sup> and hexathienoacene (**HTA**, see Fig. 1-8 for molecular structures)<sup>35</sup> have been reported to show charge mobility of up to 0.045 cm<sup>2</sup> V<sup>-1</sup> s<sup>-1</sup> and 0.006 cm<sup>2</sup> V<sup>-1</sup> s<sup>-1</sup>, respectively. These results demonstrated that further extension of the conjugation of thiophene rings was not effective to improve the OFET performance.



**Fig. 1-8.** Structures of **PTA** and **HTA**.

Other fused thiophene-containing heteroaromatic ring systems have been designed and prepared, such as anthraceno[2,3-*b*]thiophene<sup>36,37</sup> tetraceno[2,3-*b*]thiophene (**TCT**),<sup>37</sup> pentaceno[2,3-*b*]thiophene (**PCT**)<sup>38</sup> and anthradithiophene (**ADT**)<sup>39</sup> (see Fig. 1-9 for molecular structures). The oligothienoacenes possess one or two terminal benzene rings fused with thiophene one. These conjugated molecules showed better stability and provide charge mobilities of 0.15 cm<sup>2</sup> V<sup>-1</sup> s<sup>-1</sup> for **ACT**, 0.47 cm<sup>2</sup> V<sup>-1</sup> s<sup>-1</sup> for **TCT**, 0.57 cm<sup>2</sup> V<sup>-1</sup> s<sup>-1</sup> for **PCT**. In contrast, the charge mobility of **ADT** was found to be 0.09 cm<sup>2</sup> V<sup>-1</sup> s<sup>-1</sup> due to the two isomers existing in the compound.

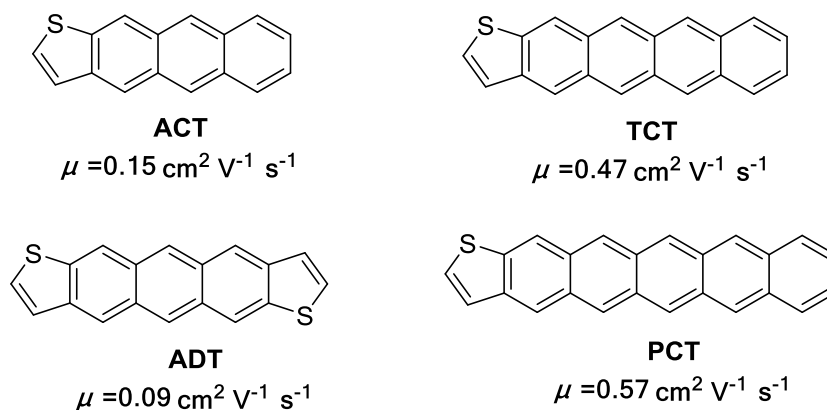


**Fig. 1-9.** Structures of heteroacene derivatives.

It appears that the heteroatom replacement is promising to produce efficient OSCs, thus, heteroatoms, such as sulfur, nitrogen, and selenium have been conventionally introduced into aromatic  $\pi$  systems. Some examples of such molecules are displayed in Fig. 1-10. The charge mobility of quaterthiophene<sup>40</sup> was  $0.0025 \text{ cm}^2 \text{ V}^{-1} \text{ s}^{-1}$  and that of quatersephenophene<sup>41</sup> was  $0.0036 \text{ cm}^2 \text{ V}^{-1} \text{ s}^{-1}$ , the effect of selenium was, thus, quite marginal. However, the replacement of the sulfur with nitrogen atoms had an appreciable effect on the OFET performance for a five-ring heteroaromatic system. In the case of **DBTDT**<sup>42</sup> and *anti*-**DBTP**<sup>43</sup> (see Fig. 1-10 for molecular structures), charge mobility was increased from  $0.012 \text{ cm}^2 \text{ V}^{-1} \text{ s}^{-1}$  to  $0.6 \text{ cm}^2 \text{ V}^{-1} \text{ s}^{-1}$  when the nitrogen atom was replaced by sulfur one. This phenomenon was commonly observed when some of the  $\text{sp}^2$  carbons of a semiconductor molecules are replaced by the heteroatoms, thus, the charge mobility of constituents is increased.<sup>44, 45</sup>

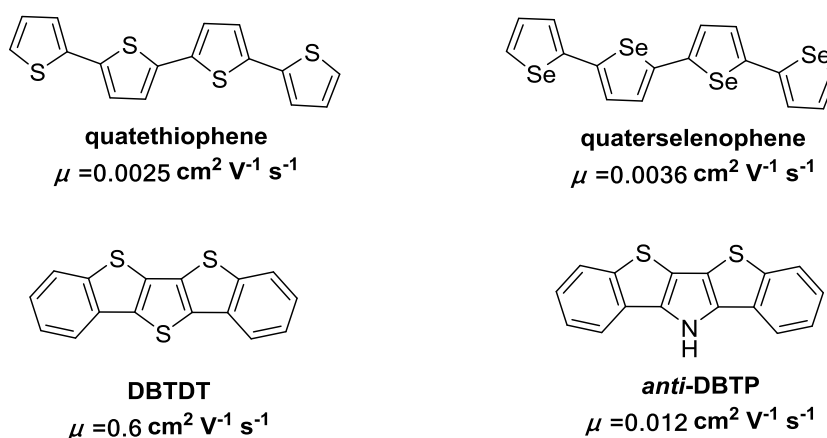


**Fig. 1-10.** Representative structures of heteroatom incorporatory fused aromatics.

The present [1]benzothieno[3,2-b][1]benzothiophene (**BTBT**)-based materials can be charged as one of the ideal classes of p-type OSCs. Long alkyl-chain substituted derivatives, such as, **C<sub>n</sub>-BTBT**<sup>46</sup> and **C<sub>10</sub>-DNBDT-NW**<sup>47</sup> (see Fig. 1-11 for molecular structures) showed excellent electron mobility of 1 cm<sup>2</sup> V<sup>-1</sup> s<sup>-1</sup> and 16 cm<sup>2</sup> V<sup>-1</sup> s<sup>-1</sup>, respectively.

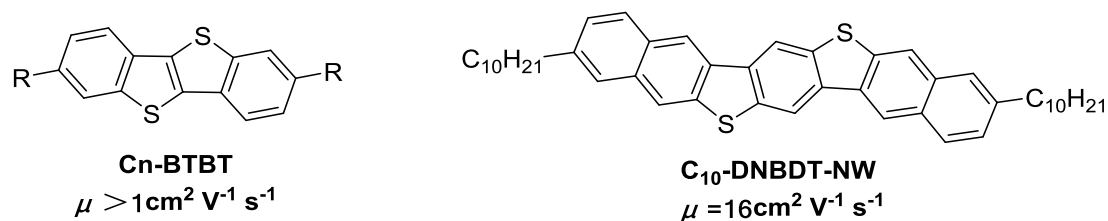


**Fig. 1-11.** Structures of **C<sub>n</sub>-BTBT** and **C<sub>10</sub>-DNBDT-NW**.

The sulfur atoms significantly contributed to provide the appropriate HOMO energy level and to arrange the intermolecular HOMO overlap suitable for the carrier transport.

## 1.2.2 Conventional n-type small molecular organic semiconductors

Organic semiconductor molecules applicable to FETs have drawn intensive attention because of their intriguing advantages and promising potentials. Most effort has been devoted to the p-type organic semiconductors.<sup>48-50</sup> The delay in developing n-type OSCs could be primarily attributed to (1) the instability of the organic radical anions in the presence of oxygen, water, and various electron traps on the interfaces around a directing channel and (2) the large injection barrier of electron between the work function of metals and the LUMO energy levels of the semiconductors.<sup>51</sup>

An ideal n-type organic semiconductor should be solution processable, stable under air. Also, it is desired for practical n-type OSCs to provide low electron injection barriers and high charge carrier mobilities. Many experimental and theoretical

investigations have shown that solubility, electronic absorption, and emission behavior can be efficiently tuned by functionalization with hydrophobic, hydrophilic, electron-donating or electron-withdrawing groups. Especially, functionalizing the structures with electron-withdrawing groups, such as halogen atoms, cyano, carbonyl, and imide groups, will reduce the electron density on the aromatic backbone, thus, considered to be useful to obtain n-type OSCs.

Introduction of highly electronegative fluorine atoms is one of common methods to lower the LUMO energy level. Perfluorotetracene and perfluoropentacene (see Fig. 1-12 for molecular structures) showed n-type FET behavior with an electron mobility of  $2.4 \times 10^{-4} \text{ cm}^2 \text{ V}^{-1} \text{ s}^{-1}$  and  $0.22 \text{ cm}^2 \text{ V}^{-1} \text{ s}^{-1}$  respectively.<sup>52, 53</sup>

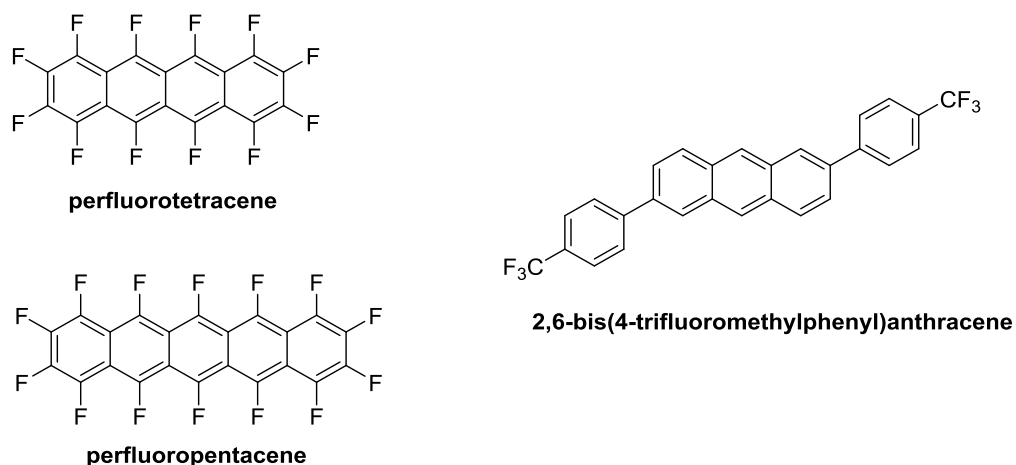


**Fig. 1-12.** Structures of fluorinated acene derivatives.

Another affordable strategy is to introduce electron-withdrawing trifluoromethyl groups into aromatic rings, *e.g.*, 2,6-bis(4-trifluoromethyl-phenyl)anthracene, a simple derivative of anthracene incorporating two 4-trifluoromethylphenyl groups on the molecular edges has been reported.<sup>54</sup>

Cyano functionality is also adopted as an electron withdrawing group for n-type OSCs. Tetracyanoquinodimethane (TCNQ) showed electron mobility as high as  $1.6 \text{ cm}^2 \text{ V}^{-1} \text{ s}^{-1}$  in the single crystalline form (see Fig. 1-13 for molecular structures).<sup>55</sup> TCP was first prepared by Glocklhofer through a one-pot synthesis method.<sup>56</sup> As

expected, **TCP** exhibited n-type semiconducting behavior, with electron mobility of *ca.*  $2.2 \times 10^{-4} \text{ cm}^2 \text{ V}^{-1} \text{ s}^{-1}$ , indicating that the introduction of cyano group into the *peri* position of acene is an effective method to transfer p-type OSCs into n-type ones.

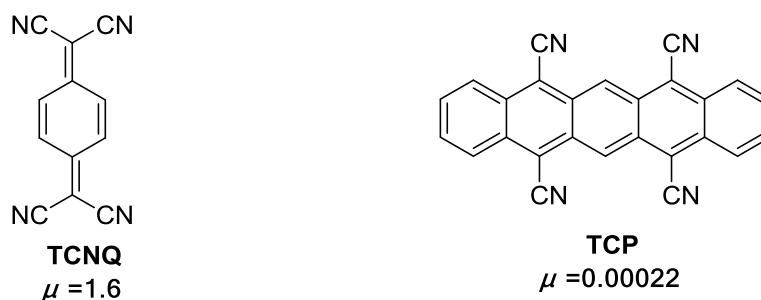


**Fig. 1-13.** Structures of **TCNQ** and **TCP**.

Acenequinones are known to be very stable and adopt favorable  $\pi$  stacking with low distortion. Replacing the carbon atoms in acenequinones with nitrogen ones lowered the LUMO energy level of pentacenequinone (see Fig. 1-14 for molecular structures) to yield n-type OSCs with a field effect mobility up to  $0.12 \text{ cm}^2 \text{ V}^{-1} \text{ s}^{-1}$ .<sup>9,57</sup> In 2011, Tao's group reported an air stable n-type semiconductor, tetrachlorodiazapentacene, which had a LUMO energy level of  $-3.79 \text{ eV}$  and effective  $\pi$ - $\pi$  stacks in the solid state.<sup>58</sup> Highly flexible needle-shaped crystal of tetrachlorodiazapentacene was applied to an n-type FET to exhibit high electron mobility up to  $3.39 \text{ cm}^2 \text{ V}^{-1} \text{ s}^{-1}$ .

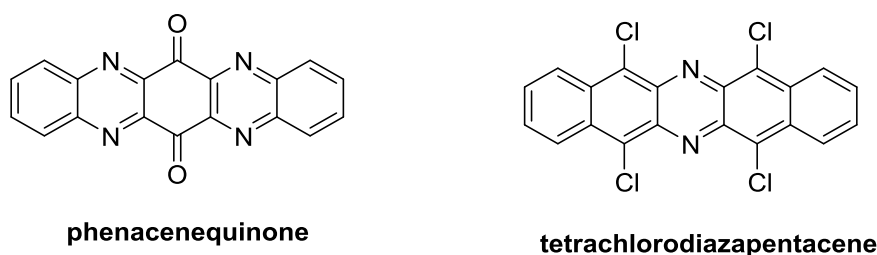


**Fig. 1-14.** Structures of heteropentacene derivatives.

Imide is also established as a highly electron withdrawing functionality. The functionality is very versatile and allows modification of the physical properties of polycyclic aromatic molecules by charging an appropriate functionality at the imide

nitrogen atom without changing structures of the aromatic core.<sup>10, 59</sup> Diimidization of aromatic systems will lower the LUMO energy level and significantly enhance electron affinity. Thus, introduction of imide groups into aromatic core is useful for developing n-type OSCs materials.

Pyromelliticdiimides (**PMDI**, see Fig.1-15 for molecular structure) which has the smallest aromatic core,<sup>60</sup> has shown a high field-effect electron mobility of  $0.079 \text{ cm}^2 \text{ V}^{-1} \text{ s}^{-1}$ . Wang reported that **AnDI**-based devices exhibit good electron mobility up to  $0.02 \text{ cm}^2 \text{ V}^{-1} \text{ s}^{-1}$ , and high on/off ratio  $> 10^7$  under ambient conditions as a consequence of balanced electron affinity.<sup>61</sup>

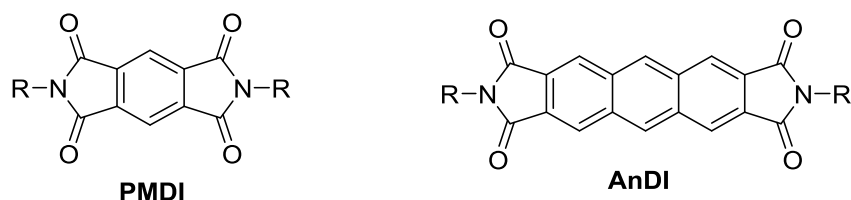


**Fig. 1-15.** Structures of **PMDI** and **AnDI**.

Naphthalenediimides (**NDIs**) and perylenediimides (**PDI**s) (see Fig. 1-16 for molecular structures) are two promising candidates for n-type OFET materials. Large electron affinities of the imide functionality facilitate electron accumulation. Additionally, it is easy to introduce various substituents on the imide nitrogen atoms for tuning the molecular self-assembly abilities, charge transport properties as well as air stability.<sup>42, 62, 63</sup>

Furthermore, a series of organic molecules derived from electron deficient aromatic cores are investigated for organic transistors. For example, **NDI-8CN<sub>2</sub>** (see Fig. 1-16 for molecular structures) has considerably low LUMO energy level of  $-4.5 \text{ eV}$ , hence, they are stable under ambient device operating conditions. Top contact devices of **NDI-8CN<sub>2</sub>** fabricated by a vacuum-deposition technique displayed an averaged mobility of  $0.15 \text{ cm}^2 \text{ V}^{-1} \text{ s}^{-1}$  in vacuum and  $0.11 \text{ cm}^2 \text{ V}^{-1} \text{ s}^{-1}$  under air.<sup>64</sup>

More recently, nitrogen-containing PDI analogue, **BQQDI**, based on unique

molecular design strategies was described.<sup>65</sup> Nitrogen atom was introduced into the perylene system at the optimum positions to achieve stability with high electron mobility.

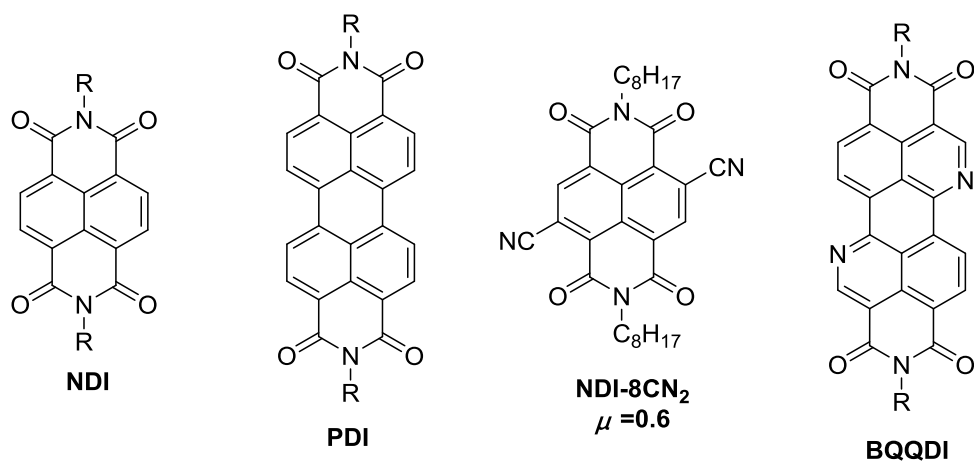


**Fig. 1-16.** Chemical structures of **NDI**, **PDI** and **NDI-8CN<sub>2</sub>**.

This thesis focuses on furthering the study of structure-charge transport properties of  $\pi$ -conjugated phenacene derivatives through introducing the electron-withdrawing groups. To understand the factors affecting the charge-carrier mobility of molecules, picene derivatives incorporating imide and ester moieties along the long axis direction of the picene core were conveniently synthesized by using Mallory photocyclization as the key step for constructing the picene skeleton. The details of the synthesis and characterization of novel picene derivatives-based semiconductors are described in the thesis.



### 1.3 References

1. J. Mei, Y. Diao, A. L. Appleton, L. Fang and Z. Bao, *J. Am. Chem. Soc.*, 2013, **135**, 6724-6746.
2. Y. Sun, Y. Liu and D. Zhu, *J. Mater. Chem.*, 2005, **15**, 53.
3. T. Okamoto, C. P. Yu, C. Mitsui, M. Yamagishi, H. Ishii and J. Takeya, *J. Am. Chem. Soc.*, 2020, **142**, 9083-9096.
4. T. W. Kelley, P. F. Baude, C. Gerlach, D. E. Ender, D. Muyres, M. A. Haase, D. E. Vogel and S. D. Theiss, *Chem. Mater.*, 2004, **16**, 4413-4422.
5. A. Tsumura, H. Koezuka and T. Ando, *Appl. Phys. Lett.*, 1986, **49**, 1210-1212.
6. K. Zhou, H. Dong, H. L. Zhang and W. Hu, *Phys. Chem. Chem. Phys.*, 2014, **16**, 22448-22457.
7. K. J. Baeg, M. Caironi and Y. Y. Noh, *Adv. Mater.*, 2013, **25**, 4210-4244.
8. K. Myny, S. Steudel, S. Smout, P. Vicca, F. Furthner, B. van der Putten, A. K. Tripathi, G. H. Gelinck, J. Genoe and W. Dehaene, *Org. Electron.*, 2010, **11**, 1176-1179.
9. J. E. Anthony, *Chem. Rev.*, 2006, **106**, 5028-5048.
10. A. Naibi Lakshminarayana, A. Ong and C. Chi, *J. Mater. Chem. C*, 2018, **6**, 3551-3563.
11. J. M. Farrell, C. Mutzel, D. Bialas, M. Rudolf, K. Menekse, A. M. Krause, M. Stolte and F. Wurthner, *J. Am. Chem. Soc.*, 2019, **141**, 9096-9104.
12. J. E. Anthony, *Angew. Chem. Int. Edit.*, 2008, **47**, 452-483.
13. A. N. Aleshin, J. Y. Lee, S. W. Chu, J. S. Kim and Y. W. Park, *Appl. Phys. Lett.*, 2004, **84**, 5383-5385.
14. R. W. I. de Boer, T. M. Klapwijk and A. F. Morpurgo, *App. Phys. Lett.*, 2003, **83**, 4345-4347.
15. O. D. Jurchescu, M. Popinciuc, B. J. van Wees and T. T. M. Palstra, *Adv. Mater.*, 2007, **19**, 688-692.
16. H. Klauk, U. Zschieschang, R. T. Weitz, H. Meng, F. Sun, G. Nunes, D. E.

- Keys, C. R. Fincher and Z. Xiang, *Adv. Mater.*, 2007, **19**, 3882-3887.
17. M. Watanabe, Y. J. Chang, S. W. Liu, T. H. Chao, K. Goto, M. M. Islam, C. H. Yuan, Y. T. Tao, T. Shinmyozu and T. J. Chow, *Nat. Chem.*, 2012, **4**, 574-578.
  18. H. Meng, F. Sun, M. B. Goldfinger, G. D. Jaycox, Z. Li, W. J. Marshall and G. S. Blackman, *J. Am. Chem. Soc.*, 2005, **127**, 2406-2407.
  19. A. K. Tripathi, M. Heinrich, T. Siegrist and J. Pflaum, *Adv. Mater.*, 2007, **19**, 2097-2101.
  20. T. Hasegawa and J. Takeya, *Sci. Technol. Adv. Mater.*, 2009, **10**, 024314.
  21. J. E. Anthony, D. Vogel, S. Schnobrich, R. Clough, J. Novack and D. Redinger, *Mater. Matt.*, 2009, **4**.
  22. C. R. Swartz, S. R. Parkin, J. E. Bullock, J. E. Anthony, A. C. Mayer and G. G. Malliaras, *Org. Lett.*, 2005, **7**, 3163-3166.
  23. C. Tonshoff and H. F. Bettinger, *Angew. Chem. Int. Edit.*, 2010, **49**, 4125-4128.
  24. B. Purushothaman, M. Bruzek, S. R. Parkin, A. F. Miller and J. E. Anthony, *Angew. Chem. Int. Edit.*, 2011, **50**, 7013-7017.
  25. H. Okamoto, N. Kawasaki, Y. Kaji, Y. Kubozono, A. Fujiwara and M. Yamaji, *J. Am. Chem. Soc.*, 2008, **130**, 10470-10471.
  26. N. Kawasaki, Y. Kubozono, H. Okamoto, A. Fujiwara and M. Yamaji, *Appl. Phy. Lett.*, 2009, **94**, 043310.
  27. N. Komura, H. Goto, X. He, H. Mitamura, R. Eguchi, Y. Kaji, H. Okamoto, Y. Sugawara, S. Gohda, K. Sato and Y. Kubozono, *Appl. Phy. Lett.*, 2012, **101**, 083301.
  28. Y. Sugawara, Y. Kaji, K. Ogawa, R. Eguchi, S. Oikawa, H. Gohda, A. Fujiwara and Y. Kubozono, *Appl. Phy. Lett.*, 2011, **98**, 013303.
  29. X. Lee, Y. Sugawara, A. Ito, S. Oikawa, N. Kawasaki, Y. Kaji, R. Mitsuhashi, H. Okamoto, A. Fujiwara, K. Omote, T. Kambe, N. Ikeda and Y. Kubozono, *Org. Electron.*, 2010, **11**, 1394-1398.
  30. X.-C. Chen, S. Nishinaga, Y. Okuda, J.-J. Zhao, J. Xu, H. Mori and Y. Nishihara, *Org. Chem. Front.*, 2015, **2**, 536-541.

31. M. Murai, H. Maekawa, S. Hamao, Y. Kubozono, D. Roy and K. Takai, *Org. Lett.*, 2015, **17**, 708-711.
32. H. Okamoto, S. Hamao, K. Kozasa, Y. Wang, Y. Kubozono, Y.-H. Pan, Y.-H. Yen, G. Hoffmann, F. Tani and K. Goto, *J. Mater. Chem. C*, 2020, **8**, 7422-7435.
33. H. Okamoto, S. Hamao, H. Goto, Y. Sakai, M. Izumi, S. Gohda, Y. Kubozono and R. Eguchi, *Sci. Rep.*, 2014, **4**, 5048.
34. K. Xiao, Y. Liu, T. Qi, W. Zhang, F. Wang, J. Gao, W. Qiu, Y. Ma, G. Cui and S. Chen, *J. Am. Chem. Soc.*, 2005, **127**, 13281-13286.
35. Y. Liu, X. Sun, C. A. Di, Y. Liu, C. Du, K. Lu, S. Ye and G. Yu, *Chem. Asian J.*, 2010, **5**, 1550-1554.
36. E. Guallar, F. J. Jimenez, P. van 't Veer, P. Bode, R. A. Riemersma, J. Gomez-Aracena, J. D. Kark, L. Arab, F. J. Kok, J. M. Martin-Moreno, E. U.-H. Metals and G. Myocardial Infraction Study, *Am. J. Epidemiol*, 2005, **162**, 157-164.
37. M. L. Tang, T. Okamoto and Z. Bao, *J. Am. Chem. Soc.*, 2006, **128**, 16002-16003.
38. M. L. Tang, S. C. Mannsfeld, Y.-S. Sun, H. A. Becerril and Z. Bao, *J. Am. Chem. Soc.*, 2009, **131**, 882-883.
39. J. G. Laquindanum, H. E. Katz and A. J. Lovinger, *J. Am. Chem. Soc.*, 1998, **120**, 664-672.
40. F. Garnier, R. Hajlaoui, A. El Kassmi, G. Horowitz, L. Laigre, W. Porzio, M. Armanini and F. Provasoli, *Chem. mater.*, 1998, **10**, 3334-3339.
41. Y. Kunugi, K. Takimiya, K. Yamane, K. Yamashita, Y. Aso and T. Otsubo, *Chem. Mater.*, 2003, **15**, 6-7.
42. J. H. Gao, R. J. Li, L. Q. Li, Q. Meng, H. Jiang, H. X. Li and W. P. Hu, *Adv. Mater.*, 2007, **19**, 3008-3011.
43. T. Qi, Y. Guo, Y. Liu, H. Xi, H. Zhang, X. Gao, Y. Liu, K. Lu, C. Du, G. Yu and D. Zhu, *Chem. Commun.*, 2008, 6227-6229.
44. Y. Inoue, M. Kitano, K. Nakajima and M. Hara, *Chem. Lett.*, 2011, **40**,

- 410-411.
45. N. P. D. Ngidi, M. A. Ollengo and V. O. Nyamori, *Int. J. Energy Res.*, 2019, **43**, 1702-1734.
  46. H. Ebata, T. Izawa, E. Miyazaki, K. Takimiya, M. Ikeda, H. Kuwabara and T. Yui, *J. Am. Chem. Soc.*, 2007, **129**, 15732-15733.
  47. C. Mitsui, T. Okamoto, M. Yamagishi, J. Tsurumi, K. Yoshimoto, K. Nakahara, J. Soeda, Y. Hirose, H. Sato, A. Yamano, T. Uemura and J. Takeya, *Adv. Mater.*, 2014, **26**, 4546-4551.
  48. T. W. Lee, D. H. Lee, J. Shin, M. J. Cho and D. H. Choi, *Poly. Chem.*, 2015, **6**, 1777-1785.
  49. G. Kim, S. J. Kang, G. K. Dutta, Y. K. Han, T. J. Shin, Y. Y. Noh and C. Yang, *J. Am. Chem. Soc.*, 2014, **136**, 9477-9483.
  50. C. Luo, A. K. Kyaw, L. A. Perez, S. Patel, M. Wang, B. Grimm, G. C. Bazan, E. J. Kramer and A. J. Heeger, *Nano. Lett.*, 2014, **14**, 2764-2771.
  51. Q. Meng and W. Hu, *Phys. Chem. Chem. Phys.*, 2012, **14**, 14152-14164.
  52. Y. Inoue, Y. Sakamoto, T. Suzuki, M. Kobayashi, Y. Gao and S. Tokito, *J. Appl. Phys.*, 2005, **44**, 3663.
  53. Y. Sakamoto, T. Suzuki, M. Kobayashi, Y. Gao, Y. Inoue and S. Tokito, *Mole. Cryst. Liq. Cryst.*, 2006, **444**, 225-232.
  54. S. Ando, J.-i. Nishida, E. Fujiwara, H. Tada, Y. Inoue, S. Tokito and Y. Yamashita, *Chem. Mater.*, 2005, **17**, 1261-1264.
  55. E. Menard, V. Podzorov, S. H. Hur, A. Gaur, M. E. Gershenson and J. A. Rogers, *Adv. Mater.*, 2004, **16**, 2097-2101.
  56. F. Glocklhofer, A. Petritz, E. Karner, M. J. Bojdys, B. Stadlober, J. Frohlich and M. M. Unterlass, *J. Mater. Chem. C*, 2017, **5**, 2603-2610.
  57. Z. Liang, Q. Tang, J. Liu, J. Li, F. Yan and Q. Miao, *Chem. Mater.*, 2010, **22**, 6438-6443.
  58. M. M. Islam, S. Pola and Y. T. Tao, *Chem. Commun.*, 2011, **47**, 6356-6358.
  59. C. Li, Z. Lin, Y. Li and Z. Wang, *Chem. Rec.*, 2016, **16**, 873-885.
  60. Q. Zheng, J. Huang, A. Sarjeant and H. E. Katz, *J. Am. Chem. Soc.*, 2008, **130**,

14410-14411.

61. Z. Wang, C. Kim, A. Facchetti and T. J. Marks, *J. Am. Chem. Soc.*, 2007, **129**, 13362-13363.
62. P. R. L. Malenfant, C. D. Dimitrakopoulos, J. D. Gelorme, L. L. Kosbar, T. O. Graham, A. Curioni and W. Andreoni, *Appl. Phys. Lett.*, 2002, **80**, 2517-2519.
63. H. Chen, M. Ling, X. Mo, M. Shi, M. Wang and Z. Bao, *Chem. Mater.*, 2007, **19**, 816-824.
64. B. A. Jones, A. Facchetti, T. J. Marks and M. R. Wasielewski, *Chem. Mater.*, 2007, **19**, 2703-2705.
65. T. Okamoto, S. Kumagai, E. Fukuzaki, H. Ishii, G. Watanabe, N. Niitsu, T. Annaka, M. Yamagishi, Y. Tani and H. Sugiura, *Sci. Adv.*, 2020, **6**, 632.



## **Chapter 2**

## 2.1 Introduction

A part of the results described in this chapter have been published.<sup>1</sup>

N-type organic semiconductors have attracted much attention in recent years owing to their important roles in organic electronics.<sup>2-5</sup> Potential applications of n-type organic semiconductors are electronic paper,<sup>6</sup> active-matrix emissive displays,<sup>7</sup> radio-frequency identity (RFID) tags.<sup>8</sup> Due to  $\pi$ - $\pi$  stacking leads to molecular orbital overlap and  $\pi$ -electron delocalization in solid states, electron deficient aromatic diimides have been considered as a standard for intrinsic transport studies in organic electronics.<sup>9, 10</sup>

[n]Phenacenes (see Fig. 2-1 for molecular structure), where n is the number of fused benzene rings are armchair-structured isomer of acene typified by pentacene, they have attracted much attention due to their superior p-type FET characteristics.<sup>11</sup> This is because that picene showed not only a good mobility Ca.  $1.1 \text{ cm}^2 \text{ V}^{-1} \text{ s}^{-1}$  with a current on/off ratio of  $10^5$  under ambient atmosphere but also a higher stability than pentacene.<sup>12</sup>

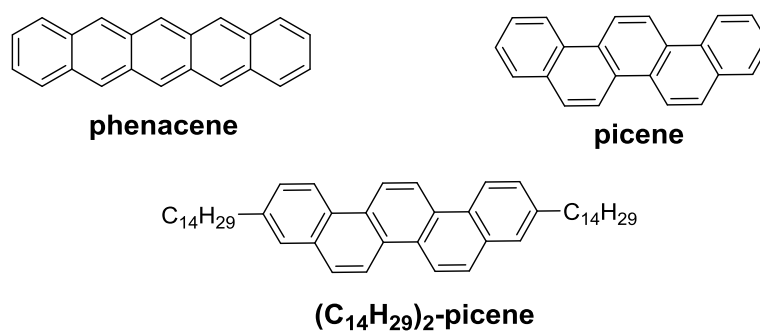


**Fig. 2-1.** Structure of phenacene, picene and (C<sub>14</sub>H<sub>29</sub>)<sub>2</sub>-picene.

Generally, the solubilities of unsubstituted [n]phenacenes decrease greatly with increasing n in the common organic solvents due to its light crystallinity. Therefore, solubility problem should be solved by incorporating suitable substituents into the phenacene cores. With the aim of gaining insight into the structure-property



relationships of high performance phenacene semiconductors materials and synthesizing a picene derivatives, which has better solubility, chemically modified synthesis and FET properties were investigated. It has been reported that thin-film OFETs based on a 3,10-dialkylpicene ((C<sub>14</sub>H<sub>29</sub>)<sub>2</sub>-picene, see Fig. 2-1 for molecular structure) showed field-effect mobilities ( $\mu$ ) as high as 20.9 cm<sup>2</sup> V<sup>-1</sup> s<sup>-1</sup>.<sup>13</sup>

Recently, impressive research progress is bearing made with polycyclic aromatic compound by modification with electron-accepting functional groups to construct high-performance n-type organic semiconductors.<sup>14,15</sup> Apparently, n-type semiconductors based on polycyclic aromatic systems require electron-deficient nature, thus, a lowering LUMO energy level.<sup>16, 17</sup> Such electronic properties are installed with multiple electron-withdrawing groups on the aromatic systems.

Large phenacenes, having imide moieties in the branching directions along the long molecular axis and the related polycyclic aromatic diimides were previously synthesized.<sup>18, 19</sup>

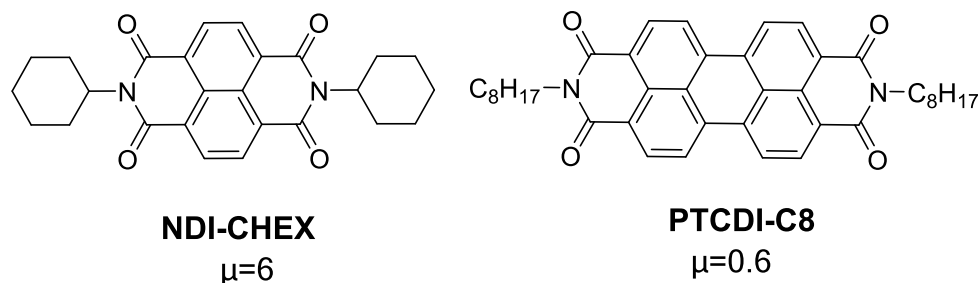


**Fig. 2-2.** Structure of **NDI-CHEX** and **PTCDI-C8**.

Amongst various molecules, naphthalene diimides<sup>20</sup> and perylene diimides (**PDI**)<sup>21</sup> are promising building blocks which have been widely employed to construct n-type semiconductors with high performance and good air stability. Adiga and co-authors have reported the fabrication of n-type OTFTs comprising cyclohexyl-functionalized diimides **NDI-CHEX** (see Fig. 2-2 for molecular structure). The highest mobility of **NDI-CHEX** under air was 6 cm<sup>2</sup> V<sup>-1</sup> s<sup>-1</sup>.<sup>22</sup> As in the case of the **NDI-CHEX** based OFETs, the devices comprising **PTCDI-C8** (see Fig. 2-2 for molecular structure) rapidly cease to operate in air. **PTCDI-C8** thin film have been implemented into

organic thin-film field-effect transistors and showed mobilities up to  $0.6 \text{ cm}^2 \text{ V}^{-1} \text{ s}^{-1}$  and current on/off ratios  $> 10^5$ .<sup>23</sup>

Wang *et al.* reported that the diimide derivatives of dibenzo[*a,h*]anthracene and phenanthro[1,2-*b*]chrysene (see Fig. 2-3 for molecular structures) served as active layers of n-channel FET devices displaying electron mobility up to  $0.054 \text{ cm}^2 \text{ V}^{-1} \text{ s}^{-1}$ .<sup>24</sup> The intramolecular cyclization was endeavored under photoirradiation conditions. The diolefinic substrates were irradiated with high-pressure mercury lamp in a mixed solvent of acetone and propylene oxide in the presence of iodine. However, few literatures on n-type FET application of phenacene diimides have been so far available.

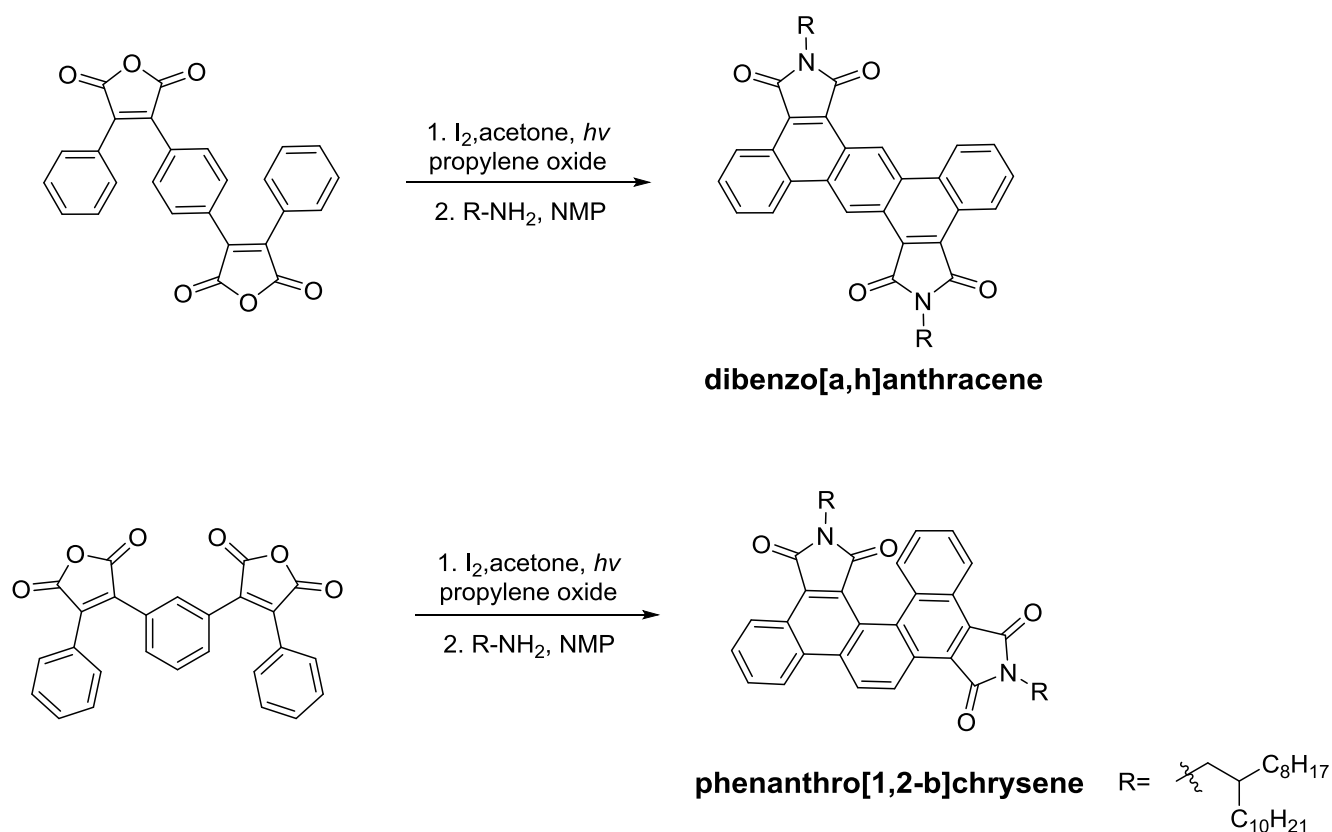


**Fig. 2-3.** Structure of diimide-containing phenacene derivatives.

More recently, Durola's group inspired by Mallory's approach, they reported the syntheses of tetracarboxy-substituted [14]phenacene by double photocyclization of

flexible precursors obtained by double Perkin condensation of building blocks.<sup>25</sup> Furthermore, a [20]phenacene dodeca-ester has been synthesized which is the longest phenacene so far reported as shown in Fig. 2-4.<sup>19</sup> The absorption spectra of [14]phenacene tetra-ester and [20]phenacene dodeca-ester are similar, while red-shifts increase with increasing the number of benzene rings.

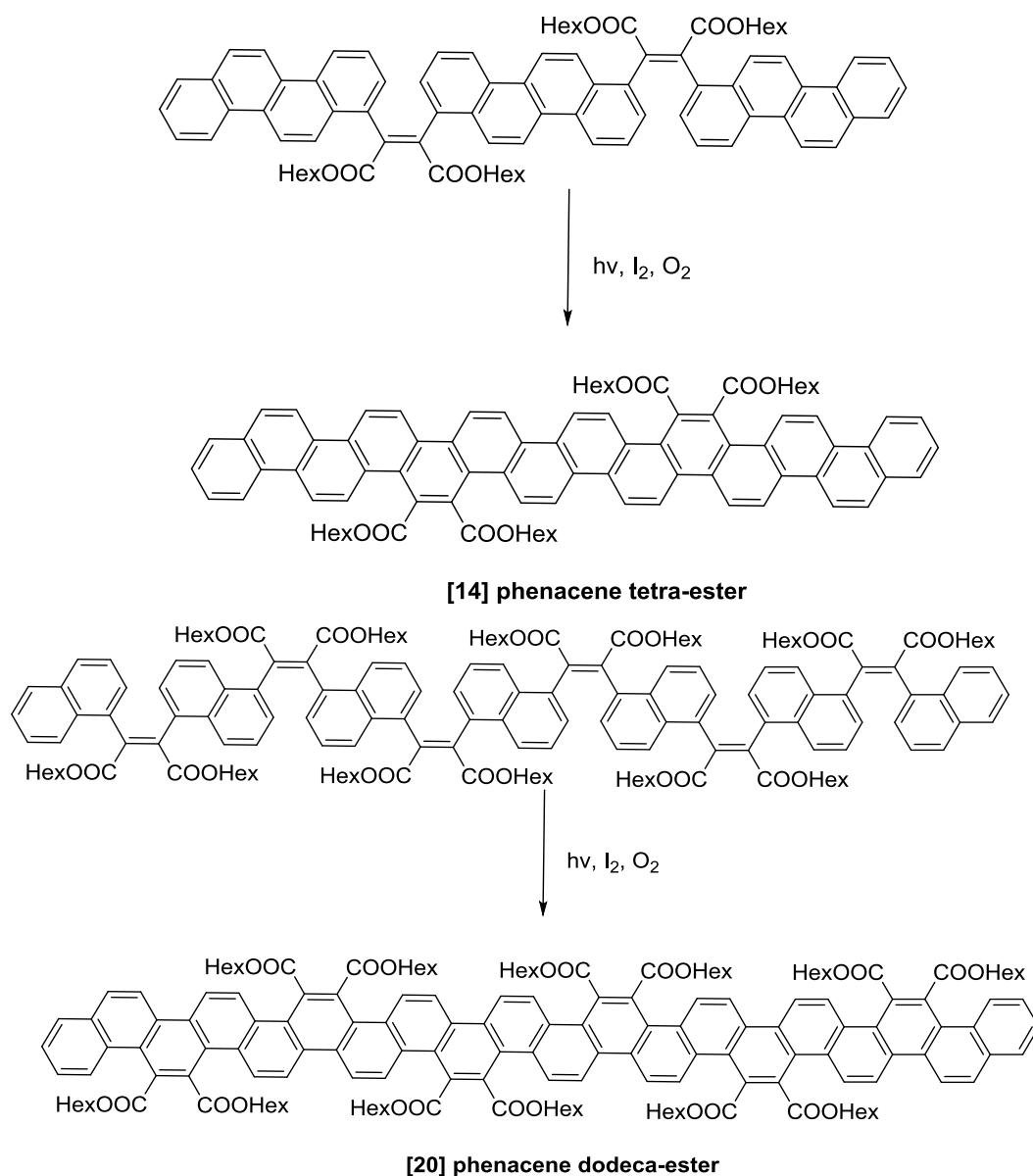


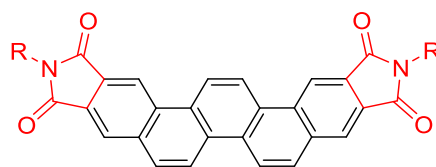
**Fig. 2-4.** Structure of [14]phenacene tetra-ester and [20]phenacene dodeca-ester.

It is expected that the introduction of peripheral functional groups into picene-type cata-condensed  $\pi$  systems is useful for further developing high-performance organic

semiconductors with sufficiently environmental stability and solution-processability because phenacenes are robust under ambient conditions.

Furthermore, little information either on synthesis of phenacene derivatives incorporating imide moieties in the long-axis directions of the molecules or on their n-type semiconductor application has so far been available. Thus, these facts have inspired us to design and develop new zigzag diimide-containing semiconductors with good processability. It is expected that incorporation of the imide groups into phenacene frameworks achieve construction of new electron-transporting materials with low-lying LUMO energy levels.

In this chapter, **C<sub>n</sub>-PicDI** ( $n = 4, 8$  and  $12$  for the chemical structures) as the first imide-incorporating picenes at both edges of the molecule were synthesized and their performance in OFETs was evaluated. In all the **C<sub>n</sub>-PicDI**s, straight alkyl chains are attached to the imide nitrogen atoms which help in ensuring adequate solubility of the products in common organic solvents. All compounds showed n-type FET behavior with moderate electron mobilities.



**C<sub>n</sub>-PicDI**

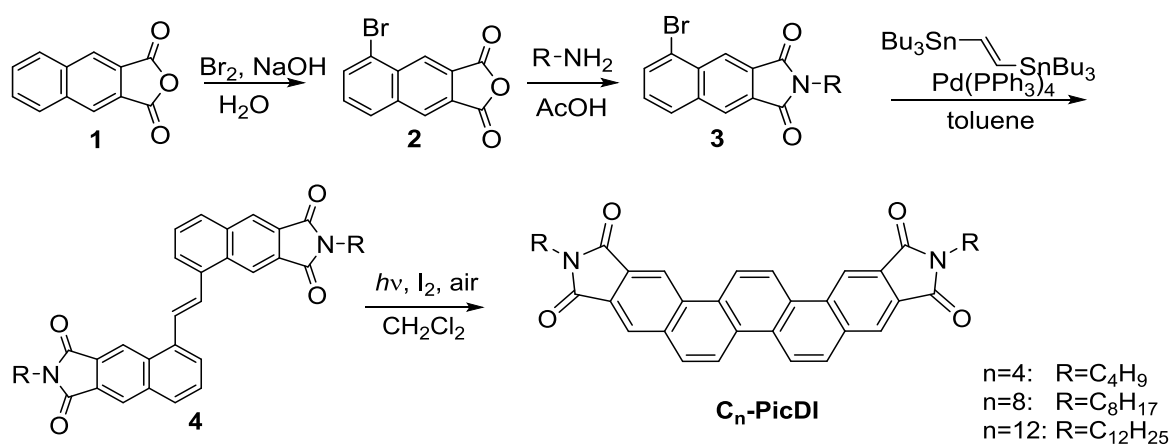
n=4: R=C<sub>4</sub>H<sub>9</sub>  
n=8: R=C<sub>8</sub>H<sub>17</sub>  
n=12: R=C<sub>12</sub>H<sub>25</sub>

**Fig. 2-5.** Structure of **C<sub>n</sub>-PicDI**s.

## 2.2 Results and Discussions

### 2.2.1 Synthesis of $C_n$ -PicDI

Detailed synthetic routes to  $C_n$ -PicDI were depicted in Scheme 2-1. All new compounds were characterized by  $^1\text{H}$  NMR,  $^{13}\text{C}$  NMR, as well as elemental analysis.

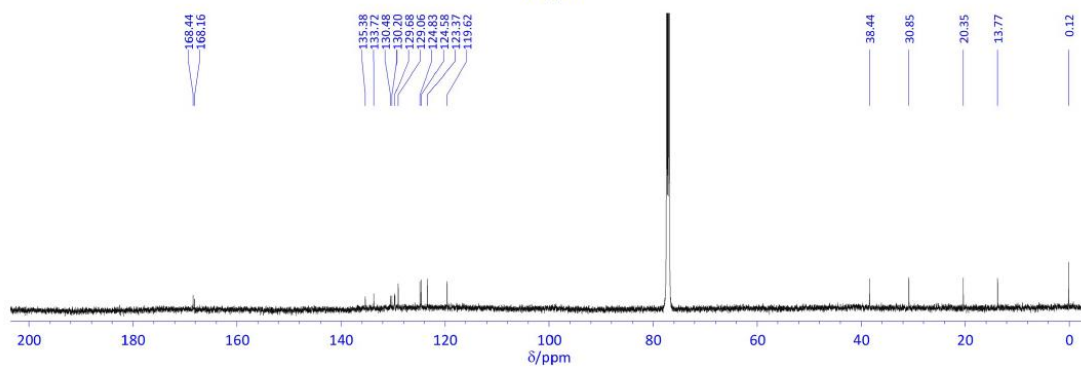
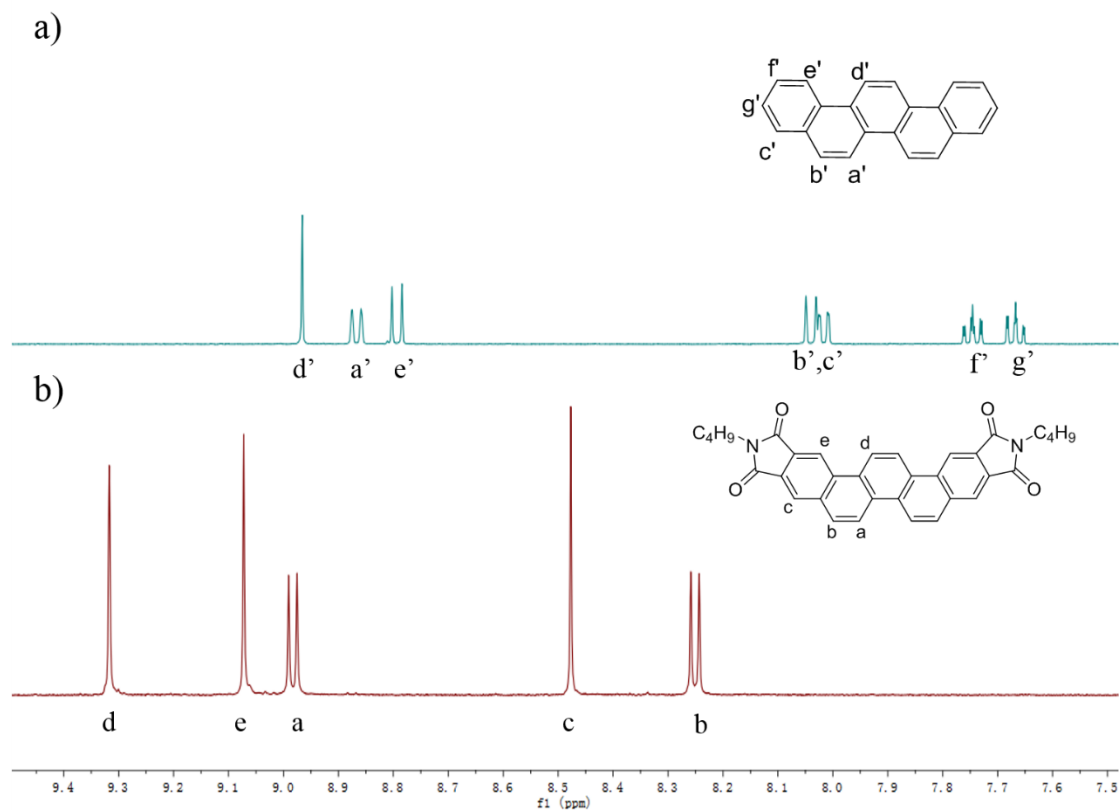


Scheme 2-1. Synthetic routes to  $C_n$ -PicDI.

$C_n$ -PicDI were synthesized by the four reactions sequence. When 2,3-naphthalenedicarboxylic anhydride was treated with bromine, there is obtained a monobromo derivative. Subsequently, reaction of **2** with appropriate primary amines in acetic acid gave **3** in moderate yields. Migita-Kosugi-Stille cross coupling of **3** with *trans*-1,2-bis(tributylstannyl)ethene in the presence of catalytic amount of  $\text{Pd}(\text{PPh}_3)_4$  in dry toluene afforded *E*-naphthylethene **4** with no isomerization of the double bond. Irradiation of **4** with  $\text{I}_2$  under aerated conditions Mallory photoreaction produced the desired  $C_n$ -PicDI in high yield.

The structure of  $C_4$ -PicDI, as a typical example, is described as follows. By comparing its  $^1\text{H}$  NMR spectral data with those for parent picene. Fig. 2-5 shows the  $^1\text{H}$  NMR spectra (aromatic region) of the two compounds. Both compounds indicate

different spectral patterns; that is, protons located at the bay region show signals at low field, whereas those at the edge of the molecule display signals in higher field. In the  $^1\text{H}$  NMR spectrum of parent picene (Fig. 2-6(a)), it is clear that the proton  $\text{H}_d$  appears as a singlet peak at 8.97 ppm, and two doublets are assigned with  $\text{H}_a$  and  $\text{H}_e$  in the bay region at 8.88 and 8.81 ppm respectively. The signals of proton  $\text{H}_b$  and  $\text{H}_c$  at the edges of picene are assigned in the region of 8.01-8.05 ppm. The signals of proton of  $\text{H}_f$  and  $\text{H}_g$  at the edge of the picene core appeared were observed in the region of 7.65-7.76 ppm. Upon introduction of imide group, the triplet signals observed for picene ( $\text{H}_g$  and  $\text{H}_f$ ) disappeared in the  $^1\text{H}$  NMR spectra of **C4-PicDI** (Fig. 2-6 (b)). The signals of  $\text{H}_c$  and  $\text{H}_e$  of **C4-PicDI** appeared as a singlet, respectively, at 8.48 and 9.07 ppm. These observations provide evidence for the presence of the imide substituents at edges of the molecules. The signals for  $\text{H}_d$  as a singlet at 9.32 ppm and for  $\text{H}_a$  as a doublet at 8.98 ppm are determined since they are located in the bay region. Additionally, the signals of **C4-PicDI**, downfield shifted compound to these for the corresponding protons of parent picenes be due to the strongly electron-withdrawing imide groups. The  $^{13}\text{C}$  NMR spectra of **C4-PicDI** are measured at 50°C and evidence for introducing imide groups was obtained as the signals for the imide carbons were clearly observed at 168.44 and 168.16 ppm.



## 2.2.2 Electronic spectra in solution and crystalline states

In order to understand electronic features of **C<sub>n</sub>-PicDI**s, the electronic spectra of **C<sub>n</sub>-PicDI**s were investigated in solution and solid phases. The UV-vis absorption spectra of **C<sub>n</sub>-PicDI**s and parent picene in  $\text{CHCl}_3$  as the reference is shown in Fig. 2-8

and their photophysical parameters, such as maximum absorption wavelengths ( $\lambda_{\text{max}}^{\text{Abs}}$ ) and molar absorption coefficients ( $\epsilon$ ), are collected in Table 2-1.

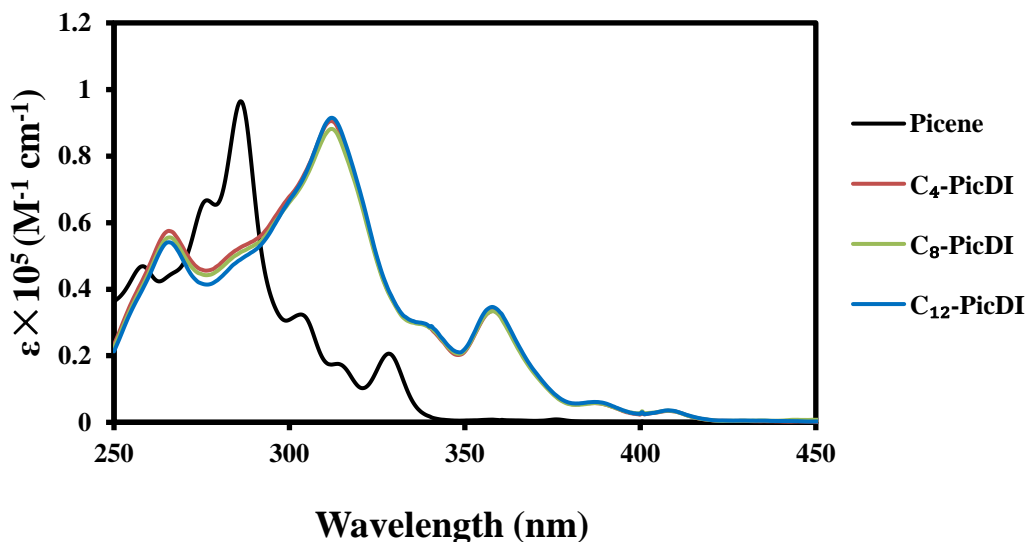


**Fig. 2-8.** Electronic absorption spectra of  $C_n$ -PicDI and parent picene in  $CHCl_3$ .

As seen from the absorption spectra (Fig. 2-8) of Picene and  $C_n$ -PicDI in  $CHCl_3$ . Parent picene showed a weak absorption band at 358 nm and 376 nm and a moderate intensity-absorption at 329 nm.  $C_n$ -PicDI showed a structured absorption band in the wavelength region of 313-408 nm (Fig. 2-8) accompanied by large  $\epsilon$  values. Additionally, the absorption curves of  $C_n$ -PicDI is the same as that of the parent picene. Therefore, the alkyl chains have a minimal effect on the electronic features of the picene core in solution.

The maximum-intensity absorption of  $C_n$ -PicDI shifted by 32 nm toward low wavelength region compared to that of parent picene. In addition, new and more intense absorption bands around 380-410 nm may reflect the difference in their electronic structures. In particular, this transition of  $C_n$ -PicDI indicates that the introduction of imide groups to the picene may enhance their transition.

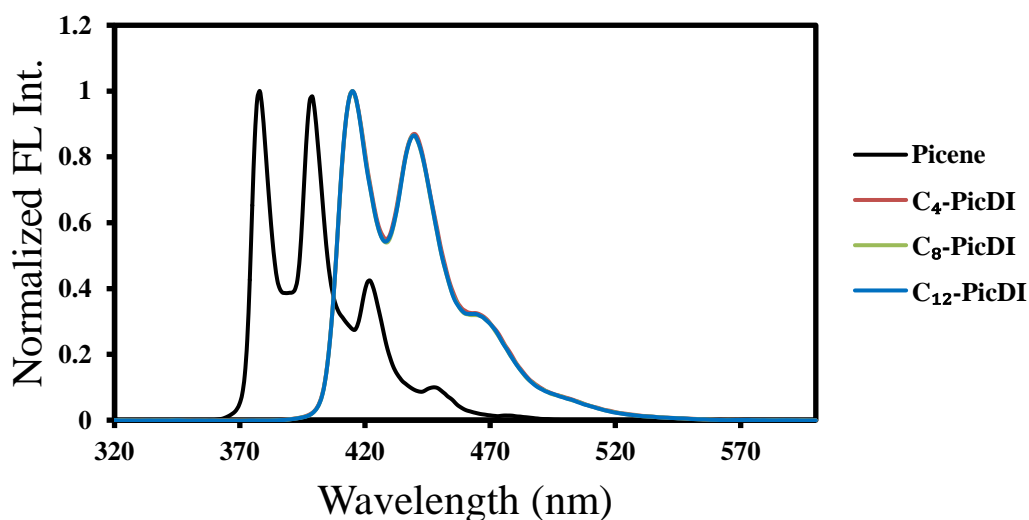


**Table 2-1.** UV-vis and Fluorescence spectra Data of **C<sub>n</sub>-PicDI**s and picene in CHCl<sub>3</sub>

compound	$\lambda_{\text{max}}^{\text{Abs}}$	$\epsilon$ ,	$\lambda_{\text{max}}^{\text{FL}}$
	nm	M <sup>-1</sup> cm <sup>-1</sup>	nm
picene	376	886	378
<b>C<sub>4</sub>-PicDI</b>	408	3445	415
<b>C<sub>8</sub>-PicDI</b>	408	3509	415
<b>C<sub>12</sub>-PicDI</b>	408	3599	415

Fig. 2-9 displays fluorescence emission spectra of **C<sub>n</sub>-PicDI**s and picene in CHCl<sub>3</sub>. Fluorescence maximum wavelength ( $\lambda_{\text{max}}^{\text{FL}}$ ) is summarized in Table 2-1. The fluorescence spectra of **C<sub>n</sub>-PicDI**s showed identical spectral features irrespective of the alkyl chain length of the imide parts and exhibited vibrational structures similar to those of parent picene.

**C<sub>n</sub>-PicDI**s showed a structured fluorescence emission band in the wavelength region of 415-440 nm. The emission band of  $\lambda_{\text{max}}^{\text{FL}}$  (= 415 nm) red-shifted by 37 nm compared to that of the parent picene ( $\lambda_{\text{max}}^{\text{FL}}$ =378 nm). The red-shifted is considered to be due to expected conjugation between the picene core and the imide moieties.

**Fig. 2-9.** Normalized fluorescence spectra of **C<sub>n</sub>-PicDI**s and parent picene in CHCl<sub>3</sub>.

Solid-state Fluorescence properties of **C<sub>n</sub>-PicDI**s were also investigated to obtain an insight into their solid states electronic features as shown in Fig. 2-10. **C<sub>4</sub>-PicDI** displayed a broad emission band with a maximum  $\lambda_{\text{max}}^{\text{FL}}$  at 486 nm. The solid-state fluorescence emission bands of **C<sub>8</sub>-PicDI** and **C<sub>12</sub>-PicDI** appeared at 498 nm and 473 nm respectively. As shown in Fig. 2-10, the profile of emission spectra of **C<sub>4</sub>-PicDI** is similar to that of **C<sub>12</sub>-PicDI**. In the case of **C<sub>8</sub>-PicDI**, the emission spectra located in the same wavelength region as that of **C<sub>4</sub>-** and **C<sub>12</sub>-PicDI**s, however, the profile of the emission band was different from that of **C<sub>4</sub>-** and **C<sub>12</sub>-PicDI**s. Upon changing the fluorescence measurement conditions from solution to solid phases, the fluorescence maximum  $\lambda_{\text{max}}^{\text{FL}}$  for **C<sub>n</sub>-PicDI**s shifted to the longer wavelength region. Thus, the difference in the fluorescence maximum wavelengths ( $\lambda_{\text{max}}^{\text{FL}}$ ) between in the solid and solution phases are determined to be 71 nm for **C<sub>4</sub>-PicDI**, 83 nm for **C<sub>8</sub>-PicDI** and 58 nm for **C<sub>12</sub>-PicDI**. The solid-state fluorescence behavior of **C<sub>n</sub>-PicDI**s is considered to be due to the presence of intermolecular interactions between adjacent molecules such as  $\pi$ - $\pi$  stacking which were affected by the alkyl chain length of the imide group in the solid state. This is a common phenomenon for rigid conjugated molecule.<sup>26, 27</sup> Unfortunately, as a single crystal of **C<sub>n</sub>-PicDI**s suitable for X-ray crystallographic analysis was not obtained, the detailed mechanism for the solid-state fluorescence behavior of **C<sub>n</sub>-PicDI** was not clearly analyzed.

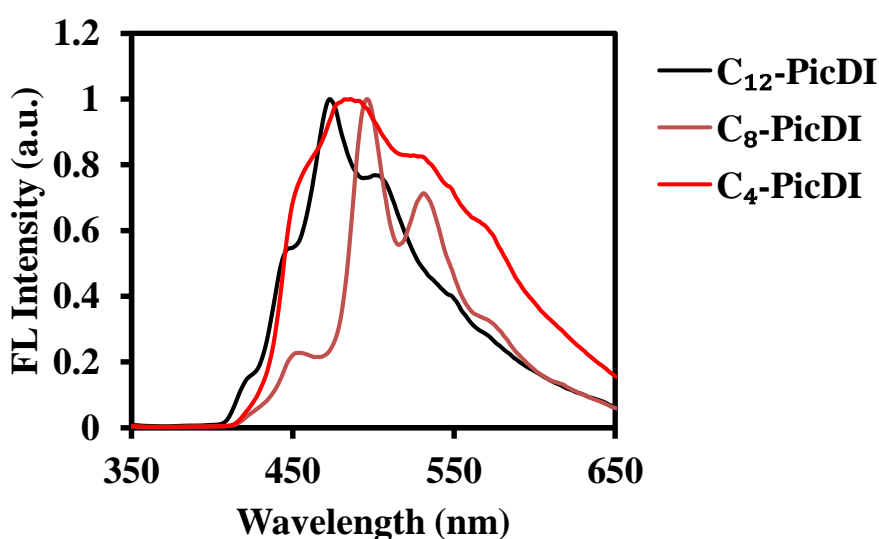
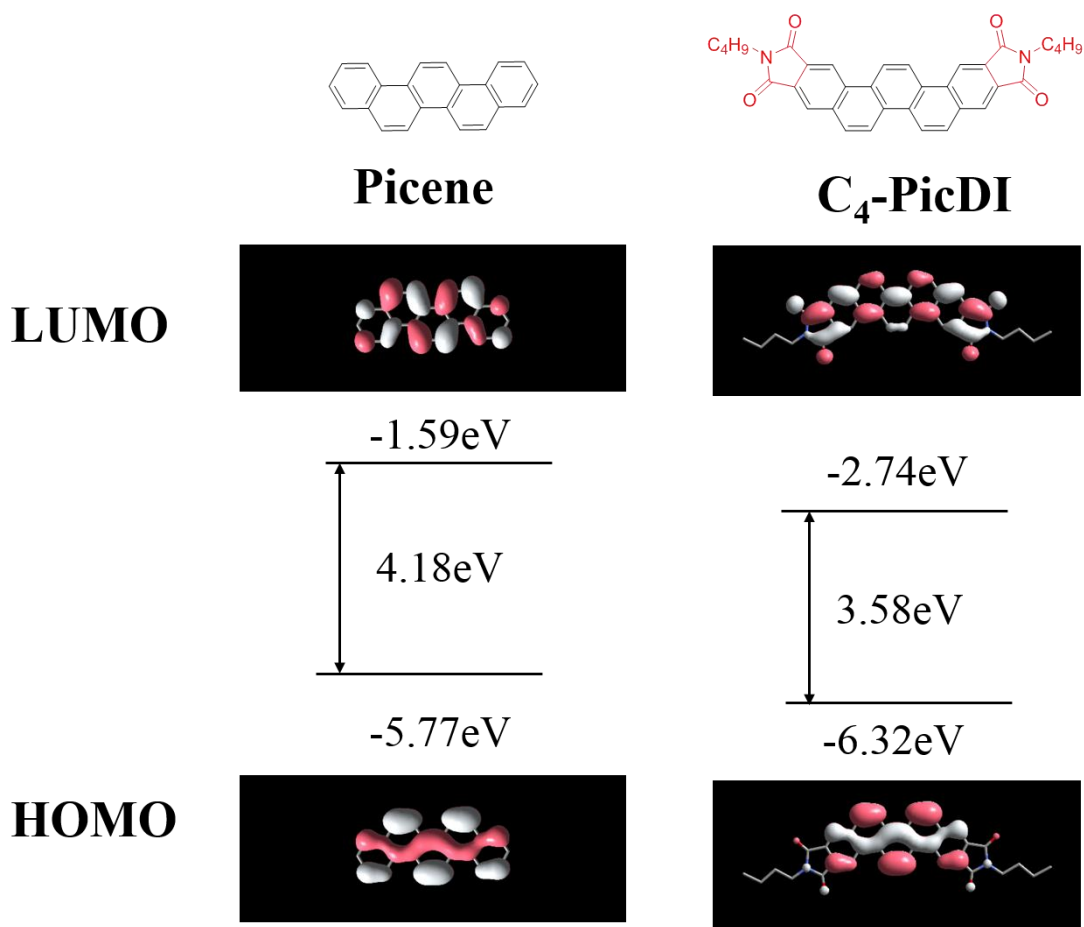


Fig. 2-10. Fluorescence spectra of **C<sub>n</sub>-PicDI**s in the solid state.

### 2.2.3 Theoretical analysis for the electronic features

To investigate the electronic structures of **C<sub>n</sub>-PicDI**s in detail, theoretical calculations were carried out with density functional theory (DFT) at the B3LYP/6-31G (d) level using Gaussian 09, Revision C. 01 package. Fig. 2-11 shows the molecular orbitals and calculated energy diagrams for parent picene and **C<sub>4</sub>-PicDI**. The shape of HOMO of **C<sub>4</sub>-PicDI** is similar to that of picene, but a small difference was observed. As seen in Fig. 2-11, the symmetry of the HOMO is the same in picene and **C<sub>4</sub>-PicDI**. However, the symmetry of the LUMO is different, *i.e.*, the LUMO in **C<sub>4</sub>-PicDI** is antisymmetrical whereas that in parent is symmetrical with respect to the C<sub>2</sub> axis of the molecules. The HOMO of **C<sub>4</sub>-PicDI** was mainly populated on the central picene core and the LUMO was located over the whole molecule including the imide molecule. Furthermore, lowering of HOMO and LUMO levels in **C<sub>4</sub>-PicDI** was clearly observed.

The energy level of LUMO and LUMO+1 orbital for **C<sub>4</sub>-PicDI** reversed compared to the case of parent picene. The energy levels LUMO (-2.74 eV) and LUMO+1 (-2.60 eV) in **C<sub>4</sub>-PicDI** were much lower than those for picene (LUMO = -1.59 eV, LUMO+1 = -1.51 eV). These results suggest that the introduction of the electron-withdrawing imide moieties into **C<sub>4</sub>-PicDI** induces the effect of stabilizing the LUMO orbital through the efficient conjugation. The substitution effectively interacted with the picene core in **C<sub>4</sub>-PicDI** to modify the molecular orbital levels. As a result, LUMO were slightly delocalized onto the imide groups, the LUMO of **C<sub>4</sub>-PicDI** has less nodal planes along the long axis of the molecule compared to parent picene. It is thus expected that **C<sub>n</sub>-PicDI**s effectively interact between the neighboring molecules in the solid state under n-type operation conditions.



**Fig. 2-11.** Frontier molecular orbital surfaces of picene and **C<sub>4</sub>-PicDI** calculated at the B3LYP/6-31+G(d) level.

## 2.2.4 Structures and electronic properties of **C<sub>n</sub>-PicDI**s in thin films

We investigated a thin film of **C<sub>n</sub>-PicDI**s formed on SiO<sub>2</sub> substrates based on XRD patterns are shown in Fig. 2-12. Only 00 $l$  reflections were observed in the XRD patterns, suggesting that the  $ab$ -plane, is laying parallel to the surface of SiO<sub>2</sub>. Thus, the normal direction to the SiO<sub>2</sub> surface is consistent with the reciprocal lattice vector,  $c^*$  in the thin films of **C<sub>n</sub>-PicDI**s. Such a molecular alignments of **C<sub>n</sub>-PicDI**s in  $ab$ -plane without any particular treatment is significant because the channel conductance should take place in the  $ab$ -plane, based on the analogy of molecular structure. The  $|c^*|^{-1}$  values which indicate interlayer distances between the  $ab$ -planes

values, were determined to be 22.94(7) Å for **C<sub>4</sub>-PicDI**, 31.0(1) Å for **C<sub>8</sub>-PicDI** and 37.1(6) Å for **C<sub>12</sub>-PicDI** in the thin films produced by thermal deposition. Therefore, it was concluded that **C<sub>n</sub>-PicDI**s incline by 30°, 29° and 32° with respect to the *c*\* axis. The inclined angle is almost the same as that of unsubstituted picene and (C<sub>14</sub>H<sub>29</sub>)<sub>2</sub>-picene,<sup>13</sup> suggesting that the addition of the imide groups provided minimal effects on the solid state molecular alignment. As expected from the solid state structures, channel conductance is expected to occur in the *ab*-plane, as in the cases of unsubstituted picene and the related compounds.

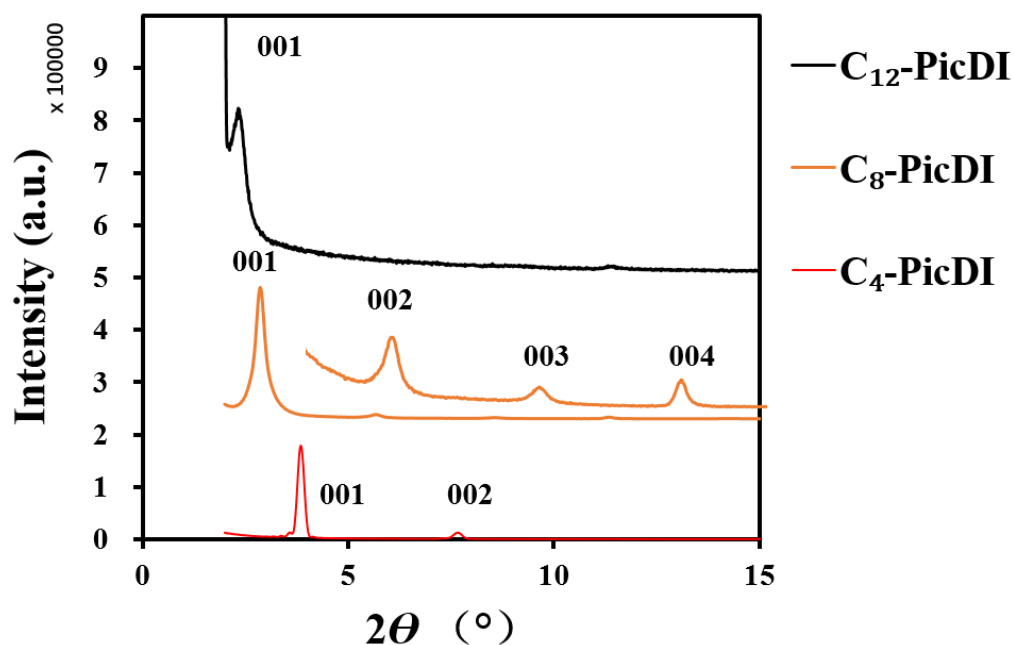


**Fig. 2-12.** XRD patterns of thin films of **C<sub>n</sub>-PicDI**s formed on an SiO<sub>2</sub> substrate.

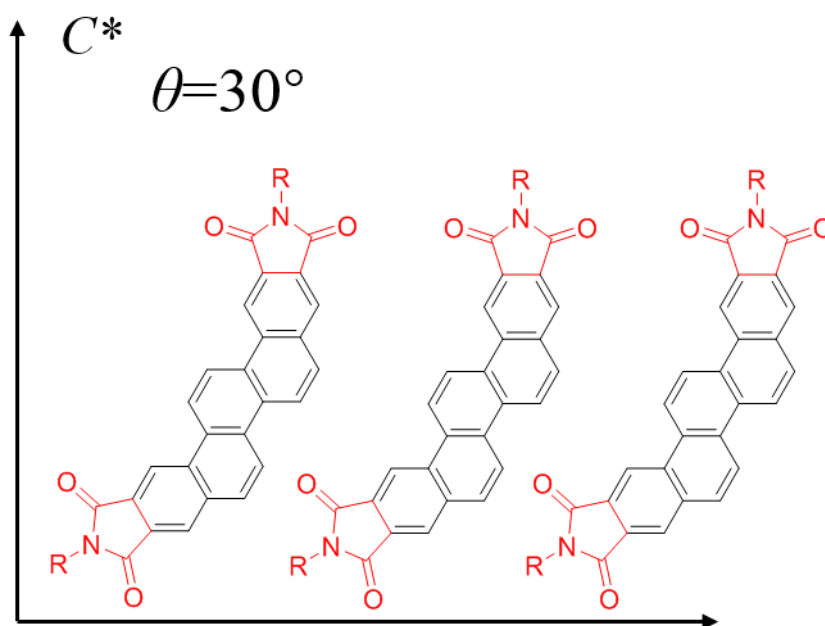


**Fig. 2-13.** Orientation of the long axis of the **C<sub>n</sub>-PicDI**s with respect to the *c*\* axis (normal to the *ab* plane) in the thin film formed on a SiO<sub>2</sub> substrate.

The photoelectron yield spectroscopy (PYS) results of thin films of **C<sub>n</sub>-PicDI**s formed on SiO<sub>2</sub>/Si substrate showed the rising onsets of the spectrum from which HOMO levels was estimated. The HOMO levels of the molecules were estimated to be 6.63 eV for **C<sub>4</sub>-PicDI**, 6.80 eV for **C<sub>8</sub>-PicDI** and 6.91 eV for **C<sub>12</sub>-PicDI** respectively. The onset energy of **C<sub>n</sub>-PicDI**s slightly increased with an increase in the alkyl chain length, indicating that the HOMO level was affected by the alkyl chain lengths in the solid state.

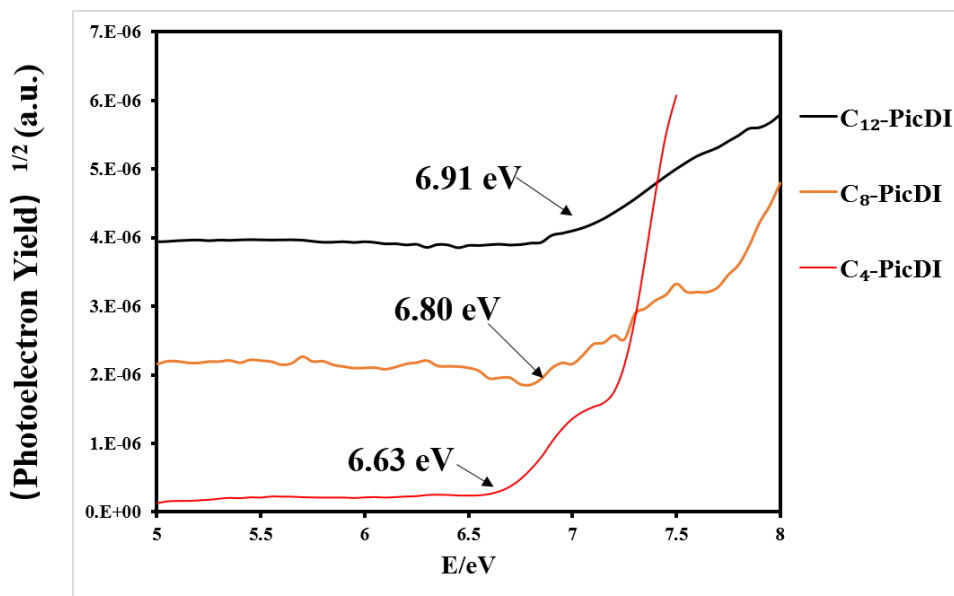


**Fig. 2-14.** PYS spectra of thin film of **C<sub>n</sub>-PicDI**s formed on SiO<sub>2</sub>/Si substrate.

The optical band gaps of **C<sub>n</sub>-PicDI**s were estimated to be 2.87 eV for **C<sub>4</sub>-PicDI**, 2.90 eV for **C<sub>8</sub>-PicDI** and 2.92 eV for **C<sub>12</sub>-PicDI** from the onsets of the respective spectra. The onset energy increased slightly from 2.87 eV to 2.92 eV with an increase in the alkyl chain length, indicating that the HOMO-LUMO gap does not significantly change with changing the alkyl chains. The HOMO-LUMO gap for **C<sub>n</sub>-PicDI**s show the values are much lower than that of picene. Thus, **C<sub>n</sub>-PicDI**s may exhibit more ordered molecular packing to achieve an efficient charge transport. These results can be understood if it is considered that the introduction of the imide groups into the both edges directly affects the frontier orbitals of the picene core.

Based on these analyses in addition to the above-mentioned PYS and absorption spectra in thin films, the energy diagram of the **C<sub>n</sub>-PicDI**s are determined and illustrated in Fig. 2-15. The data for picene<sup>12</sup> and **PTCDI-C8** are shown as the references. As seen from Fig. 2-15, the energy diagram of picene shows energy difference of 0.6 eV between the  $E_F$  of Au and HOMO of picene, while the difference between LUMO of picene and  $E_F$  of Au is much larger than 0.6 eV. The small energy difference between  $E_F$  and HOMO is consistent with previous observed p-type FET properties.<sup>28</sup> However, the LUMO energy levels of **C<sub>n</sub>-PicDI**s were in the range of -3.76 eV to -3.99 eV similar to that of **PTCDI-C8** (-4.3 eV), which were much lower

that of picene. The low LUMO energy level was clearly derived from the strongly electron withdrawing imide moieties on the edges of picene core. The imide moieties effectively interact with the electronic core of picene in **C<sub>n</sub>-PicDI**s as suggested by DFT calculations to modify the molecular orbital energy level. Therefore, it is expected that **C<sub>n</sub>-PicDI**s are potential n-type OFET materials.

The n-type semiconducting operation is predicted for all **C<sub>n</sub>-PicDI**s from their characteristic electronic structures; that is, the low LUMO energy level would make their n-type operation possible. Moreover, the large energy gap would provide a clear on-off switch ability in OFET devices.

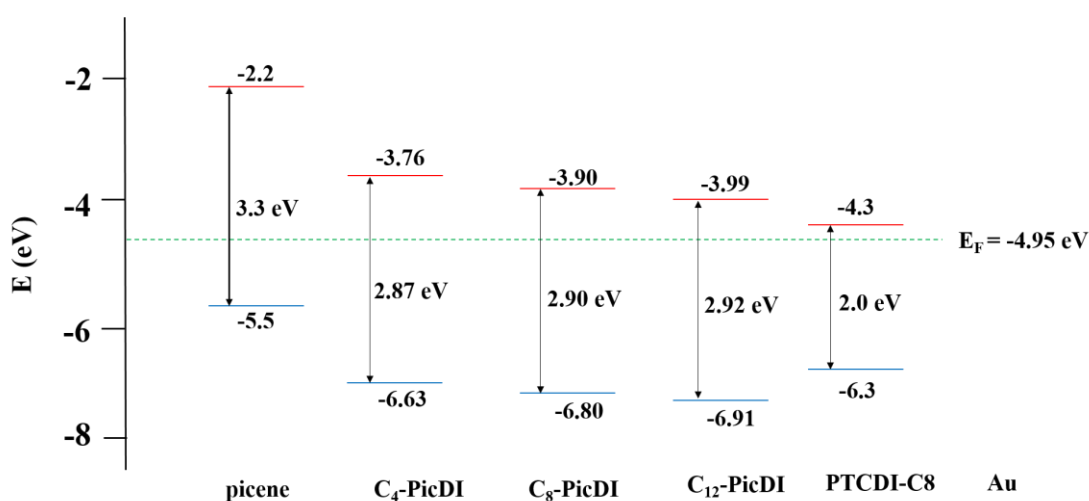


**Fig. 2-15.** Energy diagrams for HOMO and LUMO of picene, **C<sub>n</sub>-PicDI**s, and **PTCDI-C8** experimentally determined by PYS and electronic absorption spectra in thin films.

### 2.2.5 FET characteristics of **C<sub>n</sub>-PicDI**s

Subsequently, the semiconducting properties of these **C<sub>n</sub>-PicDI**s were examined in OFET devices. The devices were typical top-contact bottom-gate configuration, which was suitable for characterizing thermally evaporated electron-transporting semiconductors.<sup>29</sup> During the device fabrication, the 2,3,5,6-tetrafluorotetrac-



yanoquinodimethane (F4TCNQ) dielectric layer was introduced between the active layer and source(S)/drain(D) electrodes to reduce contact resistance.

The device structure of the **C<sub>n</sub>-PicDI**s thin-film FET with a ZrO<sub>2</sub> gate dielectric is shown in Fig. 2-16. 150 nm thick ZrO<sub>2</sub> was used as the gate dielectric, and the capacitance per area,  $C_0$ , was determined to be 38.9 nF cm<sup>2</sup>, as determined by the extrapolation of  $C_0$  recorded at 20-1000 Hz to 0 Hz. The transfer and output curves of all devices were characterized under Ar atmosphere.

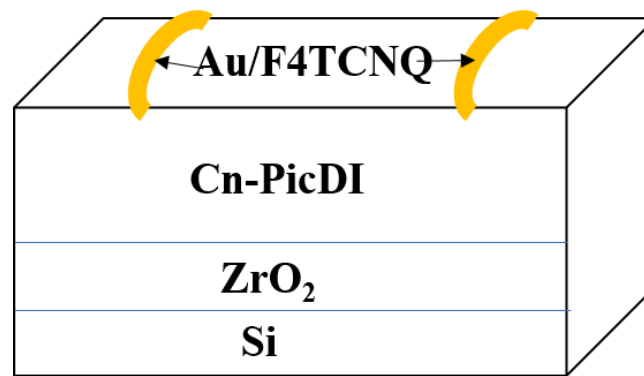


**Fig. 2-16.** Device structure of **C<sub>n</sub>-PicDI** FETs.

The absolute drain current,  $|I_D|$ , increased with the applied of the positive gate voltage,  $V_G$ . The value of  $|I_D|$  increases with an increase in  $|V_G|$ , under the condition that the drain voltage  $V_D$  was fixed at 26 V. The transfer curve for **C<sub>4</sub>-PicDI** (Fig. 2-17 (a)) indicates clear n-type operation; upon applying positive  $V_G$ , increasing drain current  $|I_D|$  was detected. The output curves,  $|I_D|$ - $|V_D|$  plots, at different positive  $V_G$  values provided typical normally-off properties (Fig.2-17 (b)), indicating that the **C<sub>4</sub>-PicDI** thin film FET exhibits n-type normally-off FET properties. The values of  $\mu$ ,  $|V_{th}|$ , on/off ratio and S were respectively determined to be  $2.7 \times 10^{-4}$  cm<sup>2</sup> V<sup>-1</sup> s<sup>-1</sup>, 20.0 V,  $1.21 \times 10^2$ , 3.9 V decade<sup>-1</sup> for **C<sub>4</sub>-PicDI**.

Table 2-2 lists the FET parameters of the **C<sub>4</sub>-PicDI** thin-film with a ZrO<sub>2</sub> gate dielectric. The averaged values of  $\mu$ ,  $|V_{th}|$ , on/off ratio and S were  $2(1) \times 10^{-4}$  cm<sup>2</sup> V<sup>-1</sup> s<sup>-1</sup>, 19(1) V,  $1.0(4) \times 10^2$ , 4.3(7) V decade<sup>-1</sup>, respectively, the averaged values were obtained from four FET devices.

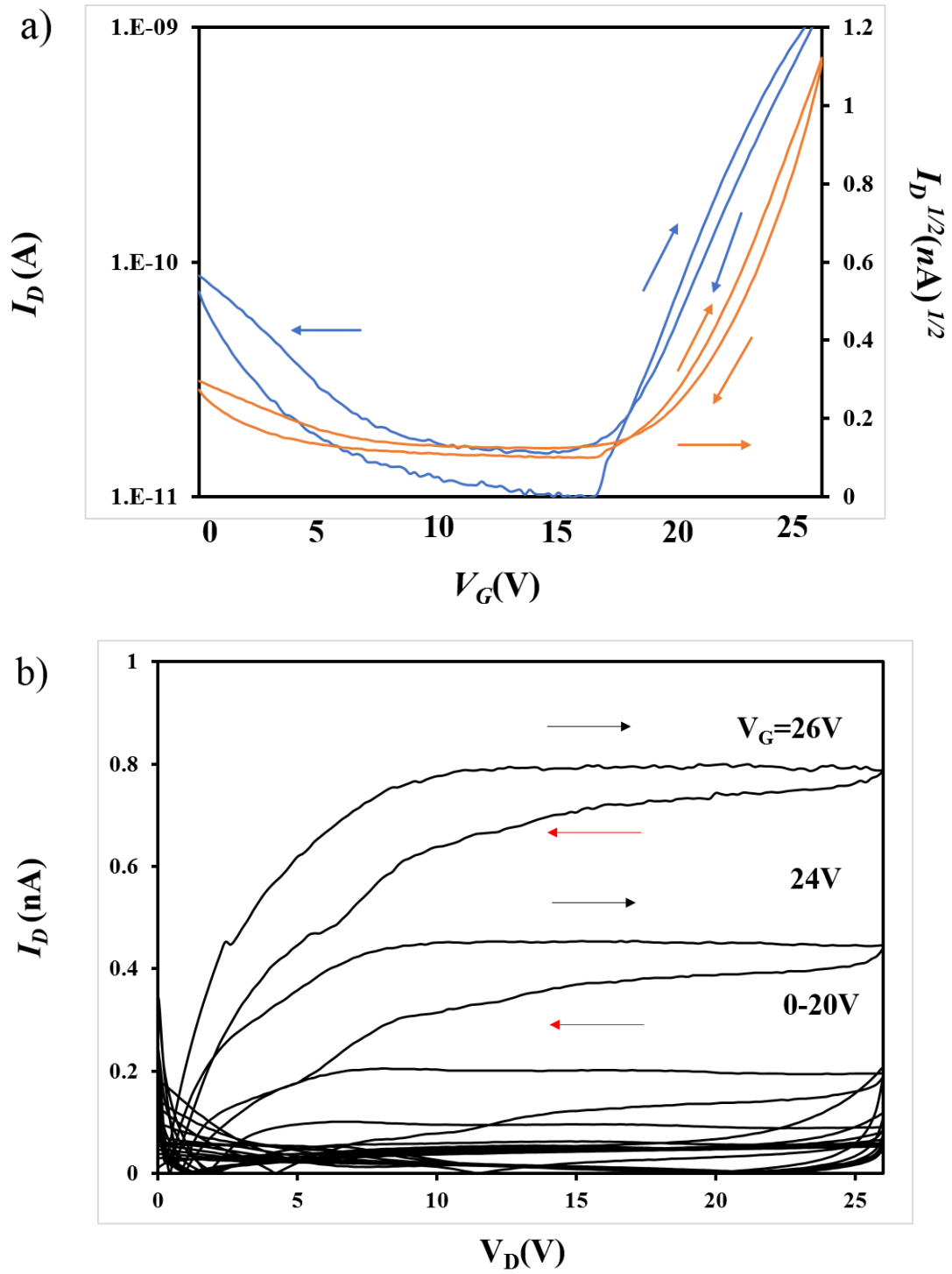


**Fig. 2-17.** Transfer curves (a) and output curves (b) of C4-PicDI thin-film FET.

**Table 2-2** FET parameters of **C4-PicDI** thin-film FET with ZrO<sub>2</sub> gate dielectric

Sample	$\mu$ (cm <sup>2</sup> V <sup>-1</sup> s <sup>-1</sup> )	$V_{th}$ (V)	On/off	S (V per decade)
#1	$2.4 \times 10^{-4}$	19.4	$1.3 \times 10^2$	4.1
#2	$2.7 \times 10^{-4}$	20.0	$1.2 \times 10^2$	3.9
#3	$1.2 \times 10^{-4}$	17.7	$0.45 \times 10^2$	5.3
#4	$0.75 \times 10^{-4}$	17.8	$1.2 \times 10^2$	4.1
Average	$2(1) \times 10^{-4}$	19(1)	$1.0(4) \times 10^2$	4.3(7)

Subsequently, the transfer and output curves of the **C8-PicDI** thin-film FET with a ZrO<sub>2</sub> gate dielectric were observed and the characteristics were shown in Fig. 2-18, The **C8-PicDI**-based FET also showed n-type operation. The output curves,  $|I_D|$ - $|V_D|$  plots, at different positive  $V_G$  values provided typical normally-off properties. The values of  $\mu$ ,  $|V_{th}|$ , on/off ratio and S were determined to be  $2.0 \times 10^{-1}$  cm<sup>2</sup> V<sup>-1</sup> s<sup>-1</sup>, 20.4V,  $2.6 \times 10^4$ , 0.890 V decade<sup>-1</sup> for **C8-PicDI**, respectively. The FET parameters of the **C8-PicDI** thin-film FETs measured in this study are listed in Table 2-3. The averaged values of  $\mu$  was  $1.0(6) \times 10^{-1}$  cm<sup>2</sup> V<sup>-1</sup> s<sup>-1</sup> which was determined from seven devices. The  $\mu$  value of **C8-PicDI** thin-film FET, is three orders of magnitude higher than that for **C4-PicDI** ones. The  $|V_{th}|$ , on/off ratio and S were 20(2) V,  $3(2) \times 10^4$ , 1.3(4) V decade<sup>-1</sup>, respectively. Thus, it was found that the FET performance of the FETs with **C8-PicDI** is relatively high displaying  $\mu$  values comparable to that for **PTCDI-C8**.<sup>23</sup>

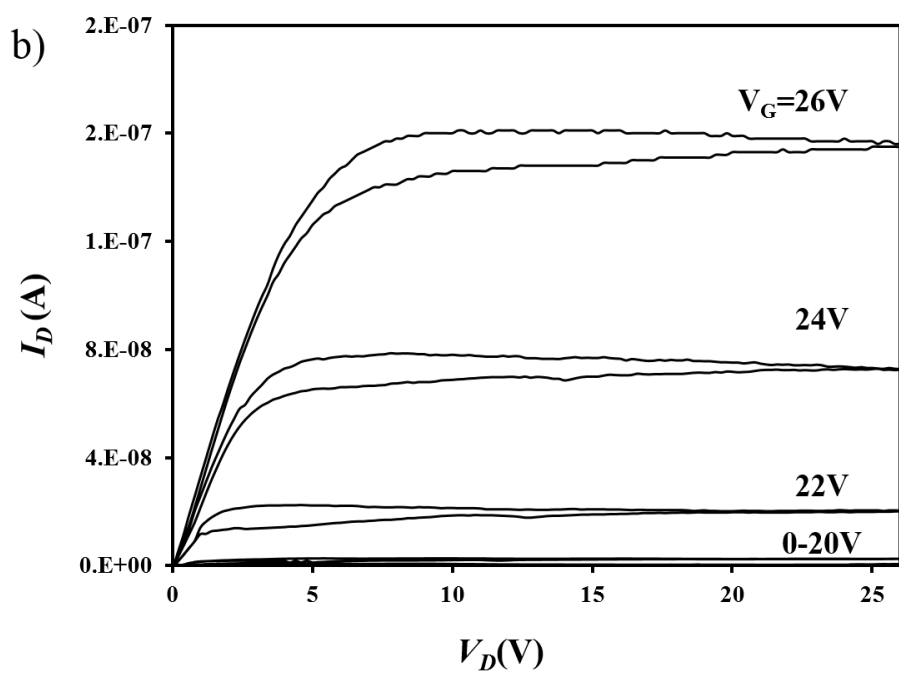
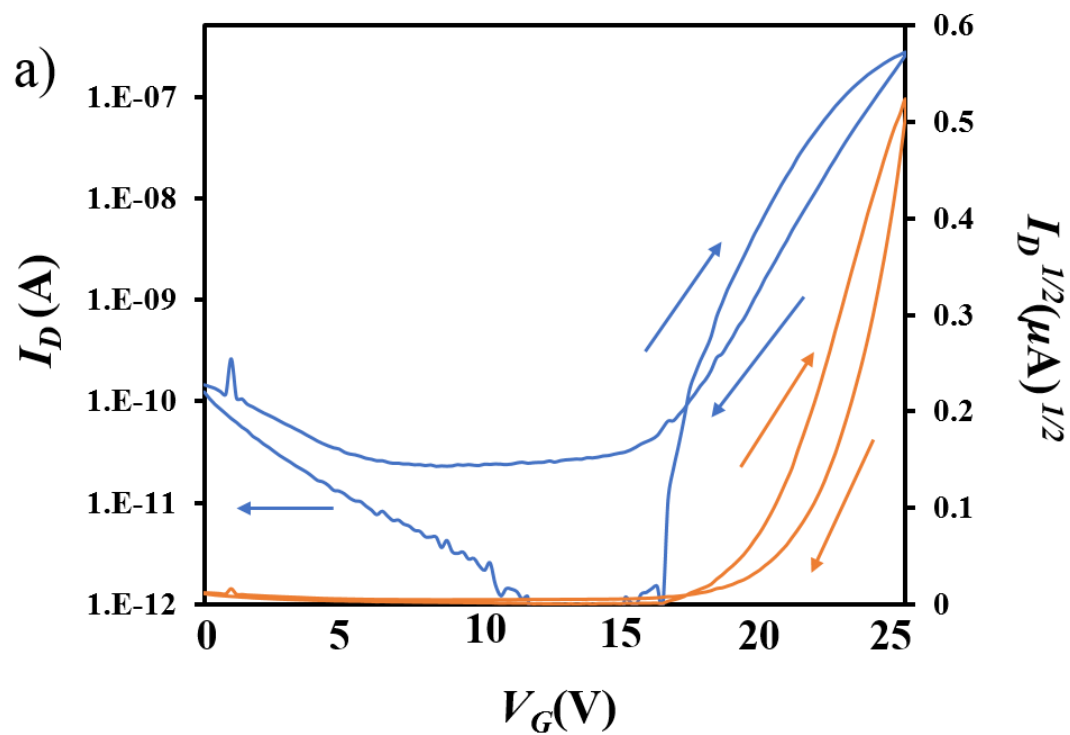


**Fig. 2-18.** Transfer curves (a) and Output curves (b) of C8-PicDI FET.

**Table 2-3.** FET parameters of **C<sub>8</sub>-PicDI** thin-film FET with ZrO<sub>2</sub> gate dielectric

Sample	$\mu$ (cm <sup>2</sup> V <sup>-1</sup> s <sup>-1</sup> )	$V_{th}$ (V)	On/off	S (V per decade)
#1	$0.64 \times 10^{-1}$	18.8	$2.0 \times 10^4$	1.87
#2	$1.4 \times 10^{-1}$	17.2	$6.4 \times 10^4$	1.08
#3	$0.95 \times 10^{-1}$	17.5	$3.7 \times 10^4$	1.24
#4	$0.22 \times 10^{-1}$	20.0	$1.0 \times 10^4$	1.78
#5	$2.0 \times 10^{-1}$	20.4	$2.6 \times 10^4$	0.890
#6	$0.98 \times 10^{-1}$	21.5	$1.5 \times 10^4$	1.05
#7	$1.0 \times 10^{-1}$	21.5	$1.7 \times 10^4$	1.00
Average	$1.0(6) \times 10^{-1}$	20(2)	$3(2) \times 10^4$	1.3(4)

The drain current,  $|I_D|$ , increased with the application of the positive gate voltage,  $V_G$ , in the same manner as cases of **C<sub>n</sub>-PicDI** ( $n = 4, 8$ ) thin-film FET with a ZrO<sub>2</sub> gate dielectric. The value of  $|I_D|$  increases with an increase in  $|V_G|$ , under the condition where drain voltage  $V_D$  was fixed at 26 V, showing a low-voltage operation. The transfer curve (Fig. 2-19) shows clear n-type operation. The output curves,  $|I_D|$ - $|V_D|$  plots at different positive  $V_G$  values, showed typical normally-off properties. The values of  $\mu$ ,  $|V_{th}|$ , on/off ratio and S were determined to be  $1.9 \times 10^{-2}$  cm<sup>2</sup> V<sup>-1</sup> s<sup>-1</sup>, 20.5 V,  $3.3 \times 10^4$ , 1.6 V decade<sup>-1</sup> for **C<sub>12</sub>-PicDI** respectively, indicating n-type normally-off FET properties. Table 2-4 lists the FET parameters of the **C<sub>12</sub>-PicDI** thin-film FET with a ZrO<sub>2</sub> gate dielectric. The averaged values of  $\mu$ ,  $|V_{th}|$ , on/off ratio and S were  $1.4(3) \times 10^{-2}$  cm<sup>2</sup> V<sup>-1</sup> s<sup>-1</sup>, 19(1) V,  $5(4) \times 10^4$ , 1.6(4) V decade<sup>-1</sup>, respectively; the averaged values were obtained from eight FET devices. The averaged  $\mu$  value,  $1.4(3) \times 10^{-2}$  cm<sup>2</sup> V<sup>-1</sup> s<sup>-1</sup>, was close to that of **C<sub>8</sub>-PicDI** FET and two orders of magnitude higher than that of **C<sub>4</sub>-PicDI** FET.

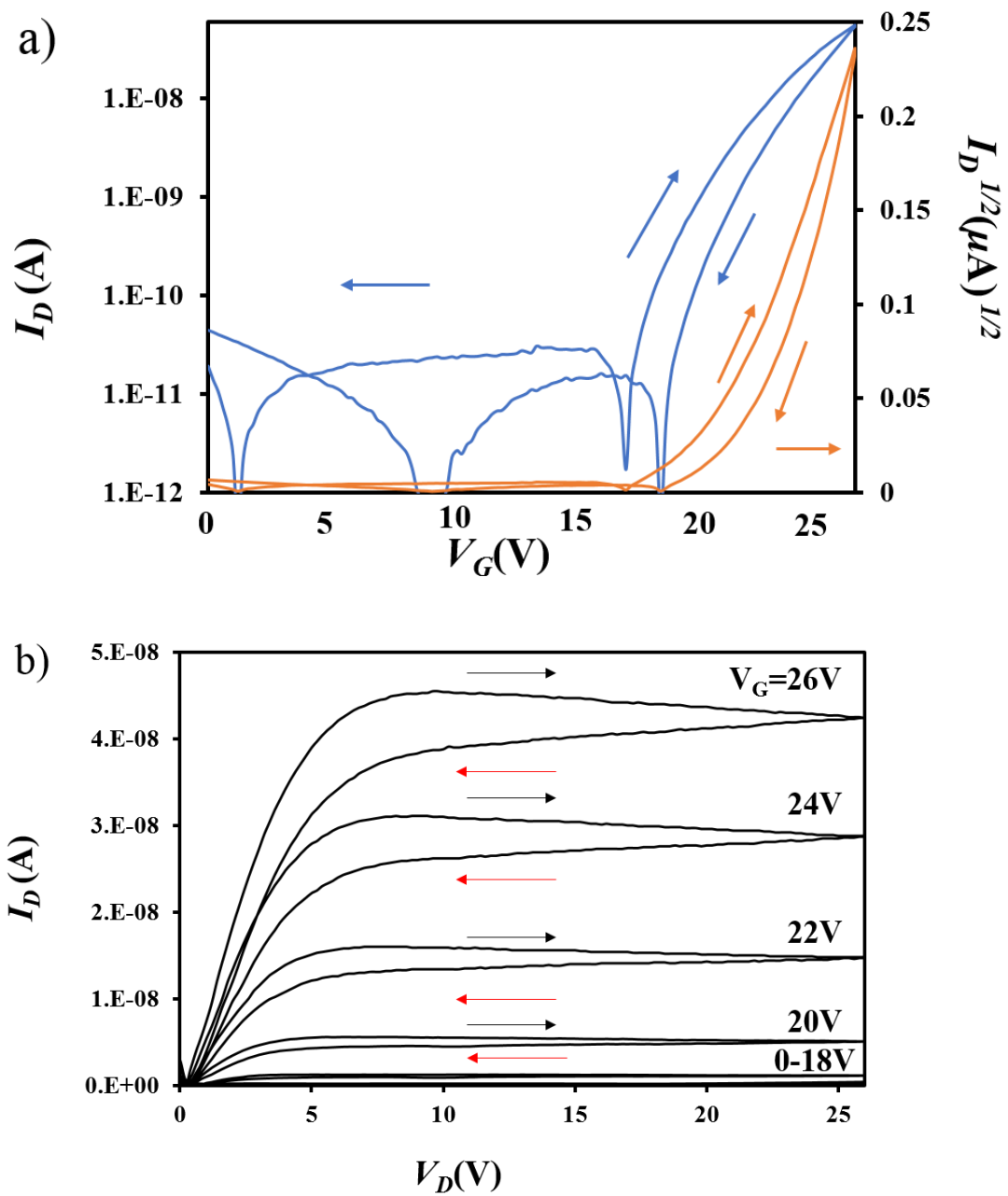


**Fig. 2-19.** Transfer curves (a) and output curves (b) of C<sub>12</sub>-PicDI FET.

**Table 2-4.** FET parameters of **C<sub>12</sub>-PicDI** thin-film FET with ZrO<sub>2</sub> gate dielectric

Sample	$\mu$ (cm <sup>2</sup> V <sup>-1</sup> s <sup>-1</sup> )	$V_{th}$ (V)	On/Off	S (V per decade)
#1	$1.5 \times 10^{-2}$	17.9	$11 \times 10^4$	1.0
#2	$0.97 \times 10^{-2}$	18.0	$11 \times 10^4$	1.7
#3	$1.1 \times 10^{-2}$	18.2	$1.5 \times 10^4$	1.2
#4	$1.8 \times 10^{-2}$	20.2	$0.56 \times 10^4$	2.1
#5	$1.9 \times 10^{-2}$	20.5	$3.3 \times 10^4$	1.6
#6	$1.4 \times 10^{-2}$	20.1	$3.3 \times 10^4$	1.8
#7	$1.5 \times 10^{-2}$	19.5	$4.2 \times 10^4$	1.4
#8	$1.3 \times 10^{-2}$	20.9	$2.0 \times 10^4$	1.7
Average	$1.4(3) \times 10^{-2}$	19(1)	$5(4) \times 10^4$	1.6(4)

The highest performance FET parameters observed in the present study for **C<sub>n</sub>-PicDI**-based FETs are collected in Table 2-5. The above  $\mu$  value for **C<sub>8</sub>-PicDI**-based FETs is relatively high for n-type organic thin-film FETs. At the present stage, **C<sub>8</sub>-PicDI** provides the highest  $\mu$  value among the **C<sub>n</sub>-PicDI**s studied. The lower energy level of LUMO and better crystallinity in **C<sub>8</sub>-PicDI** may provide the better FET properties than those for **C<sub>4</sub>-PicDI** and **C<sub>12</sub>-PicDI**. Therefore, **C<sub>8</sub>-PicDI** is the best material for n-type FET operation among **C<sub>n</sub>-PicDI**s molecules. The length of the alkyl chain is considered to be significant for realizing the improvement of the  $\mu$  value. The octyl chains is considered to appropriately control the molecular aggregation in the solid state.

**Table 2-5.** The highest performances observed for **C<sub>n</sub>-PicDI**s thin-film FET with ZrO<sub>2</sub> gate dielectric

Sample	$\mu$ (cm <sup>2</sup> V <sup>-1</sup> s <sup>-1</sup> )	$V_{th}$ (V)	On/Off	S (V decade <sup>-1</sup> )
<b>C4-PicDI</b>	$2.69 \times 10^{-4}$	20	121	3.85
<b>C8-PicDI</b>	$2.11 \times 10^{-2}$	19.7	5590.2	1.58
<b>C12-PicDI</b>	$1.86 \times 10^{-2}$	20.5	32497.9	1.60

It should be noted that significant hysteresis between forward and reverse transfer curves is presumably due to a bias stress effect produced by non-hydrophobic surface of gate dielectric. Actually, the surface of SiO<sub>2</sub> was treated by parylene to provide the hydrophobic surface, but the surface treatment by parylene may not lead to a sufficient hydrophobic surface to make the hysteresis disappear. This must be further ameliorated.



## 2.3 Conclusion

A series of high-performance n-type semiconductors were constructed based on imide functionalized picene derivatives. It was found that the Mallory photoreaction enabled synthesized the molecules. **C<sub>n</sub>-PicDI**s are, the first phenacene derivatives possessing imide moieties in the long-axis direction of the phenacene framework. The molecule structure of **C<sub>n</sub>-PicDI**s are confirmed by <sup>1</sup>H NMR, <sup>13</sup>C NMR and element analysis. As for the molecular alignment in thin films on a ZrO<sub>2</sub>/Si substrate, the molecules stood with an inclined angle about 30° to retain aromatic π-π interactions along with the long axis of the molecules. It was revealed that **C<sub>n</sub>-PicDI**s served as the active layer of n-type FET devices with high electron mobility. The highest μ value of **C<sub>n</sub>-PicDI** was 2.0×10<sup>-1</sup> cm<sup>2</sup> V<sup>-1</sup> s<sup>-1</sup> for **C<sub>8</sub>-PicDI** based FET, which was comparable to μ values for FET device of **PTCDI-C8** which is one of the benchmarks n-type compounds. The present result represents a novel strategy for designing electron transporting materials. The facile synthesis of the chemically modified π-extended phenacenes will enable the development of a future FET material for ultra-high-performance organic FETs.

## 2.4 Experimental Section

### General procedures

$^1\text{H}$  NMR and  $^{13}\text{C}$  NMR spectra were measured on VARIAN Mercury 400 (400 MHz) and VARIAN NMR System 600 (600 MHz) spectrometers. Elemental analyses were performed by using Perkin-Elmer 2400II CHN-S analyzer at the Micro Elemental Analysis Laboratory of Okayama University. In the spectral measurements, spectroscopic grade solvents were used at ambient conditions (The  $^{13}\text{C}$  NMR spectra of **C<sub>4</sub>-PicDI** was measured at 50°C). The UV-vis absorption spectra were recorded on a JASCO V-530 spectrophotometer. The fluorescence emission spectra were measured on a JASCO 5300 spectrophotometer. The high-resolution mass spectral analyses (FAB) were calculated by using JEOL JMS-700 MStation spectrometer at Institute for Materials Chemistry and Engineering, Kyushu University.

The theoretical calculations of were performed by using density functional (DFT) theory, PBE0 or B3LYP functionals and 6-311+G(d,p) basis set in a vacuum. In this study, all theoretical calculations were carried out by using the software GAUSSIAN 09 Revision C. 01 package.

Photoelectron yield spectroscopy (PYS) of the films of **C<sub>n</sub>-PicDI**s was measured at room temperature using a PYS spectrometer (Bunko-keiki BIP-KV201). For the measurement of the PYS spectra, a 60-nm film of **C<sub>n</sub>-PicDI**s was formed on a SiO<sub>2</sub>/Si substrate.

The X-ray diffraction (XRD) patterns of thin films of **C<sub>n</sub>-PicDI**s were measured with CuK $\alpha$  (wavelength  $\lambda$ = 1.5418 Å) using a RIGAKU SMARTLAB-PRO at room temperature. For the XRD measurements, a 60-nm thin film of **C<sub>n</sub>-PicDI**s was formed on the SiO<sub>2</sub>/Si substrate by thermal deposition under 10<sup>-7</sup> Torr.

**4-Bromo-2,3-naphthalenedicarboxylic anhydride (2):** Br<sub>2</sub> (1 mL, 19.4 mmol) was dropped into a mixture of 2,3-dicarboxylic anhydride **1** (2.0 g, 10.1 mmol) in a

solution of 1 mM aqueous NaOH dropwise. Subsequently the reaction mixture was refluxed for about 16 h and then allowed to cool to room temperature and the solid was collected by filtration. The solid was dissolved in CH<sub>3</sub>OH/H<sub>2</sub>O (v: v = 1:1) and adjusted pH to 1.5 by adding conc. HCl. The resulting mixture was extracted with ether. This ether extract was washed with an aqueous solution of Na<sub>2</sub>S<sub>2</sub>O<sub>3</sub>, dried over Na<sub>2</sub>SO<sub>4</sub>, filtered, and evaporated. the residue was sublimed under reduced pressure and recrystallized from MeCN giving 4-bromo-2,3-naphthalenedicarboxylic anhydride **2**. Yield: 719 mg (26%). Colorless solid, M.p. 213–215°C. <sup>1</sup>H NMR (400 MHz, CDCl<sub>3</sub>), δ<sub>H</sub> 9.01 (s, 1H), 8.55 (s, 1H), 8.09–8.13 (m, 2H), 7.66 (dd, *J* = 8.2, 0.6 Hz, 1H), <sup>13</sup>C NMR (100 MHz, CDCl<sub>3</sub>), δ<sub>C</sub> 162.72, 162.61, 137.63, 135.23, 134.65, 130.89, 130.41, 128.28, 127.77, 127.25, 126.82, 125.48. HRMS (FAB, *m/z*, MH<sup>+</sup>) Calcd. for C<sub>12</sub>H<sub>6</sub>BrO<sub>3</sub>: 276.9500. Found: 276.9503.

***N*-butyl-4-bromonaphthalene-2,3-dicarboximide (3a), *N*-octyl-4bromonaphthalene-2,3-dicarboximide (3b), and *N*-dodecyl-4bromonap-hthalene-2,3-dicarboximide (3c):** To a stirred mixture of 4-bromo-2,3-naphthalenedicarboxylic anhydride **2** (0.27 mmol) in acetic acid (2 mL) was added appropriate primary amine (0.5 mmol), then the mixture was refluxed for 17 h. The reaction mixture was cooled to room temperature and then poured onto ice water (100 mL). This mixture was extracted with AcOEt (100 mL), washed with aqueous NaHCO<sub>3</sub> solution, dried over MgSO<sub>4</sub>, and concentrated. The residue was chromatographed on silica gel (AcOEt) and recrystallized (chloroform: hexane) to afford bromonaphthal imides **3**.

**3a:** yield 87%. Colorless needles, M.p. 123–124°C. <sup>1</sup>H NMR (400 MHz, CDCl<sub>3</sub>), δ<sub>H</sub> 8.77 (s, 1H), 8.31 (s, 1H), 8.01(d, *J* = 8.3, 1H), 7.98 (dd, *J* = 7.6, 1.0, 1H), 7.53 (t, *J* = 7.8, 1H), 3.77(t, *J* = 7.3, 2H), 1.67–1.75 (m, 2H), 1.40 (sext, *J* = 7.3, 2H), 0.97 (t, *J* = 7.3, 3H). <sup>13</sup>C NMR (100 MHz, CDCl<sub>3</sub>), δ<sub>C</sub> 167.89, 167.82, 137.02, 134.51, 133.30, 130.15, 129.49, 129.30, 128.80, 125.26, 124.87, 124.26, 38.36, 30.69, 20.28, 13.81. IR (neat) ν<sub>max</sub> 1696, 1400 cm<sup>-1</sup>. Anal. Calcd. for C<sub>16</sub>H<sub>14</sub>BrNO<sub>2</sub>: C, 57.85; H, 4.25; N, 4.22. Found: C, 57.95; H, 4.08; N, 4.13.

**3b**: yield 84%. Colorless needles, M.p. 107–108°C. <sup>1</sup>H NMR (400 MHz, CDCl<sub>3</sub>) δ<sub>H</sub> 8.77 (s, 1H), 8.31 (s, 1H), 8.01 (d, *J* = 8.3 Hz, 1H), 7.98 (dd, *J* = 7.5, 1.0 Hz, 1H), 7.53 (dd, *J* = 7.6, 0.5 Hz, 1H), 3.76 (t, *J* = 7.3 Hz, 2H), 1.71 (quin, *J* = 7.4 Hz, 2H), 1.41–1.18 (m, 10H), 0.87 (t, *J* = 6.9 Hz, 3H). <sup>13</sup>C NMR (100 MHz, CDCl<sub>3</sub>) δ<sub>C</sub> 167.89, 167.81, 137.00, 134.49, 133.29, 130.15, 129.49, 129.28, 128.78, 125.25, 124.88, 124.26, 38.62, 31.91, 29.21, 28.66, 27.05, 22.77, 14.23. IR (neat) ν<sub>max</sub> 2920, 1693, 1400 cm<sup>-1</sup>. Anal. Calcd. for C<sub>20</sub>H<sub>22</sub>BrNO<sub>2</sub>: C, 61.86; H, 5.71; N, 3.61. Found: C, 61.86; H, 5.65; N, 3.56.

**3c**: yield 89%. Colorless needles, M.p. 104–105°C. <sup>1</sup>H NMR (400 MHz, CDCl<sub>3</sub>) δ<sub>H</sub> 8.78 (s, 1H), 8.31 (s, 1H), 8.01 (d, *J* = 8.3 Hz, 1H), 7.98 (dd, *J* = 7.5, 1.0 Hz, 1H), 7.53 (t, *J* = 7.8 Hz, 1H), 3.76 (t, *J* = 7.3 Hz, 2H), 1.71 (quin, *J* = 7.4 Hz, 2H), 1.41–1.18 (m, 18H), 0.87 (t, *J* = 6.9 Hz, 3H). <sup>13</sup>C NMR (100 MHz, CDCl<sub>3</sub>) δ<sub>C</sub> 167.91, 167.84, 137.02, 134.51, 133.30, 130.16, 129.51, 129.30, 128.79, 125.27, 124.89, 124.28, 38.64, 32.05, 29.77, 29.76, 29.71, 29.64, 29.49, 29.36, 28.66, 27.06, 22.83, 14.28. IR (neat) ν<sub>max</sub> 2920, 1693(C=O), 1400(C-N) cm<sup>-1</sup>. Anal. Calcd. for C<sub>24</sub>H<sub>30</sub>BrNO<sub>2</sub>: C, 64.86; H, 6.80; N, 3.15. Found: C, 64.85; H, 6.79; N, 3.10.

**(*E*)-1,2-bis(2-butyl-1,3-dihydro-1,3-dioxobenzo[*f*]-2H-isoindol-5-yl)-ethene 4a, (*E*)-1,2-bis(2-octyl-1,3-dihydro-1,3-dioxobenzo[*f*]-2H-isoindol-5-yl) ethene 4b, and (*E*)-1,2-bis(2-dodecyl-1,3-dihydro-1,3-dioxobenzo[*f*]-7-2H-isoindol-5-yl) ethene 4c**: A solution of *N*-butyl-4-bromonaphthalene-2,3-dicarboximide **3** (1.44 mmol) and (*E*)-1, 2-bis(tributylstannyl)ethene (0.7 mmol) in 15 ml dry toluene was evacuated and refilled with argon three times. Tetrakis(triphenylphosphine)-palladium(0) (3 mol %) was added to the mixture. The mixture was further purged with argon and refluxed overnight. The resulting mixture was concentrated and the residue was chromatographed on silica gel using a mixture of hexane: EtOAc = 5:1 as an eluent. Recrystallization of the crude product from MeOH/CHCl<sub>3</sub> to afford compound **4**.

**4a**: yield 84%. Yellow solid. M.p. >300°C. <sup>1</sup>H NMR (600 MHz, CDCl<sub>3</sub>): δ<sub>H</sub> 8.73 (s, 2H), 8.39 (s, 2H), 8.09 (dd, *J* = 11.3, 7.9 Hz, 4H), 8.00 (s, 2H), 7.79 (dd, *J* = 8.2, 7.2

Hz, 2H), 3.77 (t,  $J = 7.3$  Hz, 4H), 1.75 – 1.67 (m, 4H), 1.40 (m,  $J = 7.3$  Hz, 4H), 0.96 (t,  $J = 7.4$  Hz, 6H).  $^{13}\text{C}$  NMR (151 MHz,  $\text{CDCl}_3$ ):  $\delta_{\text{C}}$  168.2, 167.9, 137.1, 135.8, 133.3, 130.7, 129.4, 129.0, 128.1, 127.8, 127.2, 125.1, 120.3, 38.1, 30.5, 20.1, 13.6. IR (neat)  $\nu_{\text{max}}$  2378, 1703 (C=C), 1489, 1338, 1057  $\text{cm}^{-1}$ . Anal. Calcd. for  $\text{C}_{34}\text{H}_{30}\text{N}_2\text{O}_4$ : C, 76.96; H, 5.70; N, 5.28%. Found: C, 76.75; H, 5.33; N, 5.20%.

**4b**: yield 79%. Yellow solid, M.p. 260–261°C.  $^1\text{H}$  NMR (600 MHz,  $\text{CDCl}_3$ )  $\delta_{\text{H}}$  8.72 (s, 1H), 8.39 (s, 1H), 8.10 (d,  $J = 6.2$  Hz, 1H), 8.08 (d,  $J = 6.9$  Hz, 1H), 8.00 (s, 1H), 7.79 (dd,  $J = 7.33, 0.8$  Hz, 1H), 3.75 (t,  $J = 7.3$  Hz, 2H), 1.71 (quin,  $J = 7.5, 7.0$  Hz, 2H), 1.42–1.19 (m, 10H), 0.86 (t,  $J = 6.7$  Hz, 3H).  $^{13}\text{C}$  NMR (151 MHz,  $\text{CDCl}_3$ )  $\delta_{\text{C}}$  168.41, 168.16, 137.28, 136.06, 133.54, 130.89, 129.59, 129.17, 128.32, 128.07, 127.37, 125.38, 120.53, 38.57, 31.91, 29.32, 28.71, 27.07, 22.77, 14.23, 27.07, 22.77, 14.23. IR (neat)  $\nu_{\text{max}}$  2927, 1764, 1707, 1384  $\text{cm}^{-1}$ . Anal. Calcd. for  $\text{C}_{42}\text{H}_{46}\text{N}_2\text{O}_4$ : C, 78.47; H, 7.21; N, 4.36. Found: C, 78.62; H, 7.15; N, 4.37.

**4c**: yield 88%. Yellow crystals, M.p. 237–239°C.  $^1\text{H}$  NMR (600 MHz,  $\text{CDCl}_3$ )  $\delta_{\text{H}}$  8.72 (s, 1H), 8.38 (s, 1H), 8.09 (d,  $J = 7.4$  Hz, 1H), 8.07 (d,  $J = 8.1$  Hz, 1H), 7.99 (s, 1H), 7.79 (t,  $J = 7.7$  Hz, 1H), 3.75 (t,  $J = 7.4$  Hz, 2H), 1.71 (quin,  $J = 7.3$  Hz, 2H), 1.39–1.18 (m, 18H), 0.86 (t,  $J = 7.0$  Hz, 3H).  $^{13}\text{C}$  NMR (151 MHz,  $\text{CDCl}_3$ )  $\delta_{\text{C}}$  168.40, 168.16, 137.29, 136.07, 133.56, 130.89, 129.60, 129.17, 128.34, 128.09, 127.37, 125.37, 120.52, 38.58, 32.05, 29.77, 29.76, 29.71, 29.65, 29.48, 29.37, 28.71, 27.08, 22.82, 14.26. IR (neat)  $\nu_{\text{max}}$  2921, 1766, 1710 (C=O), 1384 (C-N)  $\text{cm}^{-1}$ . Anal. Calcd. for  $\text{C}_{50}\text{H}_{62}\text{N}_2\text{O}_4$ : C, 79.54; H, 8.28; N, 3.71. Found: C, 79.55; H, 8.33; N, 3.77.

***N*-Dibutyl-picene-2,3,10,11-tetracarboxydiimide C<sub>4</sub>-PicDI, *N*-Dioctyl-picene-2,3,10,11-tetracarboxydiimide C<sub>8</sub>-PicDI, and *N*-Didodecyl-picene-2,3,10,11-tetracarboxydiimide C<sub>12</sub>-PicDI**: A solution of compound **4** (0.4 mmol) and iodine (10 mol%) in 400 mL  $\text{CH}_2\text{Cl}_2$  was purged with air. The solution was irradiated with 352nm UV lamp (6×15W). The reaction was stopped when TLC analysis revealed the reaction had proceeded to completion. The solvent was removed under reduced pressure and the residue was extracted with  $\text{CH}_2\text{Cl}_2$ . The solution was washed with saturated aqueous  $\text{Na}_2\text{S}_2\text{O}_3$  solution 3 times. The organic ph-

ase was dried over  $\text{MgSO}_4$  and concentrated to obtain crude product **C<sub>n</sub>-PicDI**. Then the solid was recrystallized from chlorobenzene to afford **C<sub>n</sub>-PicDI** pale yellow solid.

**C<sub>4</sub>-PicDI**: yield 60%. Pale yellow solid, M.p.  $>300^\circ\text{C}$ .  $^1\text{H}$  NMR (600 MHz,  $\text{CDCl}_3$ )  $\delta_{\text{H}}$  9.32 (s, 2H), 9.07 (s, 2H), 8.98 (d,  $J = 9.2$  Hz, 2H), 8.48 (s, 2H), 8.25 (d,  $J = 9.1$  Hz, 2H), 3.82 (t,  $J = 7.4$  Hz, 4H), 1.80 – 1.72 (m, 4H), 1.45 (sext,  $J = 7.4$  Hz, 4H), 1.00 (t,  $J = 7.4$  Hz, 6H).  $^{13}\text{C}$  NMR (151 MHz,  $50^\circ\text{C}$ )  $\delta_{\text{C}}$  168.44, 168.16, 135.38, 133.72, 130.48, 130.20, 129.68, 129.59, 129.06, 124.83, 124.58, 123.37, 119.62, 38.436, 30.852, 20.354, 13.77. IR (neat)  $\nu_{\text{max}}$  2912, 1736 (C=C), 1261, 1120,  $781\text{cm}^{-1}$ . Anal. Calcd. for  $\text{C}_{34}\text{H}_{28}\text{N}_2\text{O}_4$ : C, 77.25; H, 5.34; N, 5.16%. Found: C, 77.55; H, 5.06; N, 5.16%.

**C<sub>8</sub>-PicDI**: yield 54%. Pale yellow solid, M.p.  $>300^\circ\text{C}$ .  $^1\text{H}$  NMR (600 MHz,  $\text{CDCl}_3$ )  $\delta_{\text{H}}$  9.01 (s, 1H), 8.88 (d,  $J = 9.4$  Hz, 1H), 8.80 (s, 1H), 8.35 (s, 1H), 8.16 (d,  $J = 9.0$  Hz, 1H), 3.77 (t,  $J = 7.5$  Hz, 2H), 1.76 (quin,  $J = 7.5, 7.3$  Hz, 2H), 1.44–1.22 (m, 10H), 0.88 (t,  $J = 7.0$  Hz, 3H).  $^{13}\text{C}$  NMR (151 MHz,  $\text{CDCl}_3$ )  $\delta_{\text{C}}$  168.33, 167.99, 135.01, 133.25, 129.99, 129.78, 129.27, 129.18, 128.90, 124.64, 124.33, 122.95, 119.29, 38.61, 31.95, 29.36, 28.78, 27.13, 22.80, 14.25, 28.78, 27.13, 22.80, 14.25. IR (neat)  $\nu_{\text{max}}$  2923, 1763, 1711,  $1388\text{ cm}^{-1}$ . HRMS (FAB,  $m/z$ ,  $\text{M}^+$ ) Calcd. for  $\text{C}_{42}\text{H}_{44}\text{N}_2\text{O}_4$ : 640.3301. Found: 640.3277.

**C<sub>12</sub>-PicDI**: yield 82%. Pale yellow solid, M.p.  $> 300^\circ\text{C}$ .  $^1\text{H}$  NMR (600 MHz,  $\text{CDCl}_3$ )  $\delta_{\text{H}}$  9.11 (s, 1H), 8.89 (d,  $J = 9.4$  Hz, 1H), 8.83 (s, 1H), 8.37 (s, 1H), 8.18 (d,  $J = 9.0$  Hz, 1H), 3.77 (t,  $J = 7.4$  Hz, 2H), 1.75 (quin,  $J = 7.4, 7.3$  Hz, 2H), 1.43–1.18 (m, 18H), 0.86 (t,  $J = 7.0$  Hz, 3H).  $^{13}\text{C}$  NMR (151 MHz,  $\text{CDCl}_3$ )  $\delta_{\text{C}}$  168.36, 168.03, 135.02, 133.26, 130.00, 129.80, 129.25, 129.17, 128.91, 124.66, 124.36, 122.98, 119.33, 38.61, 32.06, 29.80, 29.78, 29.75, 29.70, 29.51, 29.40, 28.78, 27.13, 22.84, 14.29. IR (neat)  $\nu_{\text{max}}$  2916, 1765, 1698,  $1391\text{ cm}^{-1}$ . Anal. Calcd. for  $\text{C}_{50}\text{H}_{60}\text{N}_2\text{O}_4$ : C, 79.75; H, 8.03; N, 3.72. Found: C, 79.64; H, 8.03; N, 3.74.

## 2.5 References

1. Y. Guo, K. Yoshioka, S. Hamao, Y. Kubozono, F. Tani, K. Goto and H. Okamoto, *RSC Adv.*, 2020, **10**, 31547-31552.
2. P. M. Beaujuge and J. M. Frechet, *J. Am. Chem. Soc.*, 2011, **133**, 20009-20029.
3. Y. Shi, H. Guo, M. Qin, J. Zhao, Y. Wang, H. Wang, Y. Wang, A. Facchetti, X. Lu and X. Guo, *Adv. Mater.*, 2018, **30**.
4. A. Onwubiko, W. Yue, C. Jellett, M. Xiao, H. Y. Chen, M. K. Ravva, D. A. Hanifi, A. C. Knall, B. Purushothaman, M. Nikolka, J. C. Flores, A. Salleo, J. L. Bredas, H. Sirringhaus, P. Hayoz and I. McCulloch, *Nat. Commun.*, 2018, **9**, 416.
5. Y. Wang, T. Hasegawa, H. Matsumoto and T. Michinobu, *J. Am. Chem. Soc.*, 2019, **141**, 3566-3575.
6. J. A. Rogers, Z. Bao, K. Baldwin, A. Dodabalapur, B. Crone, V. R. Raju, V. Kuck, H. Katz, K. Amundson, J. Ewing and P. Drzaic, *Proc. Natl. Acad. Sci.*, 2001, **98**, 4835-4840.
7. G. Gelinck, P. Heremans, K. Nomoto and T. D. Anthopoulos, *Adv. Mater.*, 2010, **22**, 3778-3798.
8. P. F. Baude, D. A. Ender, M. A. Haase, T. W. Kelley, D. V. Muyres and S. D. Theiss, *Appl. Phys. Lett.*, 2003, **82**, 3964-3966.
9. Z. Liu, G. Zhang, Z. Cai, X. Chen, H. Luo, Y. Li, J. Wang and D. Zhang, *Adv. Mater.*, 2014, **26**, 6965-6977.
10. X. Zhan, A. Facchetti, S. Barlow, T. J. Marks, M. A. Ratner, M. R. Wasielewski and S. R. Marder, *Adv. Mater.*, 2011, **23**, 268-284.
11. F. B. Mallory, K. E. Butler, A. C. Evans and C. W. Mallory, *Tetrahedron Lett.*, 1996, **37**, 7173-7176.
12. H. Okamoto, N. Kawasaki, Y. Kaji, Y. Kubozono, A. Fujiwara and M. Yamaji,

- J. Am. Chem. Soc.*, 2008, **130**, 10470-10471.
13. H. Okamoto, S. Hamao, H. Goto, Y. Sakai, M. Izumi, S. Gohda, Y. Kubozono and R. Eguchi, *Sci. Rep.*, 2014, **4**, 5048.
  14. J. E. Anthony, *Angew. Chem. Int. Edit.*, 2008, **47**, 452-483.
  15. O. Ostroverkhova, *Chem. Rev.*, 2016, **116**, 13279-13412.
  16. B. A. Jones, A. Facchetti, M. R. Wasielewski and T. J. Marks, *J. Am. Chem. Soc.*, 2007, **129**, 15259-15278.
  17. H. Usta, C. Risko, Z. Wang, H. Huang, M. K. Deliomeroğlu, A. Zhukhovitskiy, A. Facchetti and T. J. Marks, *J. Am. Chem. Soc.*, 2009, **131**, 5586-5608.
  18. T. S. Moreira, M. Ferreira, A. Dall'armellina, R. Cristiano, H. Gallardo, E. A. Hillard, H. Bock and F. Durola, *Eur. J. Org. Chem.*, 2017, **2017**, 4548-4551.
  19. G. Naulet, S. Huet-Exiga, H. Bock and F. Durola, *Org. Chem. Front.*, 2019, **6**, 994-997.
  20. M. Bendikov, F. Wudl and D. F. Perepichka, *Chem. Rev.*, 2004, **104**, 4891-4946.
  21. T. B. Singh, S. Erten, S. Günes, C. Zafer, G. Turkmen, B. Kuban, Y. Teoman, N. S. Sariciftci and S. Icli, *Org. Electron.*, 2006, **7**, 480-489.
  22. S. P. Adiga and D. Shukla, *J. Phys. Chem. C*, 2010, **114**, 2751-2755.
  23. N. Hiroshiba, R. Hayakawa, T. Chikyow, Y. Yamashita, H. Yoshikawa, K. Kobayashi, K. Morimoto, K. Matsuishi and Y. Wakayama, *Phys. Chem. Chem. Phys.*, 2011, **13**, 6280-6285.
  24. R. Wang, K. Shi, K. Cai, Y. Guo, X. Yang, J.-Y. Wang, J. Pei and D. Zhao, *New J. Chem.*, 2016, **40**, 113-121.
  25. T. S. Moreira, M. Ferreira, A. Dall'Armellina, R. Cristiano, H. Gallardo, E. A. Hillard, H. Bock and F. Durola, *Eur. J. Org. Chem.*, 2017, **30**, 4548-4551.
  26. K. J. Baeg, M. Caironi and Y. Y. Noh, *Adv. Mater.*, 2013, **25**, 4210-4244.
  27. A. Y. Amin, A. Khassanov, K. Reuter, T. Meyer-Friedrichsen and M. Halik, *J. Am. Chem. Soc.*, 2012, **134**, 16548-16550.
  28. T. Okamoto, C. P. Yu, C. Mitsui, M. Yamagishi, H. Ishii and J. Takeya, *J. Am. Chem. Soc.*, 2020, **142**, 9083-9096.



29. H. Mori, X. C. Chen, N. H. Chang, S. Hamao, Y. Kubozono, K. Nakajima and Y. Nishihara, *J. Org. Chem.*, 2014, **79**, 4973-4983.



## **Chapter 3**

### 3.1 Introduction

Organic electronics is recognized as a promising novel technology with irrepressible advantages, such as low cost, lightweight, designability, and easy processability, and mechanical flexibility. Great strides have been made over the past decade toward the development of efficient ambipolar molecules, which play a crucial role in constructing OFET for logic gates.<sup>1</sup> The research in this field is focused on the designing of new organic  $\pi$ -conjugated molecules,<sup>2,3</sup> and innovative methodologies to enhance the device performance.<sup>4</sup> Up to now, diverse materials are synthesized and utilized for implementing and their further emerging applications requirements.<sup>5,6</sup>

The development of high-performance FETs is in need, since it is a key component of integrated circuits. Therefore, more practical applications and improvements can be achieved by devoting the research on p-type devices, n-type and ambipolar semiconducting materials with high performance are, thus, desired. Currently, development of such materials is still a critical challenge in organic electronics.

A promising alternative approach is to use ambipolar OFET devices, in which both electrons and holes can be injected and transported in the same ambipolar organic semiconducting layer, have improved significantly.<sup>4</sup> To realize ambipolar devices, balanced n- and p- type conduction characteristics are desired as the basic and important criteria for achieving good performance electronic devices.<sup>7</sup>

For OFETs that can offer both n- and p- type behavior, the molecules must have suitable for both hole and electron transport. One of the main challenges hampering electronic properties the development of new high-performance ambipolar molecules have been the design and synthesis of new frameworks with charge carrier mobilities.<sup>8</sup> Hence, to meet these requirements, fine tuning of the HOMO and LUMO energy levels are the key factors for obtaining ambipolar OSCs. For designing OSC molecules, it is generally considered that the molecules are required to have a HOMO energy level  $\leq -5.0$  eV to achieve stable hole transport and the LUMO energy level

needs to be  $\leq -4.0$  eV for the stable electron transport.<sup>5,9</sup>

In recent years, ambipolar OFETs were generally fabricated by polymers, charge carrier transporting along the polymer backbones have attracted a great deal of research interest. Donor-acceptor polymers with diketopyrrolopyrrole (**DPP**) as a benchmark acceptor in OFETs have been realized owing to planar backbone, good  $\pi$ -conjugation, and strong intermolecular interactions.<sup>10</sup> Chen and coworkers developed an strategy by a bisdiketopyrrolopyrrole (**2DPP**) for an ambipolar organic semiconductor. The FETs based on **P2DPP-BTz** (see Fig. 3-1 for molecular structure) show high performance with hole and electron mobilities of 1.73 and 2.58  $\text{cm}^2 \text{V}^{-1} \text{s}^{-1}$ , respectively. These results demonstrate that the **2DPP** acceptor is a promising building block for high-mobility ambipolar polymers.<sup>11</sup>

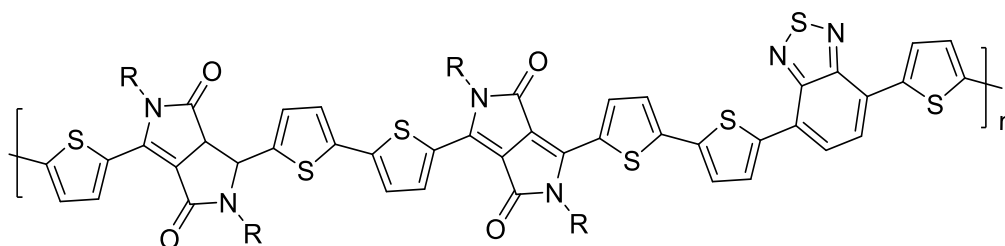


**Fig. 3-1.** Structure of **P2DPP-BTz**.

Small molecular type semiconductors have been emerged as competitive alternatives to conjugated polymers due to the diverse merits of good reproducibility with monodisperse molecular weight, well-defined molecular structure, ease of purification, and easier functionalization.<sup>12,13</sup> Small molecules can provide a better-ordered film than provided by polymers, which can improve the charge-carrier transport properties of the OFET device.<sup>14,15</sup>

In particular, small molecules with A-D-A type or D-A-D type conjugated frameworks often exhibit relatively high OFET performance. A series of  $\pi$ -extended quinolines with D- $\pi$ -A-D and D- $\pi$ -A-A architectures were employed to such molecules illustrated in Fig. 3-2. **PPQC**<sup>16</sup> (R = OMe) serves as ambipolar organic semiconductors. Ambipolar mobilities were observed for methoxy group substituted

compounds. Among the molecules studied, the good charge carrier mobilities are supported by the electron-donating methoxy group to appropriately adjust the HOMO and LUMO energy levels and to arrange the molecules into solid state through better self-assembly.

Ramachandran and coworkers have reported using triaryl amines (TAAs) as the parent core, ester groups were introduced into the periphery of the aryl substituents to adequately alter the molecular packing in the solid phase and electronic energy levels.<sup>17</sup> The asymmetrical compound **DEPA** exhibited hole mobility of  $0.003 \text{ cm}^2 \text{ V}^{-1} \text{ s}^{-1}$  with on/off ratio of  $10^5$ .

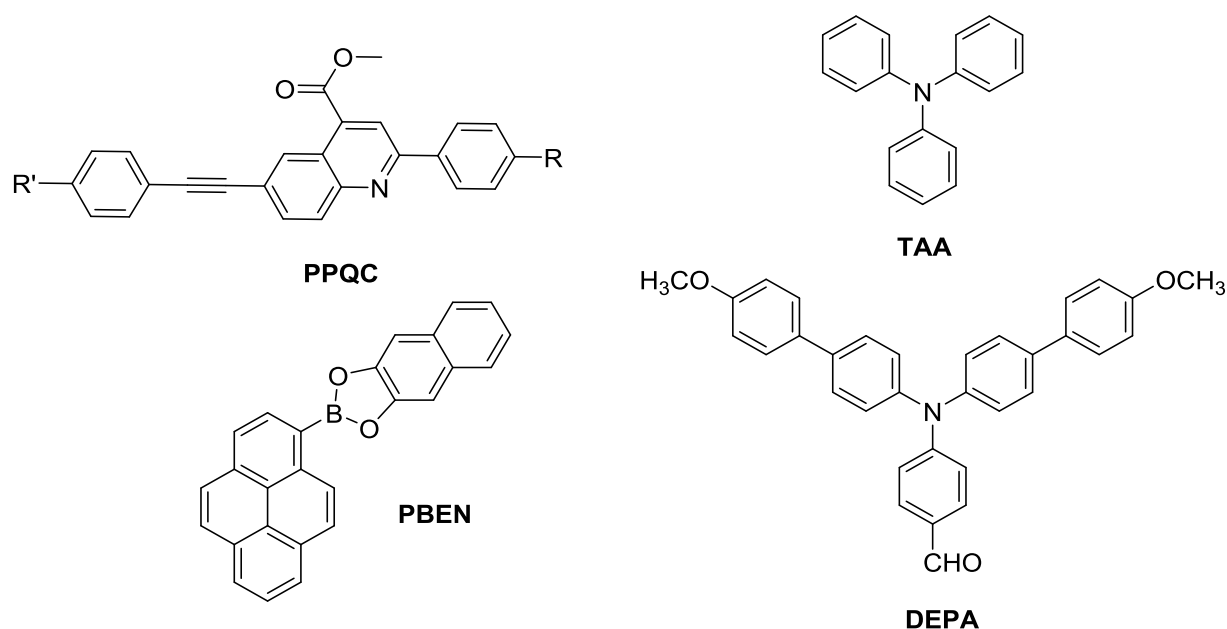


**Fig. 3-2.** Structure of **PPQC**, **DEPA** and **PBEN**.

In 2008, Yamashita and the coworkers first reported  $\pi$ -conjugated system, **PBEN**, containing tricoordinated boron atoms which was effective to increase intermolecular donor-accepter interactions. The devices using **PBEN** showed hole mobility as high as  $2.4 \times 10^{-7} \text{ cm}^2 \text{ V}^{-1} \text{ s}^{-1}$  and on/off ratio of 20.<sup>18</sup>

A series of dithienosilole-based molecules were synthesized by introducing terminal ester groups with different alkyl side chain. The structural modifications yielded significant changes in the electronic properties as well as on their performance in

OFET and OPV performance.<sup>19</sup> **C8-Ester** (see Fig. 3-3 for molecular structure) exhibited high hole mobilities up to  $1.37 \times 10^{-2} \text{ cm}^2 \text{ V}^{-1} \text{ s}^{-1}$  due to well-ordered, edge-on molecular orientations for these molecules. It demonstrates that the intermolecular interactions of small molecule donors can be selectively tuned by rational molecular design for optimizing the performance in OFETs.

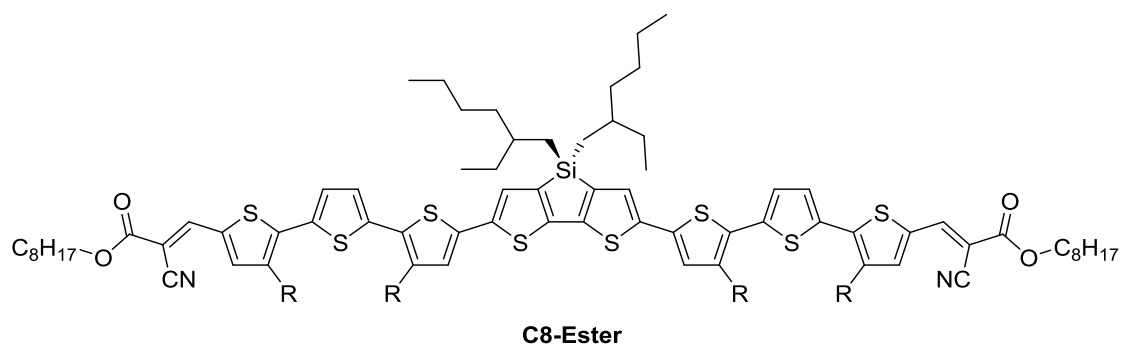


**Fig. 3-3.** Structure of **C8-Ester**.

Pentacene and picene are the structural isomers (see Fig. 2-1 for molecular structure), which are well-known benchmark p-type molecules with molecular structures of one-dimensional graphene nanoribbons. These isomers exhibit contrasting optical and electronic properties to each other due to the different benzene ring arrangements. Picene possesses a zigzag arrangement of the benzene rings to have a graphene armchair-edge structure, that provides an electronically stable nature of the picene molecule.<sup>20,21</sup> It was reported that picene derivatives incorporating long alkyl chains along the long axis of the molecule served as active layers of FET displaying hole mobility as high as  $21 \text{ cm}^2 \text{ V}^{-1} \text{ s}^{-1}$ .<sup>22</sup> Given the fact that the mobility for the unsubstituted picene is much lower than that of the alkylated one. It is expected that the introduction of peripheral substituents into picene-type  $\pi$ -systems leads to conspicuous improvements in processability, environmental stability and the electrical performance of organic semiconductors.

Herein, the present author reports the synthesis of new ester-substituted-picene analogues **7** and **10**, and their FET properties. Compound **10** and compound **7** are introduced with two or four ester groups along the long axis of the picene framework to modify their

electronic characteristics as well as to facilitate solution processability. The ester substitution would be of significant interest as it may systematically modulate the optoelectronic properties such as the HOMO and LUMO energy levels, thus, the bandgap.

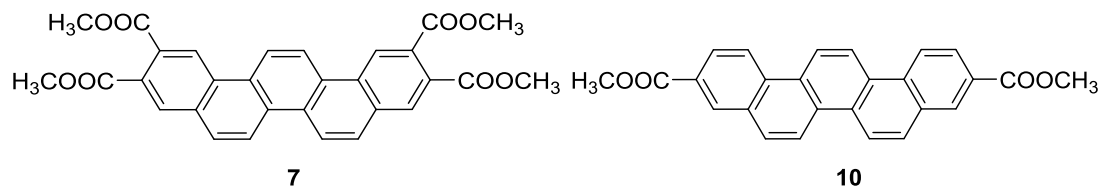


**Fig. 3-4.** Structure of compounds 7 and 10.

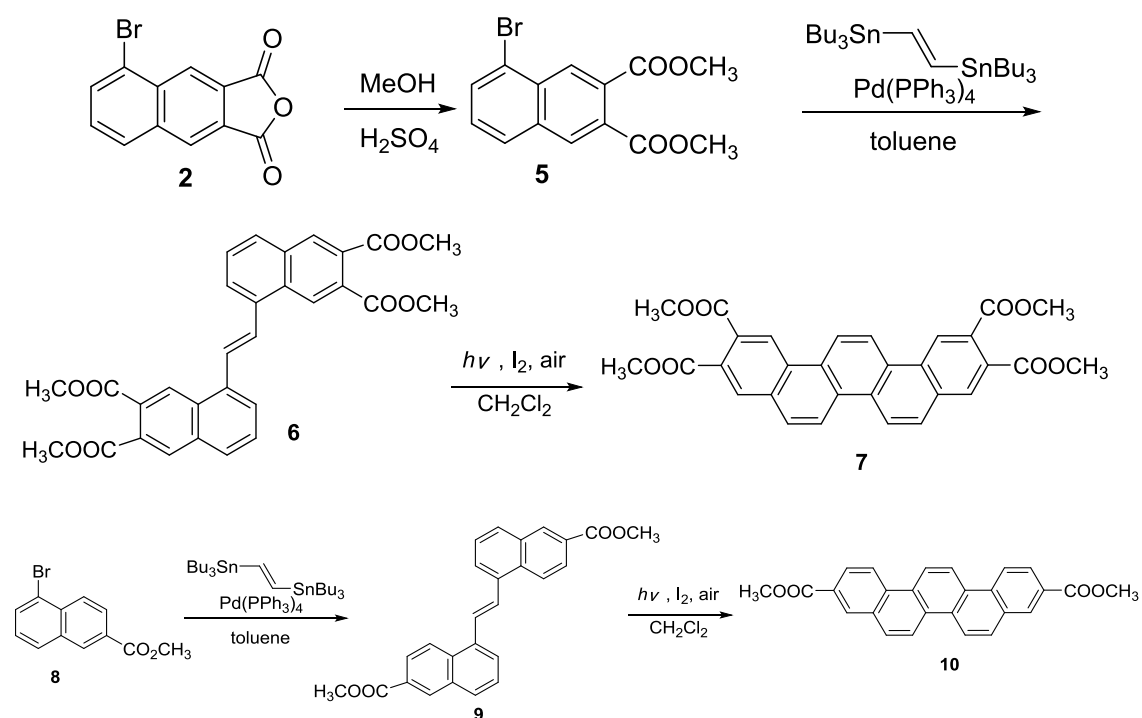


## 3.2 Results and Discussions

### 3.2.1 Synthesis of ester-substituted picene

The synthetic routes toward ester substituted picenes **7** and **10** were outlined in Scheme 3-1. The detailed synthetic procedures of precursors and final molecules are given in the experimental section. All compounds were obtained characterized by  $^1\text{H}$  NMR,  $^{13}\text{C}$  NMR and IR spectroscopy, as well as elemental analysis.

Bromonaphthalene dicarboxylic ester **5** was prepared by standard esterification of 5-bromo-2,3-naphthalenedicarboxylic anhydride **2** with methanol in the presence of  $\text{H}_2\text{SO}_4$ . Two kinds of 5-bromonaphthalene derivatives with ester appended side chains, **5** and **8**, were chosen as the constituent building blocks for the functionalized picenes. A Migita-Kosugi-Stille cross coupling reactions of bromonaphthalenes **5** and **8** with (*E*)-1,2-bis(tributylstannyl)ethene proceeded smoothly with catalytic amount of  $\text{Pd}(\text{PPh}_3)_4$  to yield the key diarylethenes **6** and **9**, respectively. As for the synthesis of the target products, functionalized diarylethenes **6** and **9** were ideal precursors, which was readily underwent the Mallory photoreaction when they were irradiated with black-light lamps (352 nm, 6  $\times$  15W) in the presence of 10 mol% iodine.



**Scheme 3-1.** Synthetic routes to ester-incorporating picenes **7** and **10**.

The structural assignments of compound **7** and **10** are described as follows. Fig. 3-5 shows the  $^1\text{H}$  NMR spectra (aromatic region) of the two compounds and the parent picene as the reference. The  $^1\text{H}$  NMR signals were clearly assigned by comparing those protons of picene. The triplet signal of  $\text{H}_g$  in picene disappeared in the  $^1\text{H}$  NMR spectrum of compound **10** (Fig. 3-5 (b)). The signals of  $\text{H}_{c'}$  and  $\text{H}_f$  respectively appeared at 8.75 ppm and 8.35 ppm with significant down-field shifted. The other protons have slightly down-field shift compared to those of the parent picene. The aromatic protons of compound **7** were observed in the region of 8.0-9.2 ppm as shown in Fig. 3-5 (c). Upon introduction of the former groups, the triplet signals observed for picene ( $\text{H}_g$  and  $\text{H}_f$ ) disappeared in the  $^1\text{H}$  NMR spectrum of compound **7**. The signals of  $\text{H}_{c''}$  and  $\text{H}_{e''}$  of compound **10** respectively appeared as a singlet at 9.01 ppm and 8.41 ppm. These observations provide evidence for the presence of the ester substituents at the edges of the molecules. The signals for  $\text{H}_{d''}$  as a singlet at 9.24 ppm, and  $\text{H}_{a''}$ , as a doublet at 8.91 ppm, were assigned because they located in the bay region, where the protons affected by more significant anisotropic effects compared to these at the edges of the molecule. The  $^{13}\text{C}$  NMR spectra of picene and **10** were not

measured due to their poor solubility, the  $^{13}\text{C}$  NMR spectra of **7** which having four ester groups was obtained successfully. These results indicate the ester group enhance the phenacene solubility in common solvent.

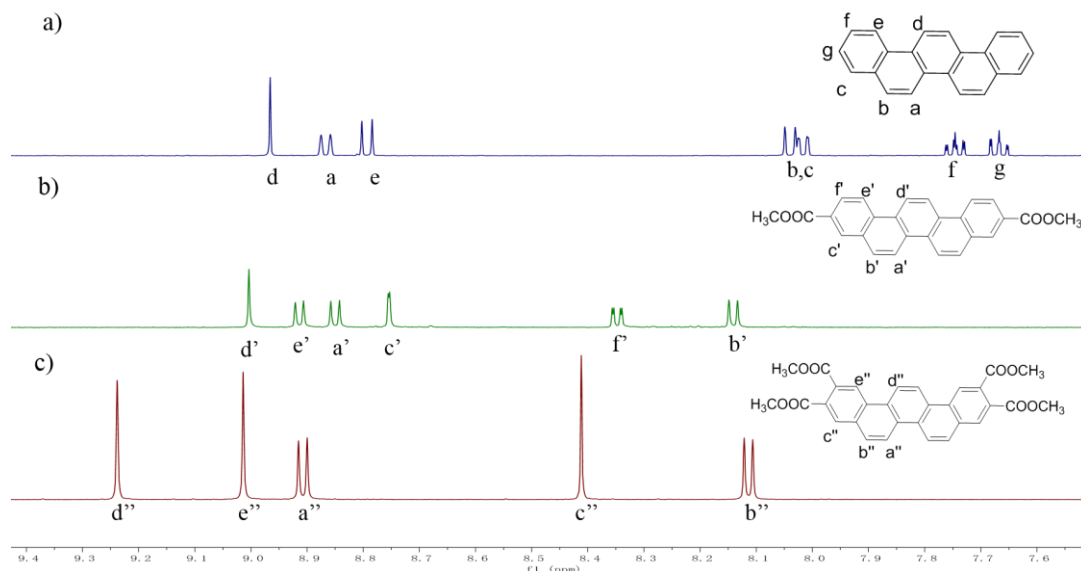


**Fig. 3-5.**  $^1\text{H}$  NMR spectra (600 MHz) of picene (a), **10** (b) and **7** (c) in  $\text{CDCl}_3$ .

### 3.2.2 Electronic spectra in solution and crystalline states

To understand the electronic properties of the ester derivatives **7** and **10**, UV-vis absorption and fluorescence spectra were recorded in CHCl<sub>3</sub> at room temperature. The photophysical parameters, such as maximum absorption wavelengths ( $\lambda_{\text{max}}^{\text{Abs}}$ ) and molar absorption coefficients ( $\epsilon$ ), are summarized in Table 3-1.

In the absorption spectra of compounds **7** and **10** (Fig. 3-6), a sharp band in the range of 275-286 nm and some moderate intensity bands are in the region of 300-350 nm, and weak bands at 358 nm and 378 nm were observed. In comparison to the parent picene, the absorption profiles of new compound **10** showed a similar one expects for that compound **10** exhibited a redshift by 20 nm. The bathochromic shift was caused by the ester groups introduced along the long axis of the molecule. The lower energy bands in the wavelength region from 350 to 400 nm were observed much more clearly than those of picene. Compound **7**, which has four ester groups, showed a maximum at 298 nm along with a shoulder peak at 338 nm, broad tails with a relatively low intensity in the low energy region (350-400 nm). In contrast to picene, compound **7** shows a bathochromic shift with the peak of the low energy absorption in the region of 350-400 nm, which is same for compound **10**. These results suggest that the strong electron-withdrawing nature of methoxy groups directly affects the electronic structures of the picene core.

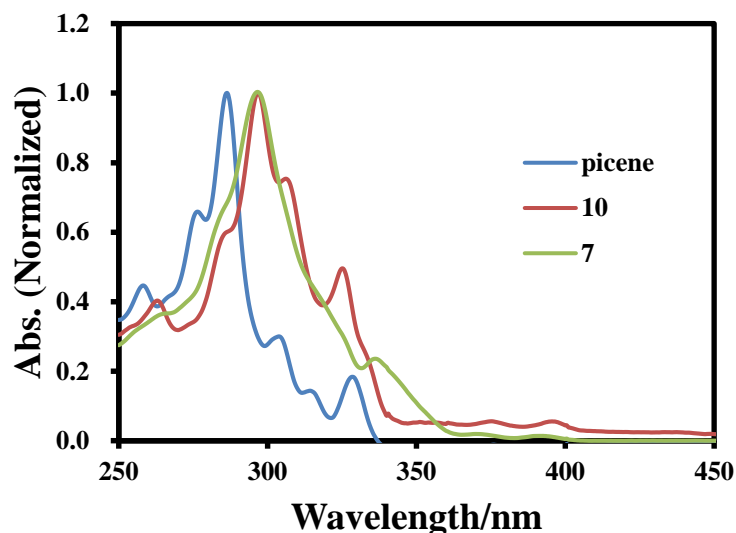


Fig. 3-6. Electronic absorption spectra of **7**, **10** and parent picene in  $\text{CHCl}_3$ .

The fluorescence spectra of compounds **7** and **10** have nearly identical profiles exhibiting a vibronic structure similar to those the of parent picene as shown in Fig. 3-6. The emission maxima were bathochromically shifted compared to that of the parent picene by 26 nm indicating that the substitution position and number little affected the fluorescence spectra.

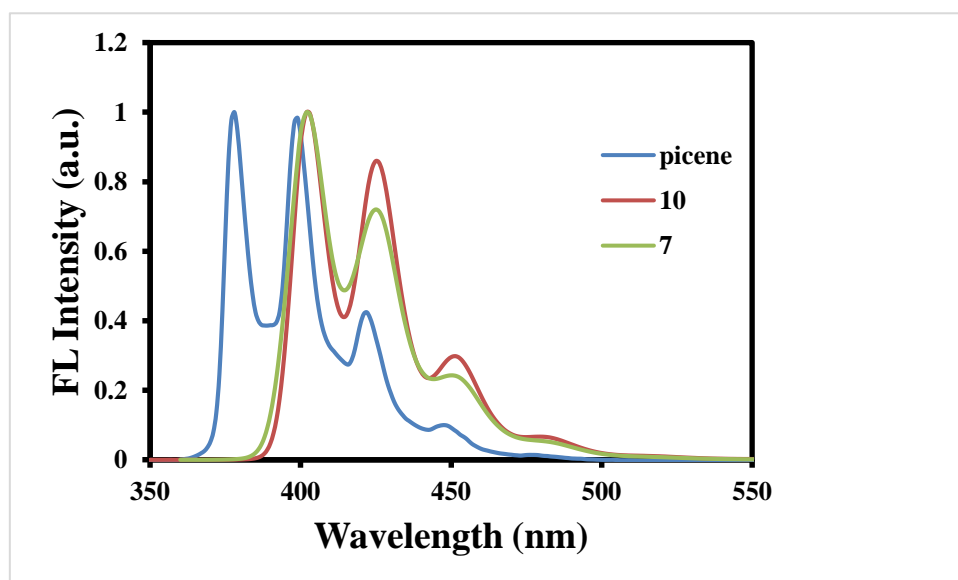


Fig. 3-6. Normalized fluoresce spectra of **7**, **10** and parent picene in  $\text{CHCl}_3$ .

**Table 3-1.** UV-vis and Fluorescence spectral data for **7**, **10** and picene in CHCl<sub>3</sub>

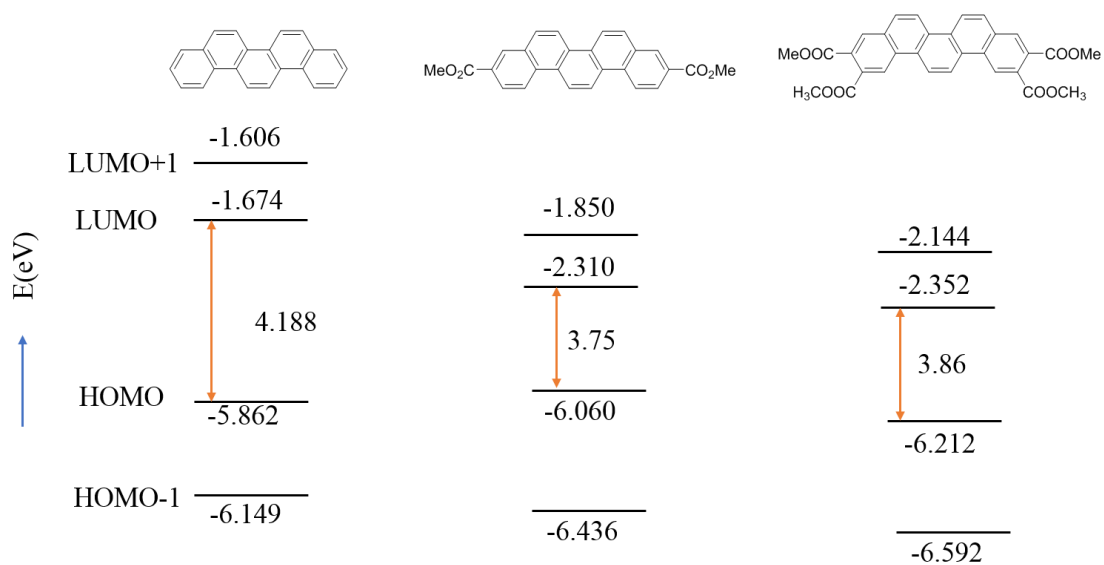
compound	$\lambda_{\text{max}}^{\text{Abs}}$	$\epsilon$ ,	$\lambda_{\text{max}}^{\text{FL}}$
	nm	M <sup>-1</sup> cm <sup>-1</sup>	nm
picene	376	886	378
<b>7</b>	394	1290	403
<b>10</b>	398	4995	403

### 3.2.3 Theoretical analysis for the electronic features

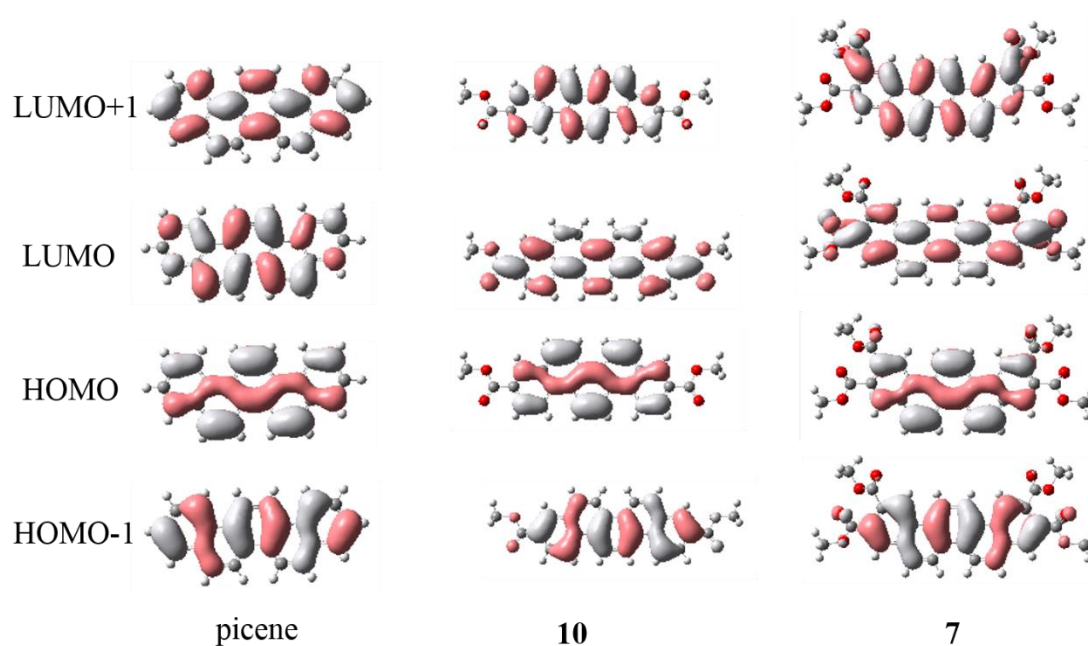
Density functional theory (DFT) calculations were performed on compounds **7** and **10** to better understand their intrinsic electronic structures at the molecular level in detail. The calculations were conducted at the B3LYP/6-31+G(d) level by using Gaussian 09 package. Electronic transitions were calculated by time-dependent (TD) DFT method at the TD-B3LYP/6-31+G(d) level.

The schematic energy-level diagrams and frontier orbital distributions for picene and **7**, **10** are shown in Fig. 3-7. It was obvious that the introduction of the electron-withdrawing ester group in picene core resulted in decreasing the HOMO and LUMO energy levels. The frontier molecular orbital (FMO) energy levels for compound **10** were calculated to be -6.06 eV and -2.31 eV for HOMO and LUMO, respectively. The FMO levels were significantly lower than those of the parent picene due to the introduced two ester groups. The presence of the four ester groups end-capping at the both edges of compound **7** resulted in the lowest HOMO and LUMO energy levels of -6.21 eV and -2.35 eV, respectively. The bandgap of compound **7** (3.86 eV) was similar with that of compound **10** (3.75 eV).

Calculated molecular orbitals are also illustrated in Fig. 3-7. For compounds **7** and **10**, the shapes of both the HOMO and HOMO-1 are quite similar, the HOMO in these molecules was delocalized on the picene core with the mirror plane along the molecular C<sub>2</sub> axis. Thus, ester substituent effects on the occupied MOs were rather small. By contrast, the distribution of the LUMO and LUMO+1 was inverted by the introduction of the ester groups. Thus, the LUMO+1 orbital of picene was stabilized by the ester group to be the LUMO of compounds **7** and **10**. LUMO orbitals of ester modified picenes **7** and **10** evenly delocalized over the  $\pi$ -conjugated framework with two nodal planes along the long axis of the molecule. The substitution by the ester groups made the HOMO-LUMO energy gap smaller than that of picene. The result is consistent with that absorption spectra of compounds **7** and **10** red-shifted compared to the parent picene.



(a)



(b)

**Fig. 3-7.** Schematic energy-level diagram (a) and molecular orbitals (b) for picene, compound **7**, and **10**.

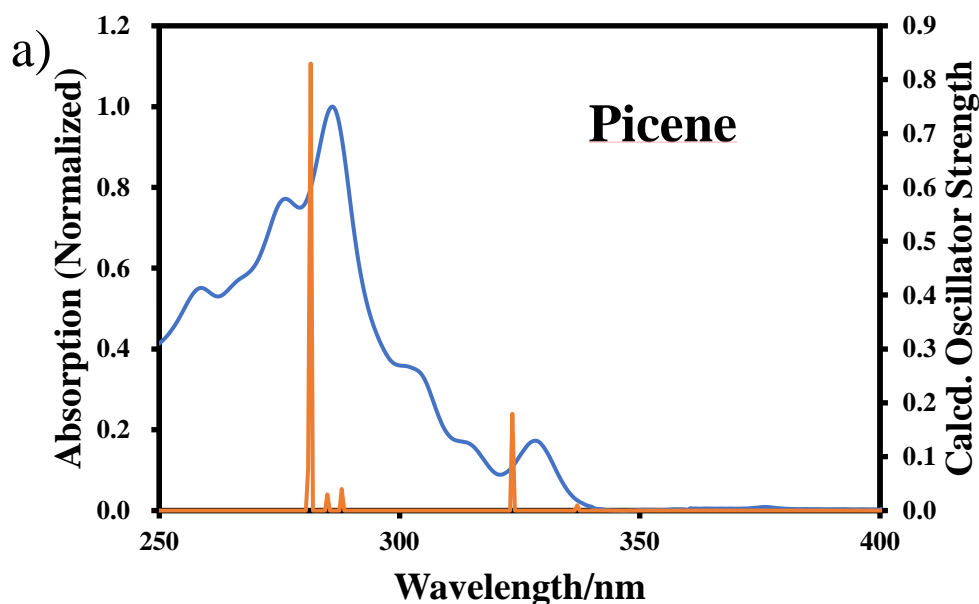
The investigation is extended to time-dependent density functional theory (TD-DFT) calculations at the TD-B3LYP/6-31+G(d) level to understand the excited-state behavior of the functionalized picenes **7** and **10**. The calculated maximum absorption



wavelengths ( $\lambda_{\max}$ ), oscillator strength ( $f$ ), and corresponding transitions are listed in Table 3-3, and Table 3-4.

The  $S_0 \rightarrow S_1$  transition for phenacenes consists of excitation a mixture of electronic transitions HOMO  $\rightarrow$  LUMO+1 and HOMO-1  $\rightarrow$  LUMO ( $^1L_b$  band). The officing of the transition is very low as it is a forbidden transition. TD-DFT calculation on picene molecule showed that transition from  $S_0$  to the lowest-singlet excited state  $S_1$  is  $^1L_b$  in character with very low oscillator strength ( $f$ ) 0.003. This excitation ( $S_0 \rightarrow S_1$ ) results from HOMO to LUMO+1 and HOMO-1 to LUMO transitions. On the other hand,  $S_0 \rightarrow S_2$  transition band is stronger ( $f = 0.17$ ) and transition is largely dominated from HOMO-LUMO transition in accordance with absorption spectra.

The calculated electronic transitions of **7** and **10** were compared with their experimental absorption spectra (Fig. 3-8). The calculated wavelengths are in good agreement with the experimental absorption bands. The first absorption band of  $\lambda_{\max}$  397 nm of compound **10** with small intensity is assigned to the electronic transition of HOMO  $\rightarrow$  LUMO (Table 3-3). The first absorption band at  $\lambda_{\max}$  393 nm of compound **7** with small intensity is assigned to the electronic transition of HOMO  $\rightarrow$  LUMO.



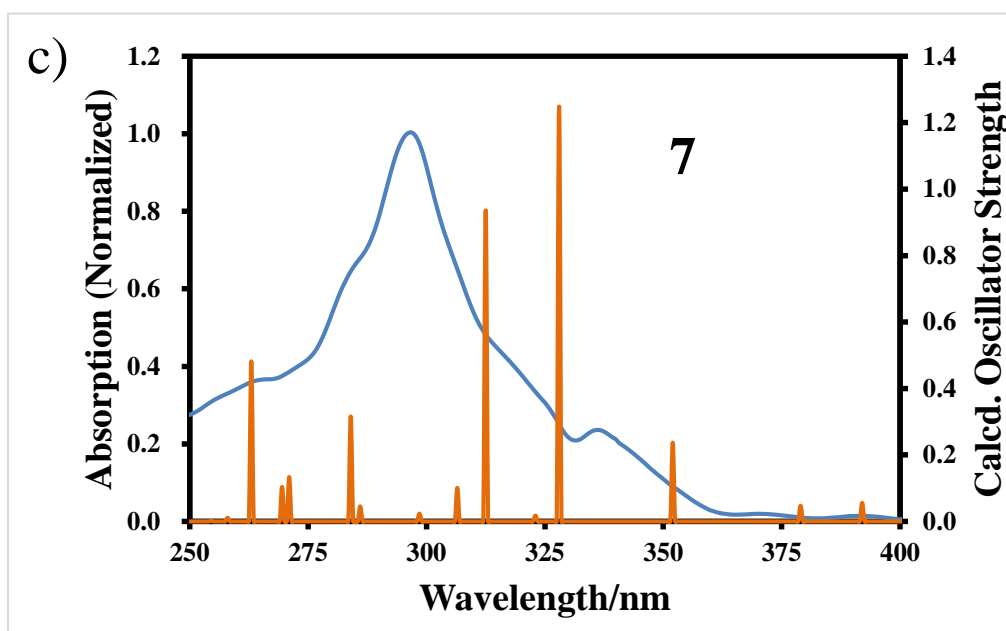
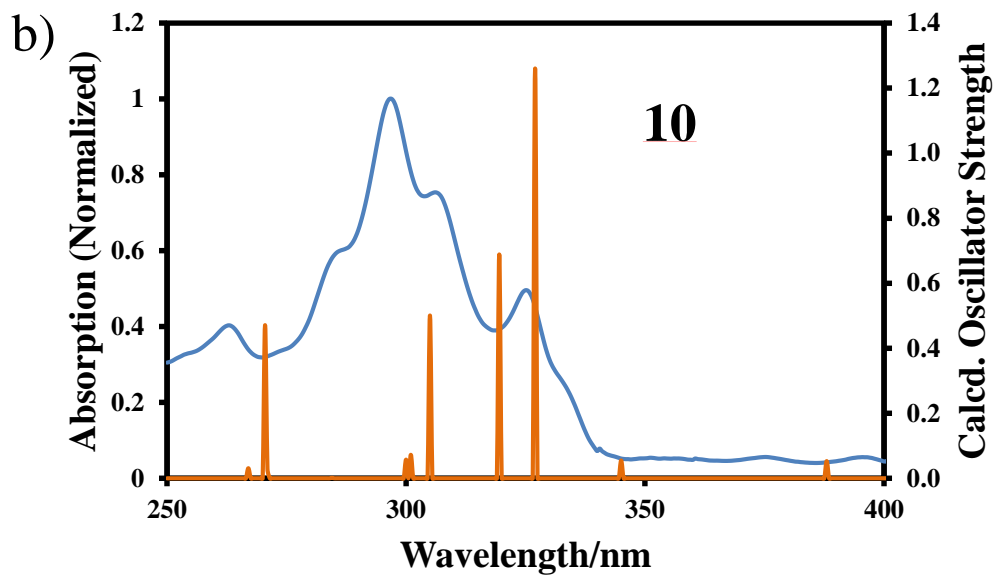


**Fig. 3-8.** Normalized absorption spectra of picene (a), **10** (b) and **7** (c) in  $\text{CHCl}_3$ . The vertical orange bars represent calculated transition wavelengths and oscillator strengths at the TD-DFT B3LYP/6-31+G(d) level.

**Table 3-2.** Calculated electronic transitions of **picene** in TD-DFT B3LYP/6-31+G(d)

Excited state	Transition wavelength	Oscillator strength	Configuration
1	337.38	0.0063	72→74 -0.40210 73→75 0.56071
2	323.41	0.1751	72→75 0.27574 73→74 0.64189 (HOMO→LUMO)
3	288.12	0.0391	71→74 0.11108 72→74 -0.33748 73→75 0.33299 73→76 0.48983
4	285.25	0.026	70→74 0.11932 71→75 0.43831 72→75 -0.11935 73→77 -0.12660 73→78 -0.11566
5	281.48	0.8316	71→75 -0.15596 72→75 0.62241 73→74 -0.26207
6	280.86	0.0781	71→74 -0.34089 72→74 0.43241 73→75 0.20974 73→76 -0.36912

**Table 3-3.** Calculated electronic transitions of **10** in TD-DFT B3LYP/6-31+G(d)

Excited state	Transition wavelength	Oscillator strength	Configuration
1	387.92	0.0528	102→105 -0.19069 103→104 0.67139 (HOMO→LUMO)
2	344.95	0.0548	102→104 0.53152 103→105 0.45700
3	326.87	1.2603	101→104 0.26903 102→104 -0.39714 102→107 -0.10110 103→105 0.45088 103→106 0.21271
4	319.37	0.6884	101→104 0.32790 102→104 0.22256 102→107 -0.17349 103→105 -0.27537 103→106 0.47491
5	305.19	0.5006	101→104 0.50536 102→107 -0.12417 103→106 -0.46460
6	301.13	0.0722	102→105 0.50287 102→106 -0.12409 103→104 0.14654 103→107 -0.42238

**Table 3-4.** Calculated electronic transitions of **7** in TD-DFT B3LYP/6-31+G(d)

Excited state	Transition wavelength	Oscillator strength	Configuration
1	379.01	0.0471	132→135 0.24931 133→134 0.65147 (HOMO→LUMO)
2	352	0.2371	132→134 -0.25234 133→135 0.65362
3	327.85	1.2485	131→134 -0.19822 132→134 0.57856 132→136 -0.18702 133→135 0.19664 133→137 -0.18204
4	323.09	0.0175	133→136 0.67973
5	312.71	0.9359	131→134 0.38139 132→134 0.30084 132→136 0.33880 133→135 0.17061 133→137 0.32156
6	306.59	0.1011	132→135 0.63520 133→134 -0.24276

### 3.3 FET characteristics

The possibility was examined to know whether the ester modified picene **7** serve as active layer of FET, FET device based on molecule were fabricated by using the compound **7** in bottom-gate, top-contact configuring. Thermally evaporated semiconductor layer was deposited on SiO<sub>2</sub>/Si substrate (Fig. 3-9).

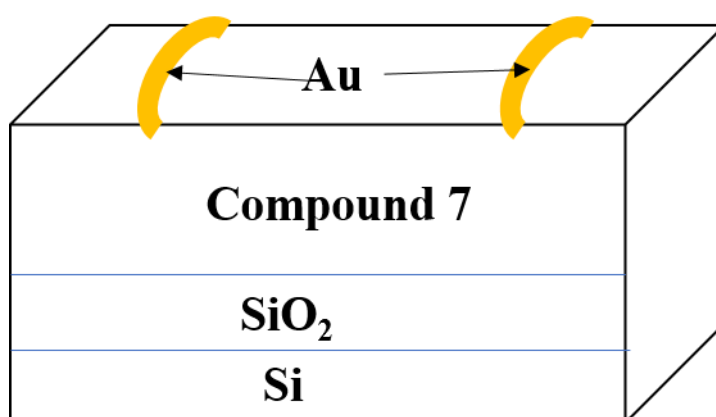


**Fig. 3-9.** FET device structure by using compound **7** as the active layer.

The absolute drain current ( $I_D$ ) curves were plotted as a function of absolute gate voltage ( $V_G$ ), as shown in Fig. 3-10 (a) for n-type operation and Fig. 3-11 (a) for p-type operation, where the drain voltage ( $V_D$ ) was fixed at -100V. The output curves are shown in Fig. 3-10 (b) for n-type operation and Fig. 3-11 (b) for p-type operation. It was observed that compound **7** did not serve as the active layer of the FET devices, under the current device fabrication and measurement conditions.

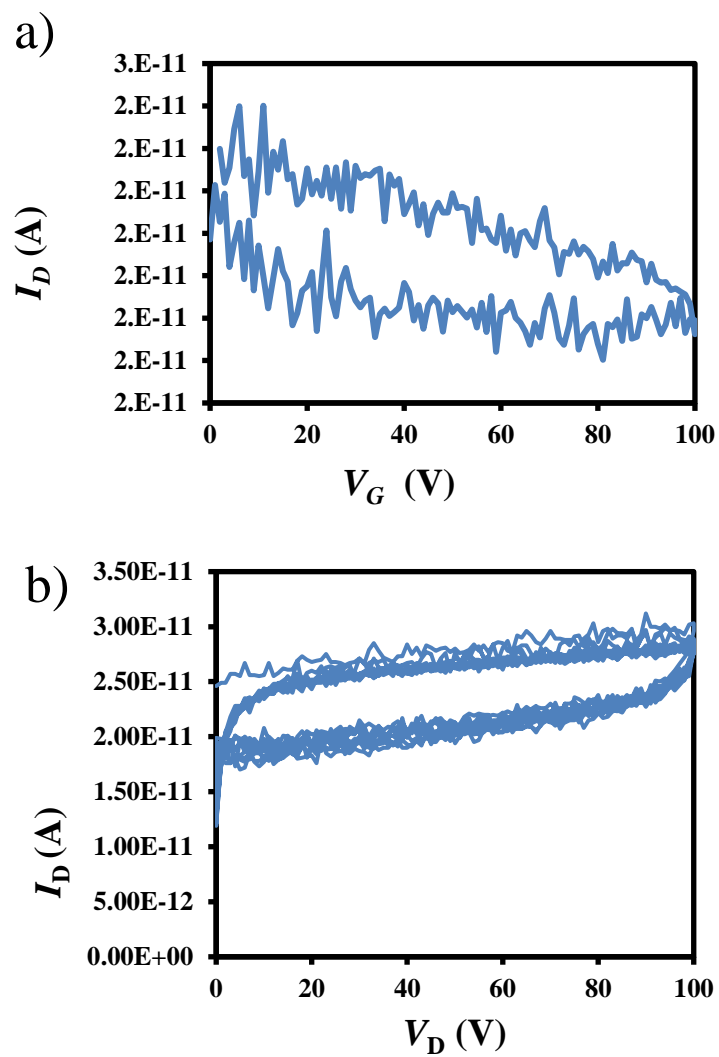


**Fig. 3-10.** Transfer (a) and output (b) curves of n-type operation for compound 7.

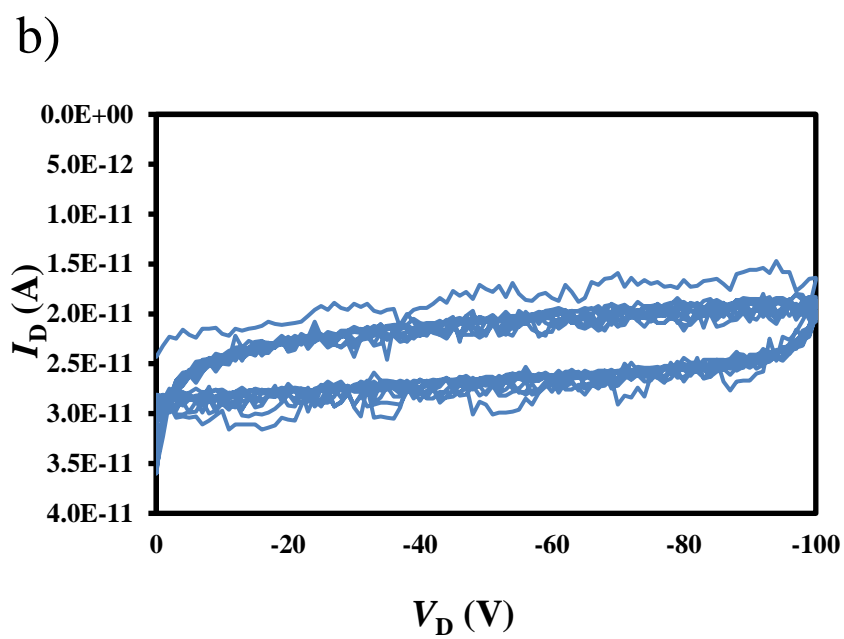
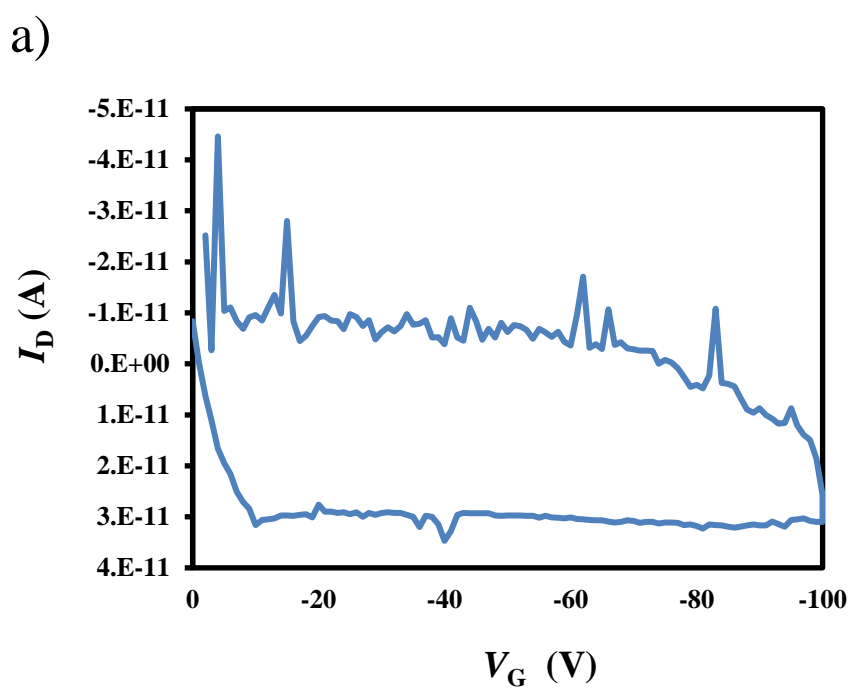


**Fig. 3-11.** Transfer (a) and output (b) curves of p-type operation for compound 7.



### 3.4 Conclusion

The two novel picene derivatives containing ester group were synthesized by using Mallory photocyclization as the key step. For the series of ester functionalized picenes it has been shown that the inclusion of the electron-withdrawing ester group lowers the energy level of the frontier molecular orbitals and enhances the solubility in common organic solvents. The possibility was examined to know whether the tetra-ester **7** serve as active layer of FETs. A FET device based on the molecule were fabricated in bottom-gate, top-contact configuring by thermal evaporation onto SiO<sub>2</sub>/Si substrate. Up to now, it was observed that compound **7** did not serve as the active layer of the FET devices, under the current device fabrication and measurement conditions.

### 3.5 Experimental Section

**Dimethyl-5-bromonaphthalene-2,3-dicarboxylate (5):** Compound **2** (954 mg, 3.46 mmol) was dissolved in MeOH (100 ml), and H<sub>2</sub>SO<sub>4</sub> (2 ml) was dropwise added into the mixture carefully. The mixture was refluxed overnight until TLC analysis revealed the reaction had proceeded to completion. The solution was cooled to room temperature, then the solvent was removed. The residue was extracted with EtOAc and washed with saturated aqueous NaHCO<sub>3</sub> solution. The organic phase was concentrated to obtain white solid of **5** (1.0 g, 90.2%). M.p. 90-91°C. <sup>1</sup>H NMR: (600 MHz, CDCl<sub>3</sub>) δ<sub>H</sub> 8.63 (s, 1H), 8.26 (s, 1H), 7.92 (d, *J* = 7.4 Hz, 1H), 7.89 (d, *J* = 8.4 Hz, 1H), 7.47 (dd, *J* = 8.2, 7.4 Hz, 1H), 3.99 (s, 3H), 3.97 (s, 3H). <sup>13</sup>C NMR: (151 MHz, CDCl<sub>3</sub>) δ<sub>C</sub> 167.96, 167.75, 134.72, 132.67, 132.36, 130.69, 130.27, 129.44, 129.36, 129.01, 128.67, 123.61, 53.01, 52.97. IR (neat) ν<sub>max</sub> 1719 (-C=O-), 1265, 1254 (-C-O-C-), 1198, 1047, 753 cm<sup>-1</sup>. Anal. Calcd. for C<sub>14</sub>H<sub>11</sub>BrO<sub>4</sub>: C, 52.04; H, 3.43. Found: C, 51.75; H, 3.23.

**(E)-1,2-bis{1-(2,3-dimethoxycarbonyl)naphthyl}ethene (6):** Compound **5** (152 mg, 0.47 mmol) and (*E*)-1, 2-bis(tributylstanny)ethene (136 mg, 0.23 mmol) were dissolved in dry toluene. The solution was deoxygenated with a stream of Ar for 30 min. Pd(PPh<sub>3</sub>)<sub>4</sub> (15 mg, 3 mol %) were added to the mixture. The resulting mixture was deoxygenated with a stream of Ar for 15 min more. The solution was refluxed overnight. The yellow solution changed to dark. The mixture was filtered and concentrated. The residue was chromatographed on silica gel by using a mixture of Hexane: EtOAc = 3:1. Then the crude mixture was further purified by reverse phase column chromatography by using MeOH and CHCl<sub>3</sub> as an eluent to afford green solid. The solid was recrystallized from MeOH to give compound **6** as yellow solid 90.8 mg (75%). M.p. 263-264°C. <sup>1</sup>H NMR (600 MHz, CDCl<sub>3</sub>) δ<sub>H</sub> 8.60 (s, 1H), 8.32 (s, 1H), 8.01 (d, *J* = 7.2 Hz, 1H), 7.95 (d, *J* = 8.2 Hz, 1H), 7.92 (s, 1H), 7.71 (dd, *J* = 8.2, 7.2 Hz, 1H), 3.97 (s, 3H), 3.94 (s, 3H). <sup>13</sup>C NMR (151 MHz, CDCl<sub>3</sub>) δ<sub>C</sub> 168.44, 168.11, 135.99, 133.93, 131.56, 131.02, 129.24, 129.23, 128.91, 128.61, 128.58, 126.80,

126.17, 52.89, 29.85. IR (neat) $\nu_{\max}$ : 2921 (-CH<sub>3</sub>), 1732 (-C=O-), 1272 (-C=O-), 969 cm<sup>-1</sup> (-C=C-). Anal. Calcd. for C<sub>30</sub>H<sub>24</sub>O<sub>8</sub>: C, 70.31; H, 4.72. Found: C, 69.91; H, 4.50.

**Tetramethyl picene-3,4,9,10-tetracarboxylate (7)**: A solution of compound **6** (90 mg, 0.175 mmol) and iodine (2.56 mg, 10 mol%) in 200 ml of CH<sub>2</sub>Cl<sub>2</sub> was purged with air. The solution was irradiated with six 352nm UV lamps (6×15W). The mixture was irradiated until TLC revealed the reaction had proceeded to completion. The solvent was removed under reduced pressure and the residue was extracted with CH<sub>2</sub>Cl<sub>2</sub>. The solution was washed with saturated Na<sub>2</sub>S<sub>2</sub>O<sub>3</sub> solution for 3 times. The organic phase was dried by MgSO<sub>4</sub> and concentrated to obtain pale yellow solid of compound **7** 73.6 mg (80.2%). M.p: 268-269°C. <sup>1</sup>H NMR (600 MHz, CDCl<sub>3</sub>)  $\delta_{\text{H}}$  9.24 (s, 2H), 9.01 (s, 2H), 8.91 (d,  $J = 9.2$  Hz, 2H), 8.41 (s, 2H), 8.11 (d,  $J = 9.1$  Hz, 2H), 4.06 (s, 6H), 4.02 (s, 6H). <sup>13</sup>C NMR (151 MHz, CDCl<sub>3</sub>)  $\delta_{\text{C}}$  168.44, 168.10, 132.76, 131.11, 130.24, 129.66, 129.61, 129.50, 129.07, 127.60, 125.32, 124.27, 122.64, 53.06, 52.97. IR (neat)  $\nu_{\max}$  2921 (-CH<sub>3</sub>), 1732 (-C=O-), 1272 cm<sup>-1</sup> (-C=O-). Anal. Calcd. for C<sub>30</sub>H<sub>22</sub>O<sub>8</sub>: C, 70.58; H, 4.34. Found: C, 70.22; H, 4.34.

**(E)-1,2-bis{1-(2-dimethoxycarbonyl)naphthyl}ethene (9)**: Compound **8** (171.6 mg, 0.65 mmol) and (E)-1, 2-bis(tributylstannyl)ethene (88.6 mg, 0.32 mmol) and Pd(PPh<sub>3</sub>)<sub>4</sub> (22.9 mg, 3 mol %) were dissolved in dry toluene (10 mL). The resulting mixture was deoxygenated with a stream of Ar for 5 min. The solution refluxed overnight. The yellow solution changed to dark. The mixture was filtered and washed with toluene. Then, the combined filtrate and washing were concentrated. The residue was column chromatographed on silica gel by using a mixture of hexane : EtOAc= 3:1. The yellow solid obtained was recrystallized from a mixture of CHCl<sub>3</sub> and MeOH to afford compound **9** yellow needles 86.1 mg (68%). M.p: 230-231°C. <sup>1</sup>H NMR (600 MHz, CDCl<sub>3</sub>)  $\delta_{\text{H}}$  8.65 (d,  $J = 1.7$  Hz, 2H), 8.28 (d,  $J = 8.9$  Hz, 2H), 8.11 (d,  $J = 8.9$ , 1.8 Hz, 2H), 7.97 (d,  $J = 7.6$  Hz, 4H), 7.91 (s, 2H), 7.62 (t,  $J = 7.7$  Hz, 2H), 4.00 (s, 6H). <sup>13</sup>C NMR (151 MHz, CDCl<sub>3</sub>)  $\delta_{\text{C}}$  167.27, 135.27, 133.58, 133.01, 131.83, 129.86, 129.16, 127.56, 126.71, 126.34, 125.69, 124.28, 52.46. IR (neat)  $\nu_{\max}$  1708 (-C=O-),

1640 (-C=C-), 1436, 1274, 1236 (-C-O-C), 773  $\text{cm}^{-1}$ . Anal. Calcd. for  $\text{C}_{26}\text{H}_{20}\text{O}_4$ : C, 78.77; H, 5.09. Found: C, 78.56; H, 4.88.

**Dimethyl picene-3,10-dicarboxylate (10)**: A solution of compound **9** (60 mg, 0.15 mmol) and iodine (2.8 mg, 10 mol%) in 150 mL of  $\text{CH}_2\text{Cl}_2$  was purged with air. The solution was irradiated with 352nm UV lamps (6×15W) until TLC revealed the reaction had proceeded to completion. The solvent was removed under reduced pressure and the residue was extracted with  $\text{CH}_2\text{Cl}_2$ . The extract was washed with saturated aqueous  $\text{Na}_2\text{S}_2\text{O}_3$  solution for 3 times. The organic phase was dried over  $\text{MgSO}_4$  and concentrated to obtain colorless solid of **10**, 60mg (95%). M.p:  $>300^\circ\text{C}$ .  $^1\text{H}$  NMR (600 MHz,  $\text{CDCl}_3$ )  $\delta_{\text{H}}$  9.00 (s, 2H), 8.91 (d,  $J = 8.7$  Hz, 2H), 8.85 (d,  $J = 9.2$  Hz, 2H), 8.75 (d,  $J = 1.8$  Hz, 2H), 8.35 (d,  $J = 8.7, 1.8$  Hz, 2H), 8.14 (d,  $J = 9.1$  Hz, 2H), 4.04 (s, 6H). IR (neat)  $\nu_{\text{max}}$  1730 (-C=O-), 1276, 1226, 1203 (-C-O-C-), 761  $\text{cm}^{-1}$ . Anal. Calcd. for  $\text{C}_{26}\text{H}_{18}\text{O}_4$ : C, 79.17; H, 4.60. Found: C, 78.88; H, 4.34.

### 3.6 References

1. T. L. Gaobo Lin, Lvbing Yuan, Wenjie Liang, Hai Xu, *Progress in Chemistry*, 2017, **29**, 1316-1330.
2. F. S. Kim, X. Guo, M. D. Watson and S. A. Jenekhe, *Adv. Mater.*, 2010, **22**, 478-482.
3. Z. Ni, H. Dong, H. Wang, S. Ding, Y. Zou, Q. Zhao, Y. Zhen, F. Liu, L. Jiang and W. Hu, *Adv. Mater.*, 2018, **30**.
4. H. Yoo, M. Ghittorelli, E. C. Smits, G. H. Gelinck, H. K. Lee, F. Torricelli and J. J. Kim, *Sci. Rep.*, 2016, **6**, 35585.
5. Y. Zhao, Y. Guo and Y. Liu, *Adv. Mater.*, 2013, **25**, 5372-5391.
6. Y. Ren, X. Yang, L. Zhou, J. Y. Mao, S. T. Han and Y. Zhou, *Adv. Funct. Mater.*, 2019, **29**, 1902105.
7. A. W. Lee, D. Le, K. Matsuzaki and K. Nomura, *ACS Appl. Electron. Mater.*, 2020, **2**, 1162-1168.
8. X. Zhou, N. Ai, Z.-H. Guo, F.-D. Zhuang, Y.-S. Jiang, J.-Y. Wang and J. Pei, *Chem. Mater.*, 2015, **27**, 1815-1820.
9. J. Zaumseil and H. Sirringhaus, *Chem. Rev.*, 2007, **107**, 1296-1323.
10. Z. Yi, S. Wang and Y. Liu, *Adv. Mater.*, 2015, **27**, 3589-3606.
11. J. Chen, Y. Jiang, J. Yang, Y. Sun, L. Shi, Y. Ran, Q. Zhang, Y. Yi, S. Wang, Y. Guo and Y. Liu, *ACS Appl. Mater. Interfaces*, 2018, **10**, 25858-25865.
12. Y. Lin, Y. Li and X. Zhan, *Chem. Soc. Rev.*, 2012, **41**, 4245-4272.
13. S. D. Collins, N. A. Ran, M. C. Heiber and T. Q. Nguyen, *Adv. Energy Mater.*, 2017, **7**, 1602242.
14. M. Kang, H. Hwang, W. T. Park, D. Khim, J. S. Yeo, Y. Kim, Y. J. Kim, Y. Y. Noh and D. Y. Kim, *ACS Appl. Mater. Interfaces*, 2017, **9**, 2686-2692.
15. Y. Zhang, C. Kim, J. Lin and T.-Q. Nguyen, *Adv. Funct. Mater.*, 2012, **22**, 97-105.
16. A. Anjali, R. Dheepika, P. M. Imran, N. S. P. Bhuvanesh and S. Nagarajan, *ACS*

*Appl. Electron. Mater.*, 2020, **2**, 2651-2661.

17. R. Dheepika, S. Sonalin, P. M. Imran and S. Nagarajan, *J. Mater. Chem. C*, 2018, **6**, 6916-6919.

18. T. Kojima, J.-i. Nishida, S. Tokito and Y. Yamashita, *Chem. Lett.*, 2008, **37**, 1122-1123.

19. K.-H. Kim, H. Yu, H. Kang, D. J. Kang, C.-H. Cho, H.-H. Cho, J. H. Oh and B. J. Kim, *J. Mater. Chem. A*, 2013, **1**, 14538.

20. P. Cudazzo, M. Gatti and A. Rubio, *Phys. Rev. B*, 2012, **86**.

21. Y. Yoshida, H. H. Yang, H. S. Huang, S. Y. Guan, S. Yanagisawa, T. Yokosuka, M. T. Lin, W. B. Su, C. S. Chang, G. Hoffmann and Y. Hasegawa, *J. Chem. Phys.*, 2014, **141**, 114701.

22. H. Okamoto, S. Hamao, H. Goto, Y. Sakai, M. Izumi, S. Gohda, Y. Kubozono and R. Eguchi, *Sci. Rep.*, 2014, **4**, 5048.

## List of publications

Facile synthesis of picenes incorporating imide moieties at both edges of the molecule and their application to n-channel field-effect transistors.

Yuxin Guo, Kaito Yoshioka, Shino Hamao, Yoshihiro Kubozono, Fumito Tani, Kenta Goto, Hideki Okamoto

RSC Advances, 2020, 10(52), 31547-31552.





## Acknowledgements

I wish to take this unique opportunity to express my deep sense of indebtedness, gratitude, and respect to my supervisor, Prof. Hideki Okamoto. He initiated me into this very fascinating and challenging field of organic electronics. His constant support, encouragement and timely interventions are responsible for making this thesis a reality. What he has impressed me is not only his professional knowledge but also his devoted attitude toward research.

It is my pleasure acknowledge Prof. Yoshihiro Kubozono and his members for the measurements of organic semiconductors performance; and the Micro-Elemental-Analysis Laboratory of Okayama University for the combustion analyses of the novel compounds; and the SC-NMR Laboratory of Okayama University for the measurements of NMR spectroscopy. Their measurements results provide data support for the present research topic for the Ph.D study.

I would like to express my heartfelt gratitude to all laboratory members, Lei Wang, Kazumasa Itani, Naoki Chiba, Kaito Yoshioka, Yukiko Ohguma, Keiko Kozasa and Tomoko Nakatsuka, they have been with me at every moment during my studies, and I am so pleased that I can share my accomplishments with them. All members get well along with each other just like a big family and the experience impresses the author deeply and beautifully. In particular, the author is grateful to them, their generous help made the author adapt to the new environment of study and life in Japan as quickly as possible.

I thank each and every person associated directly or indirectly with the success of this endeavor.

Yuxin Guo

2021.03



## **Appendix**

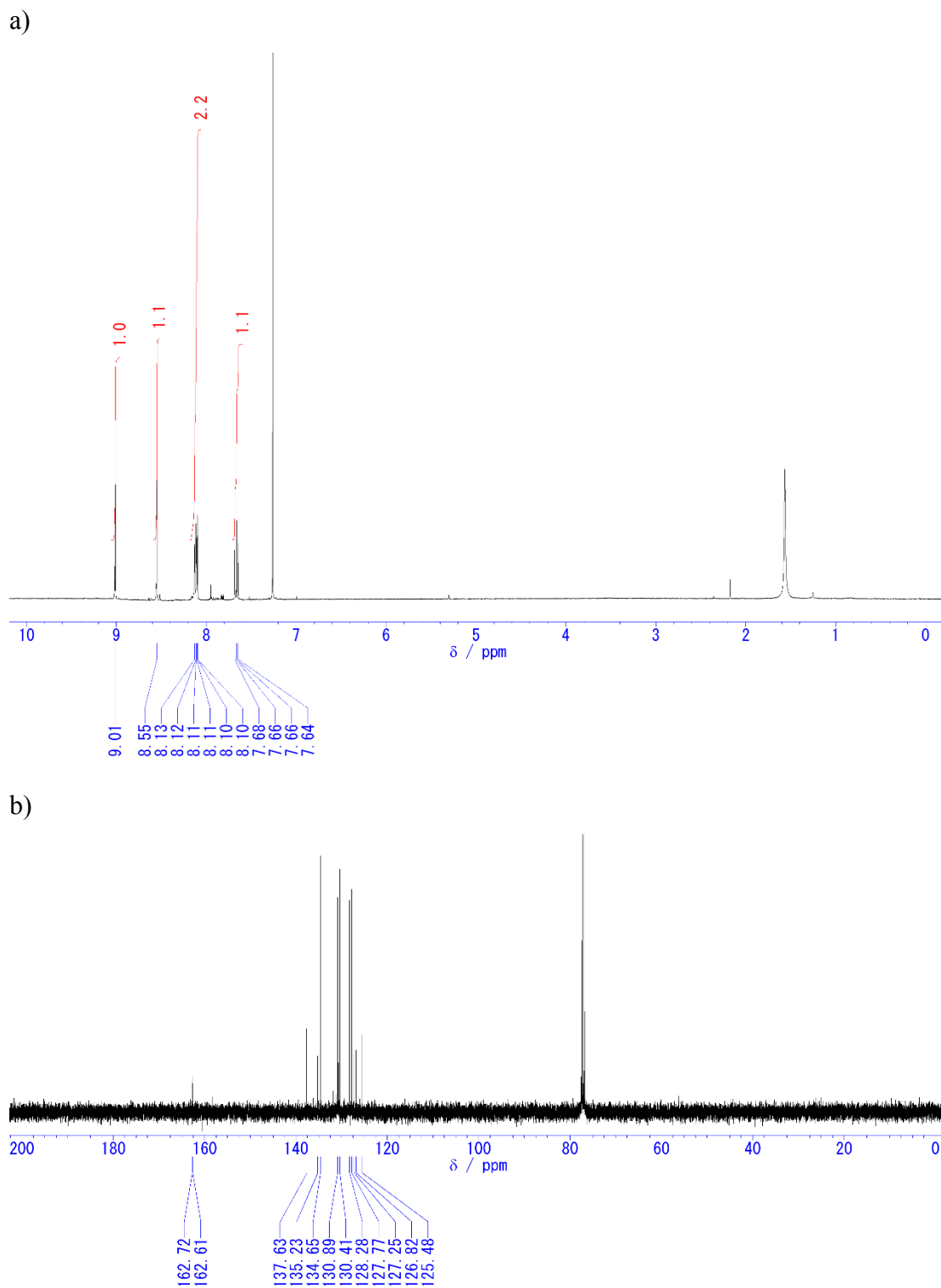
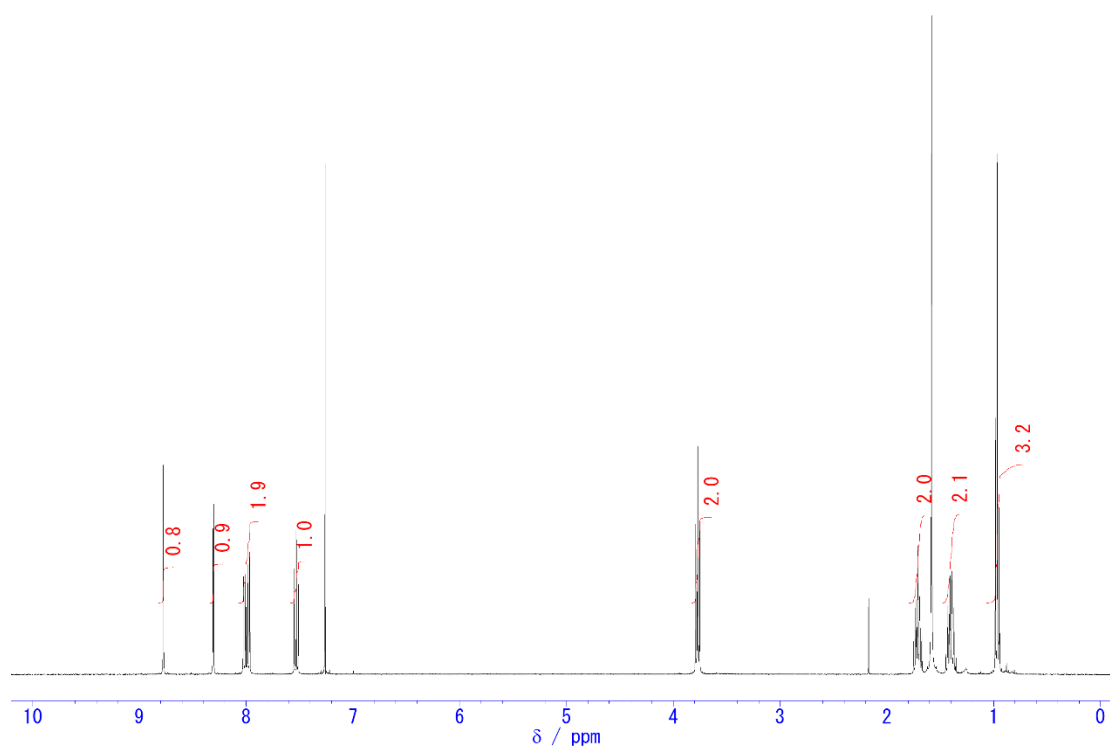


**Fig. S2-1.** (a)  $^1\text{H}$  NMR (400 MHz) and (b)  $^{13}\text{C}$  NMR (100 MHz) spectra of 4-bromo-2,3-naphthalenedicarboxylic anhydride **2** ( $\text{CDCl}_3$ ).

a)



b)

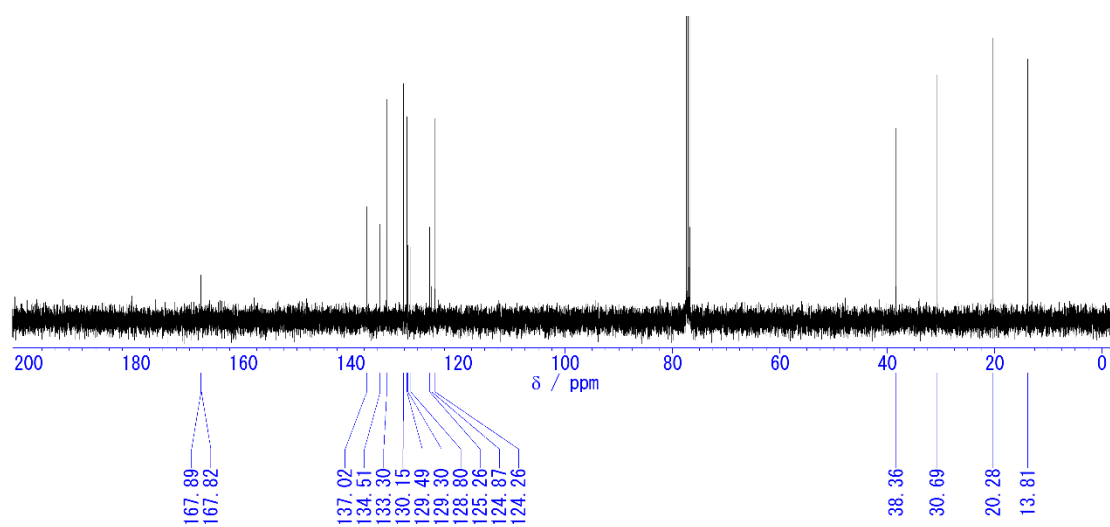


Fig. S2-2. <sup>1</sup>H NMR (400 MHz) and (b) <sup>13</sup>C NMR (100 MHz) spectra of *N*-butyl-4-bromonaphthalene-2,3-dicarboximide **3a** (CDCl<sub>3</sub>).

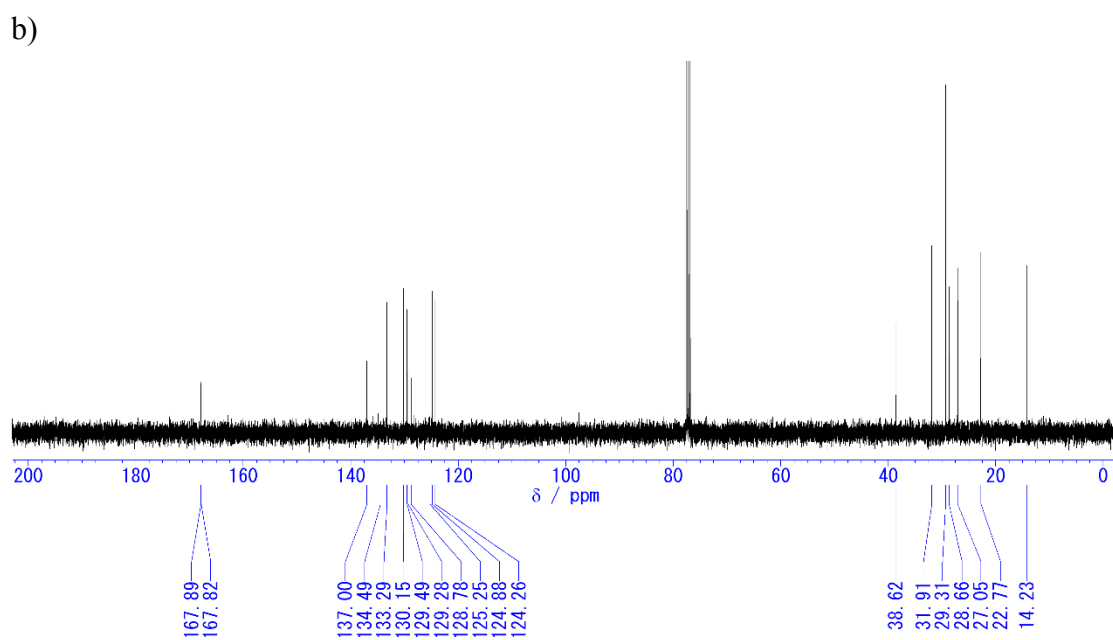
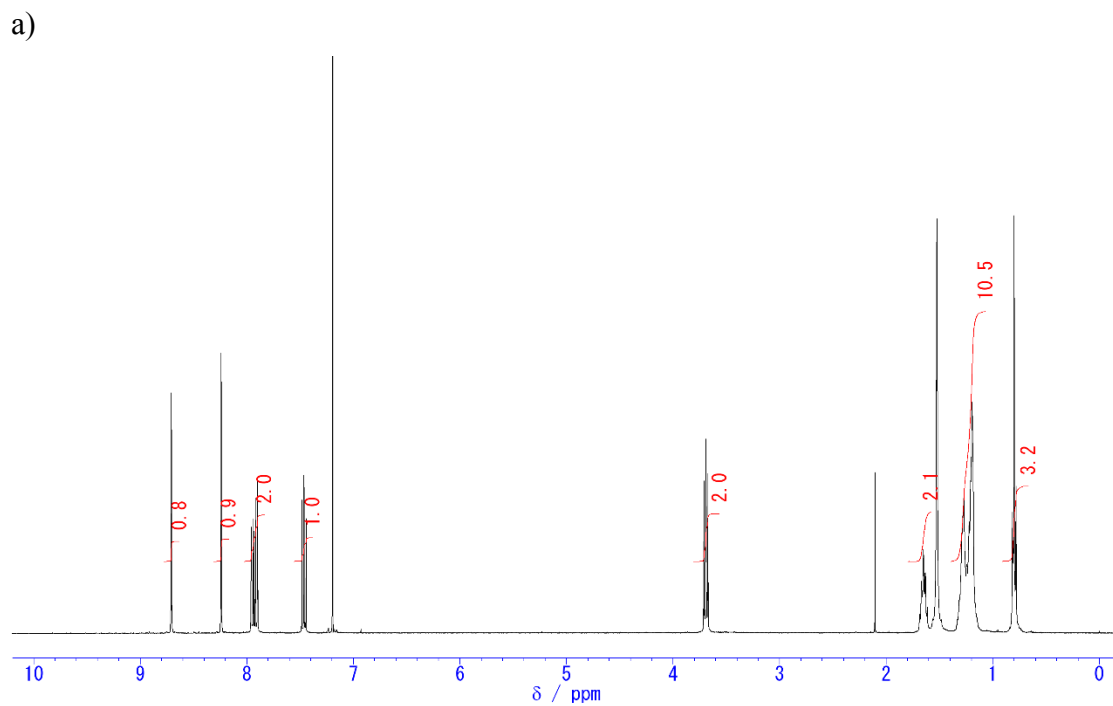
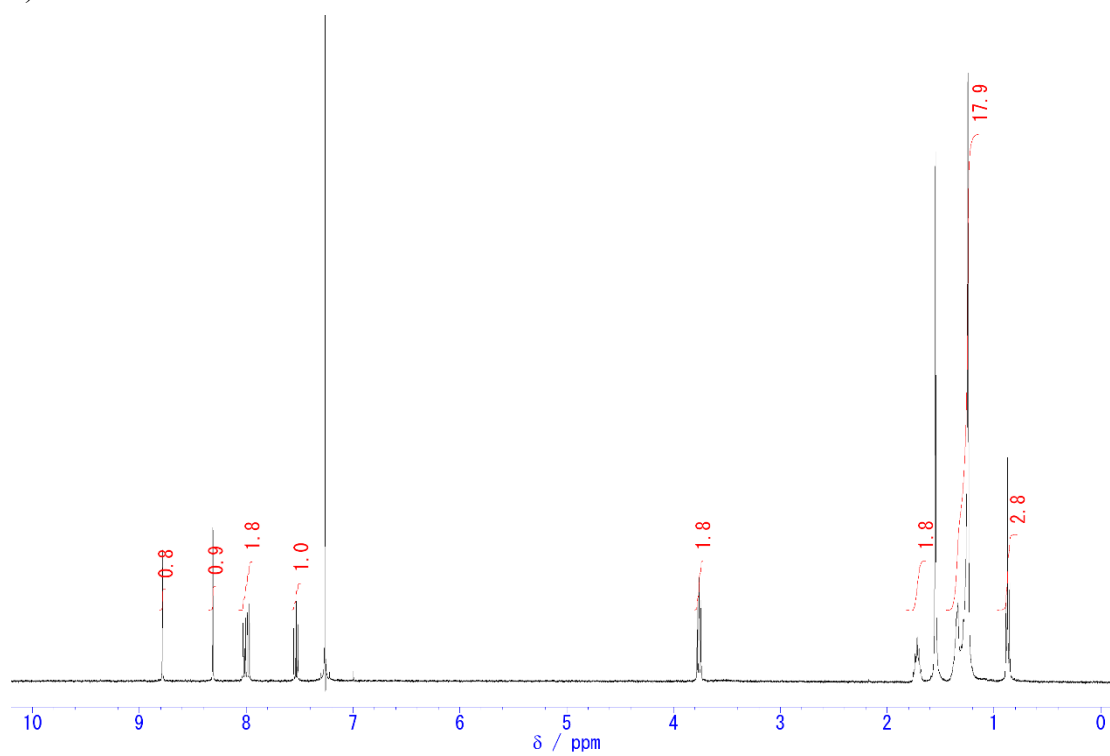


Fig. S2-3.  $^1\text{H}$  NMR (400 MHz) and (b)  $^{13}\text{C}$  NMR (100 MHz) spectra of **3b** ( $\text{CDCl}_3$ ).

a)



b)

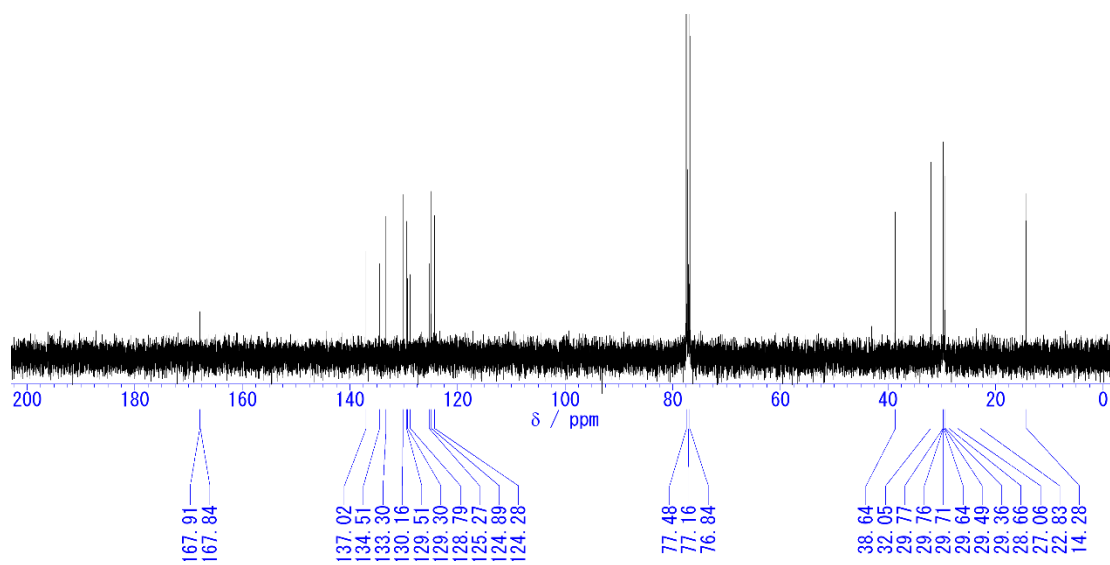
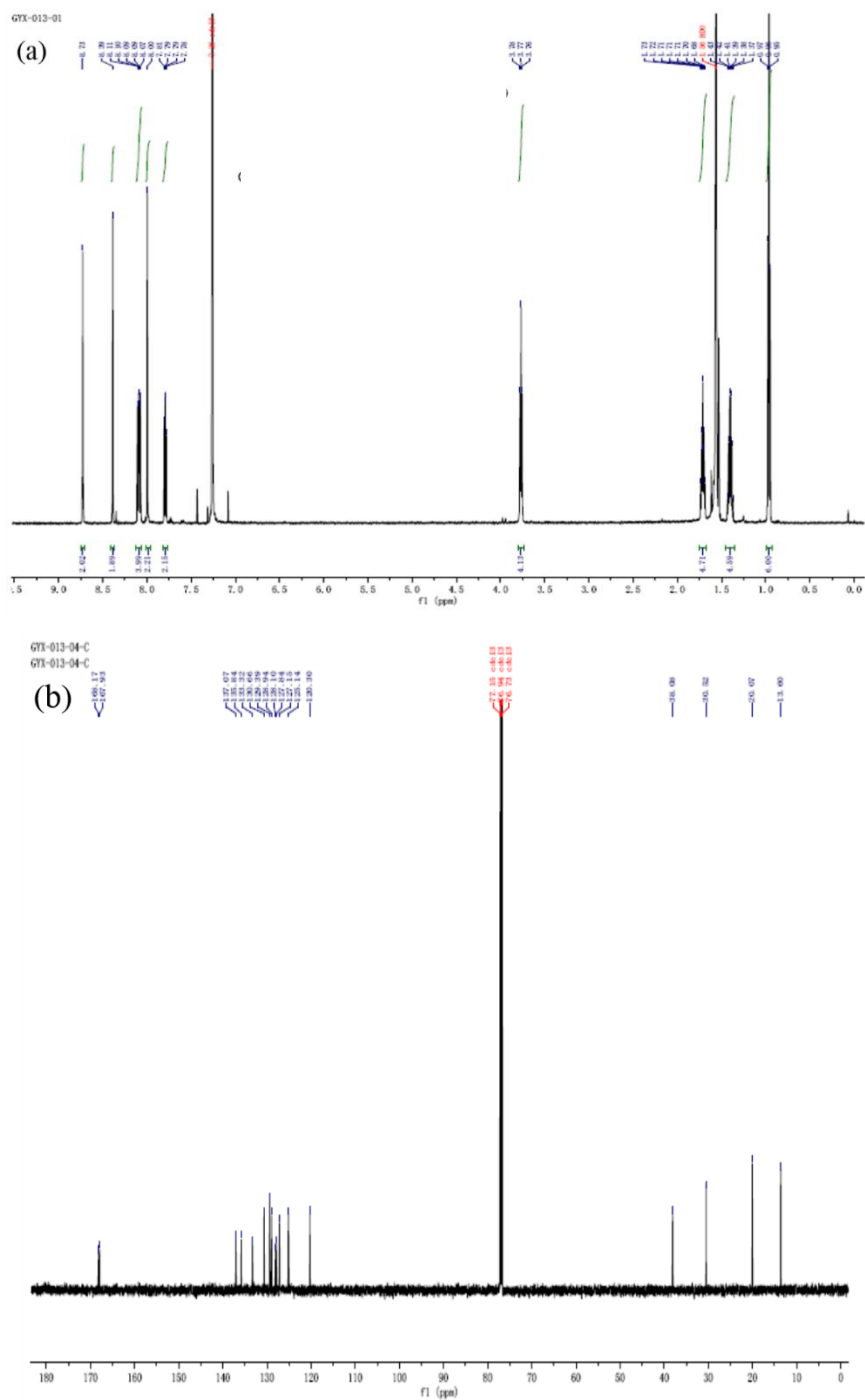
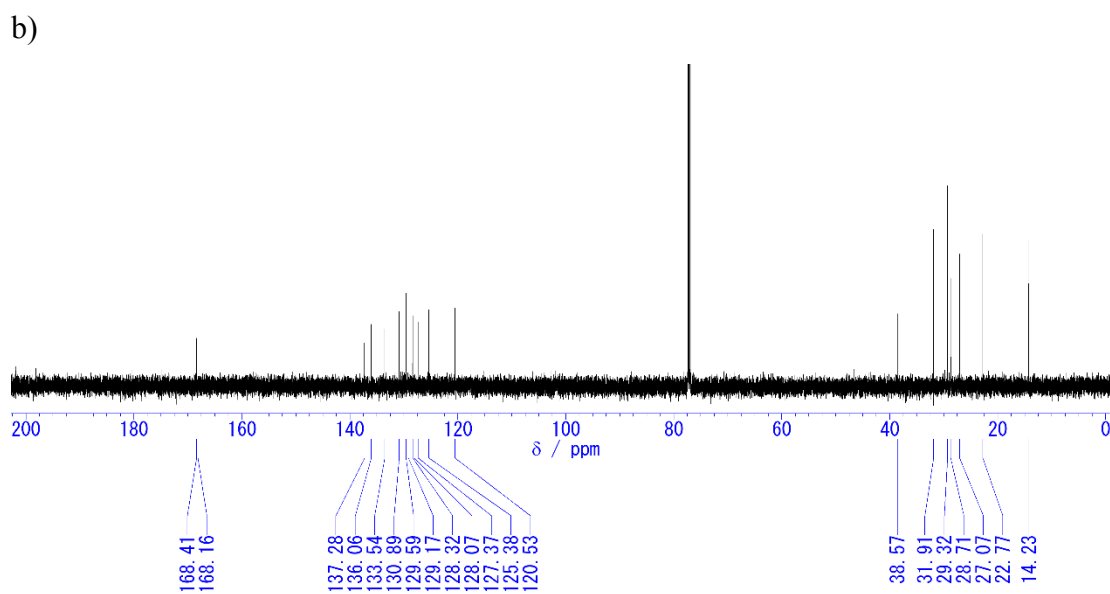
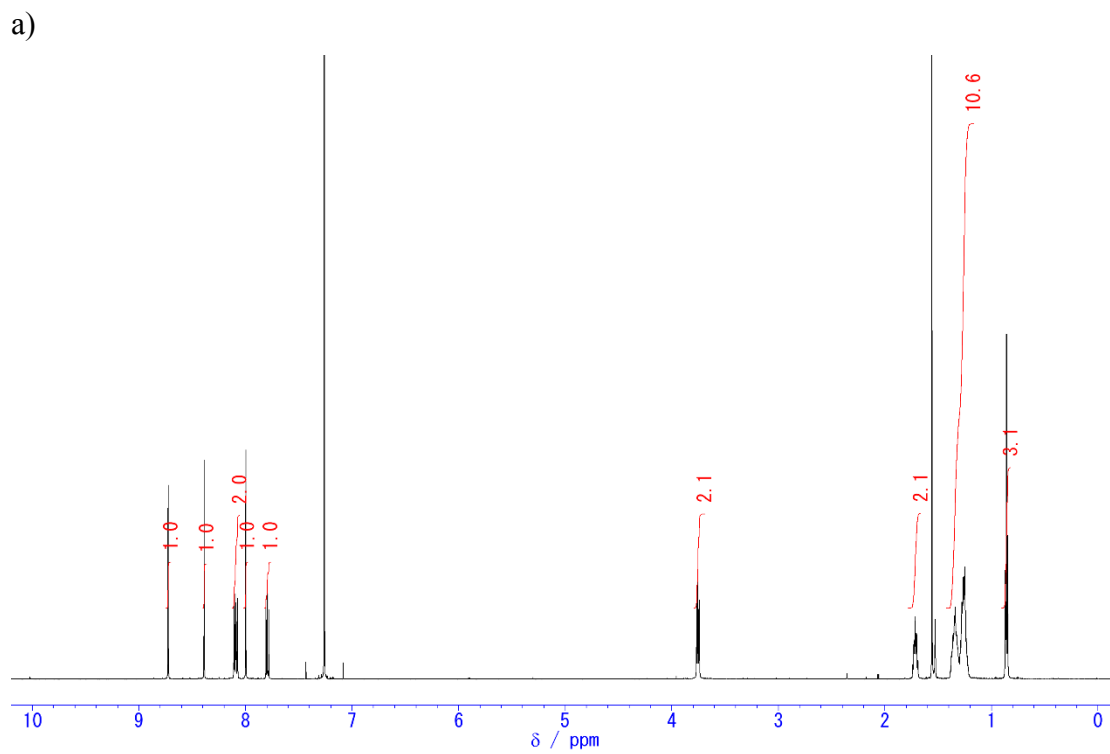


Fig. S2-4. (a)  $^1\text{H}$  NMR (400 MHz) and (b)  $^{13}\text{C}$  NMR (100 MHz) spectra of **3c** ( $\text{CDCl}_3$ ).



**Fig. S2-5.**  $^1\text{H}$  NMR (600 MHz) and (b)  $^{13}\text{C}$  NMR (151 MHz) spectra of **4a** ( $\text{CDCl}_3$ ).





**Fig. S2-6.** (a)  $^1\text{H}$  NMR (600 MHz) and (b)  $^{13}\text{C}$  NMR (151 MHz) spectra of **4b** ( $\text{CDCl}_3$ ).

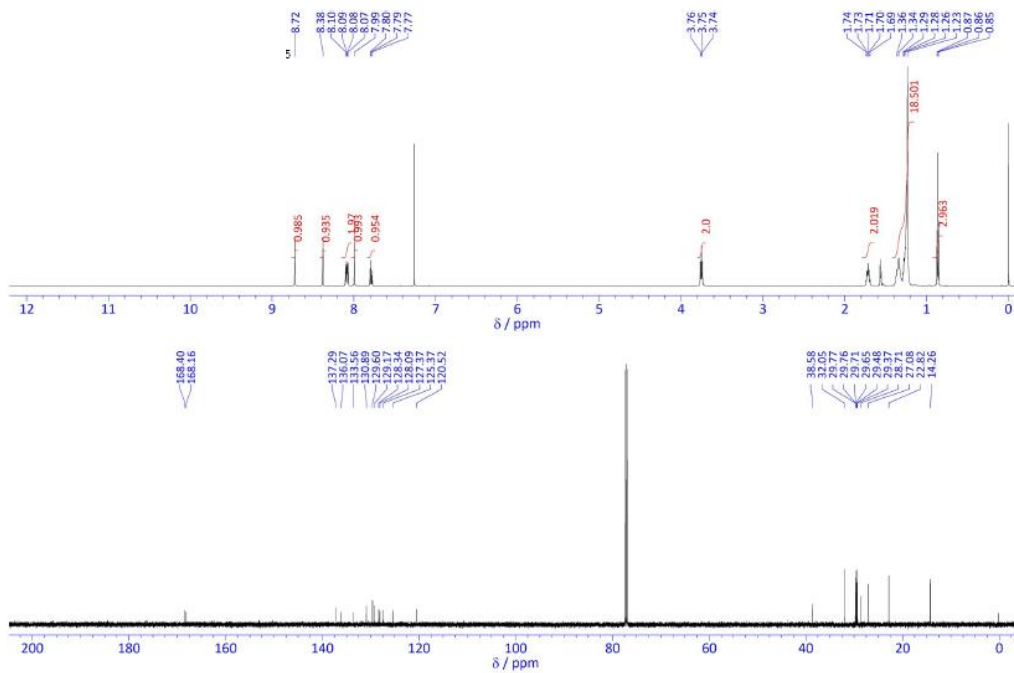


**Fig. S2-7.** (a)  $^1\text{H}$  NMR (600 MHz) and (b)  $^{13}\text{C}$  NMR (151 MHz) spectra of **4c** ( $\text{CDCl}_3$ ).

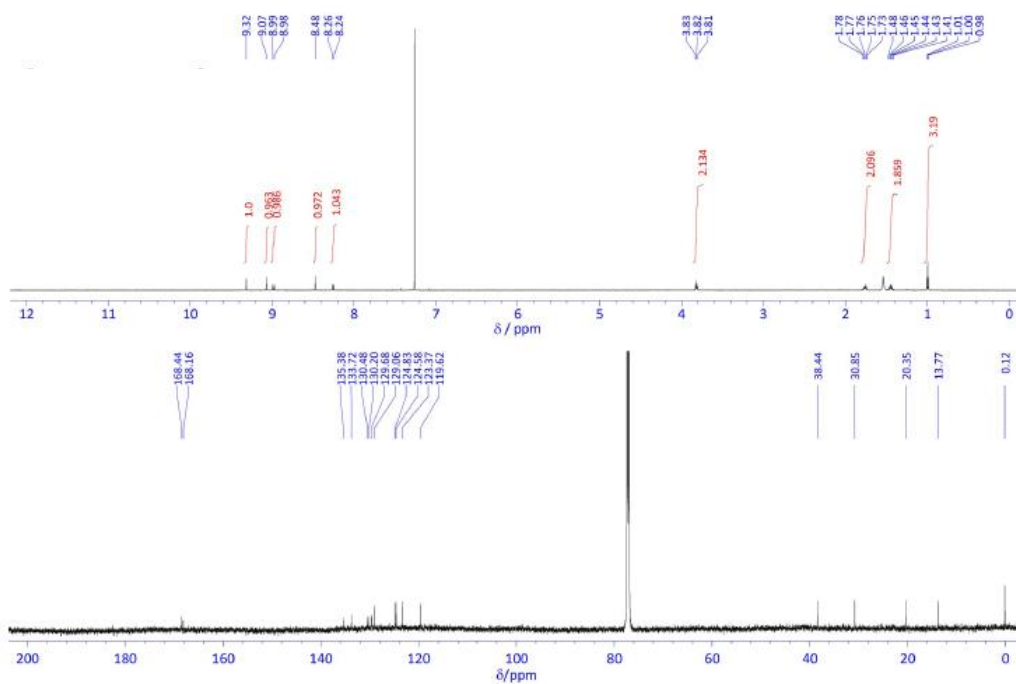
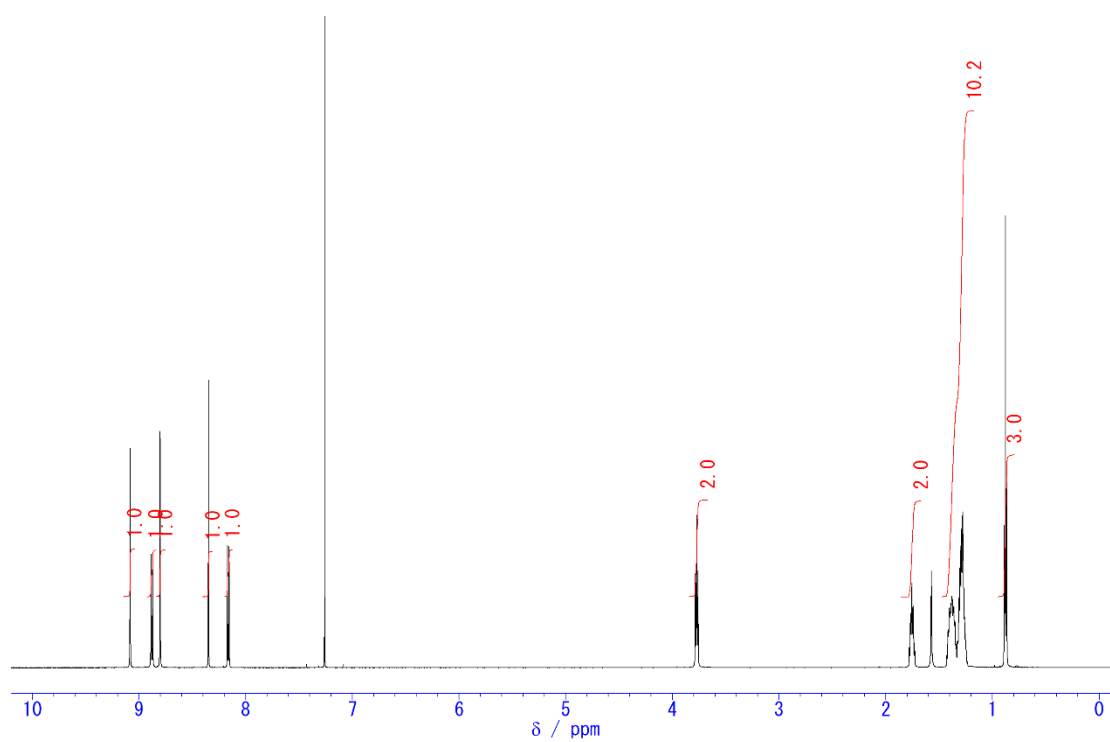


**Fig. S2-8.** (a)  $^1\text{H}$  NMR (600 MHz) and (b)  $^{13}\text{C}$  NMR (151 MHz) spectra of **C4-PicDI** ( $\text{CDCl}_3$ ).

a)



b)

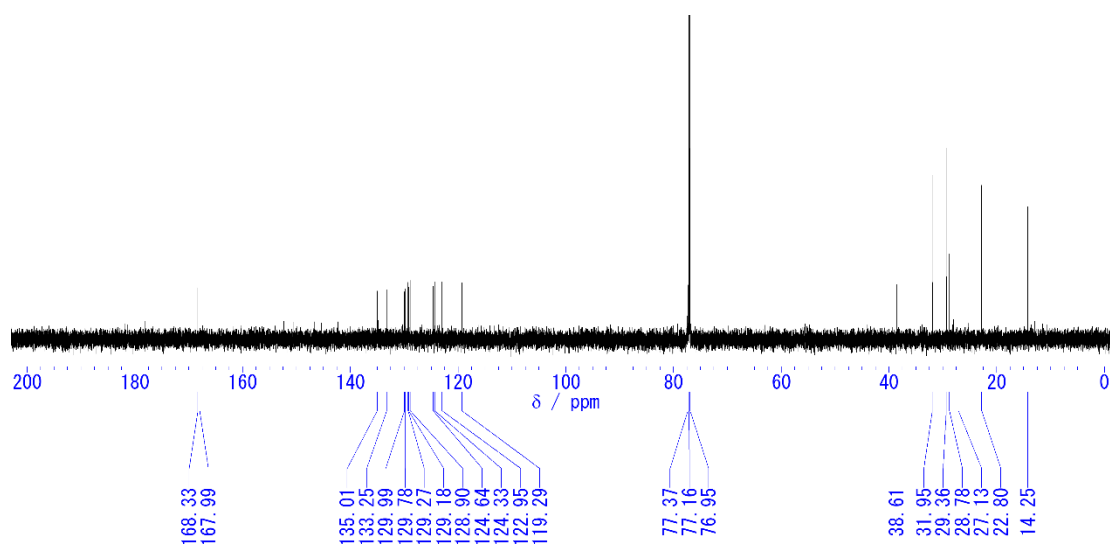
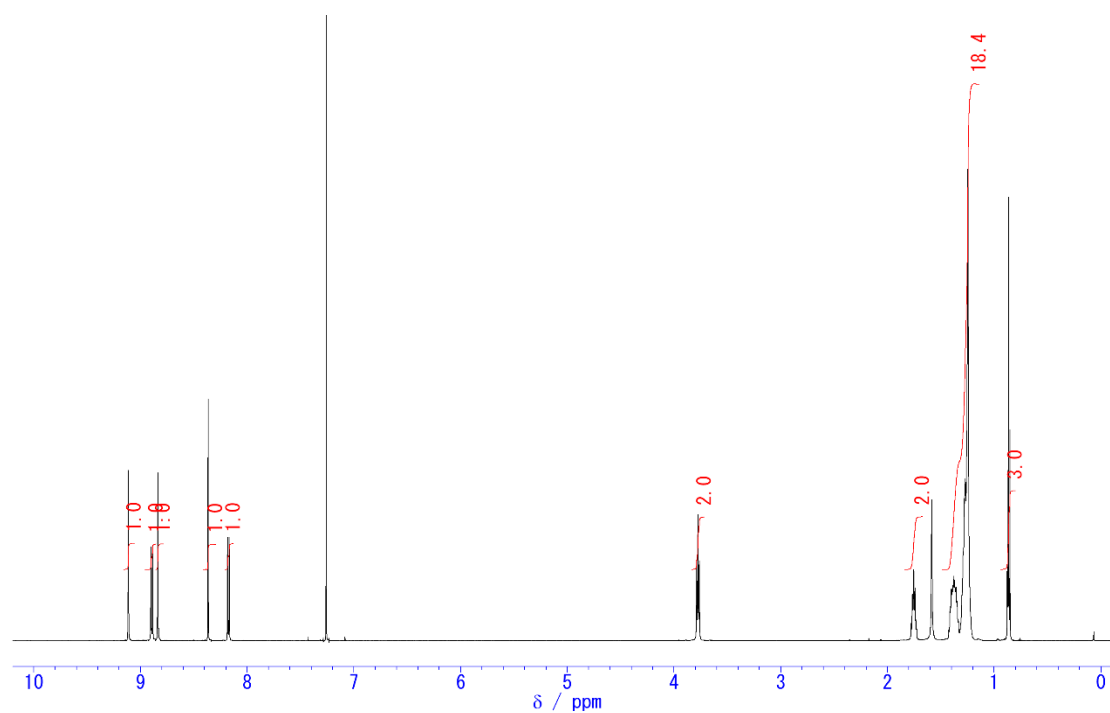


**Fig. S2-9.**  $^1\text{H}$  NMR (600 MHz) and (b)  $^{13}\text{C}$  NMR (151 MHz) spectra of **C<sub>8</sub>-PicDI** ( $\text{CDCl}_3$ ).

a)



b)

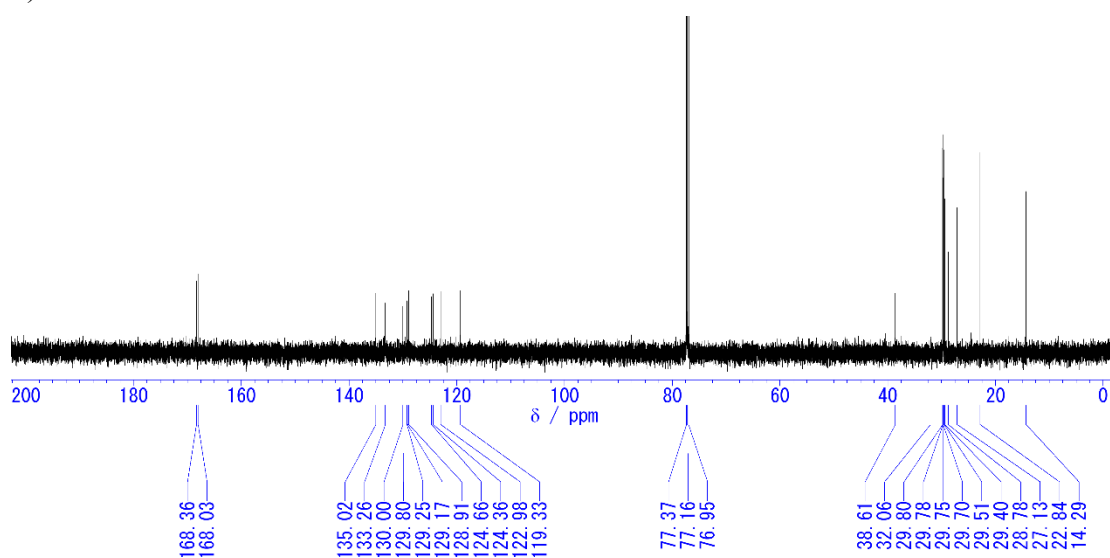
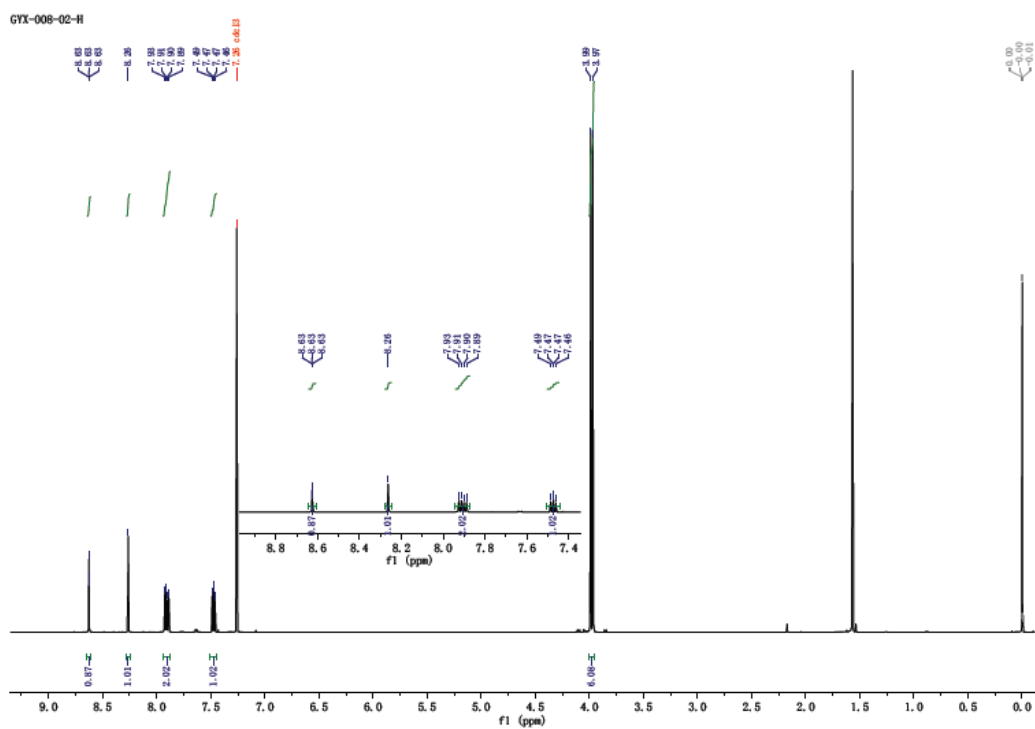


**Fig. S2-10.** (a)  $^1\text{H}$  NMR (600 MHz) and (b)  $^{13}\text{C}$  NMR (151 MHz) spectra of  $\text{C}_{12}\text{-PicDI}$  ( $\text{CDCl}_3$ ).

(a)



(b)

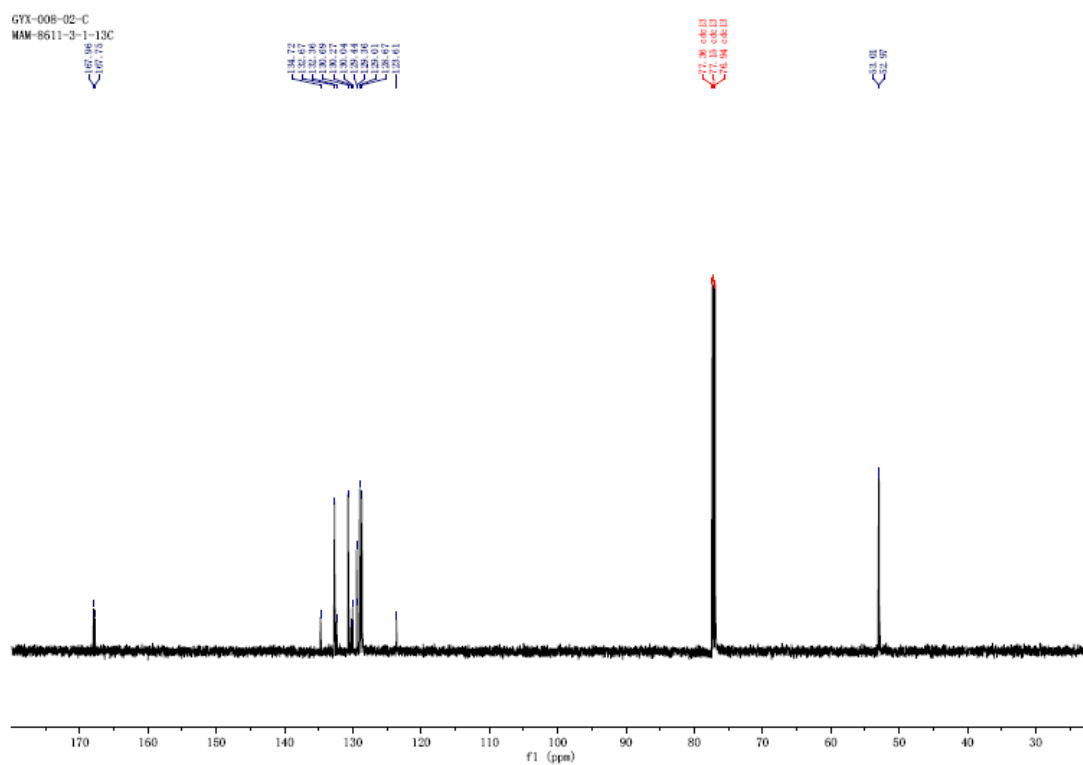
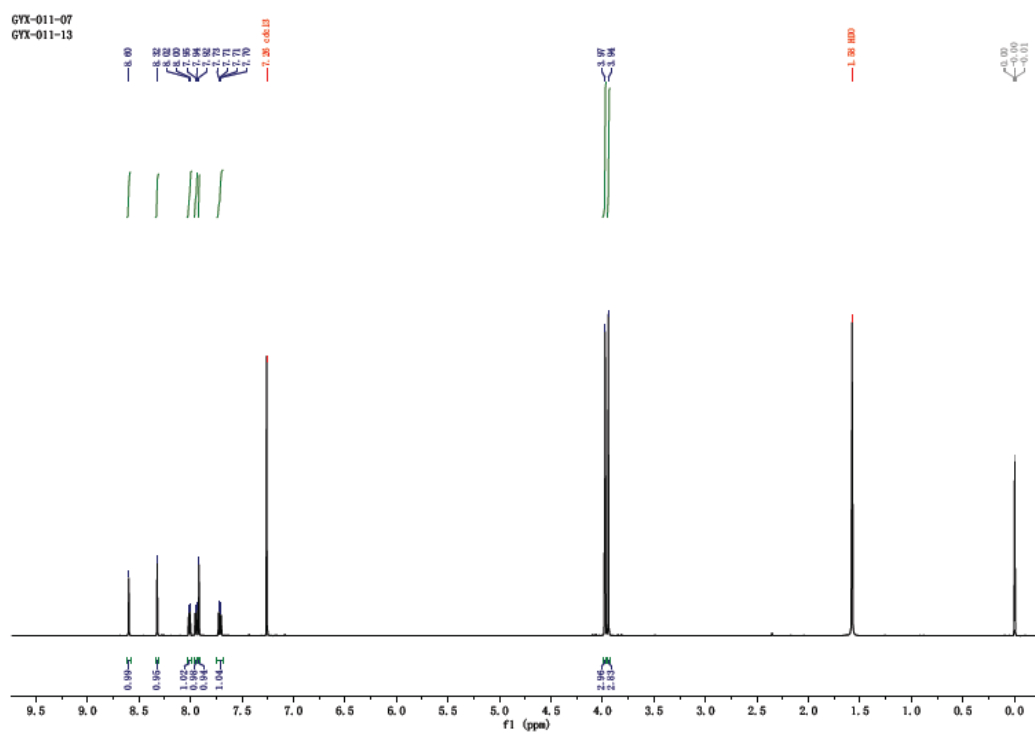


**Fig. S3-1.** (a) <sup>1</sup>H NMR (600 MHz) and (b) <sup>13</sup>C NMR (151 MHz) spectra of **5** (CDCl<sub>3</sub>).

(a)



(b)

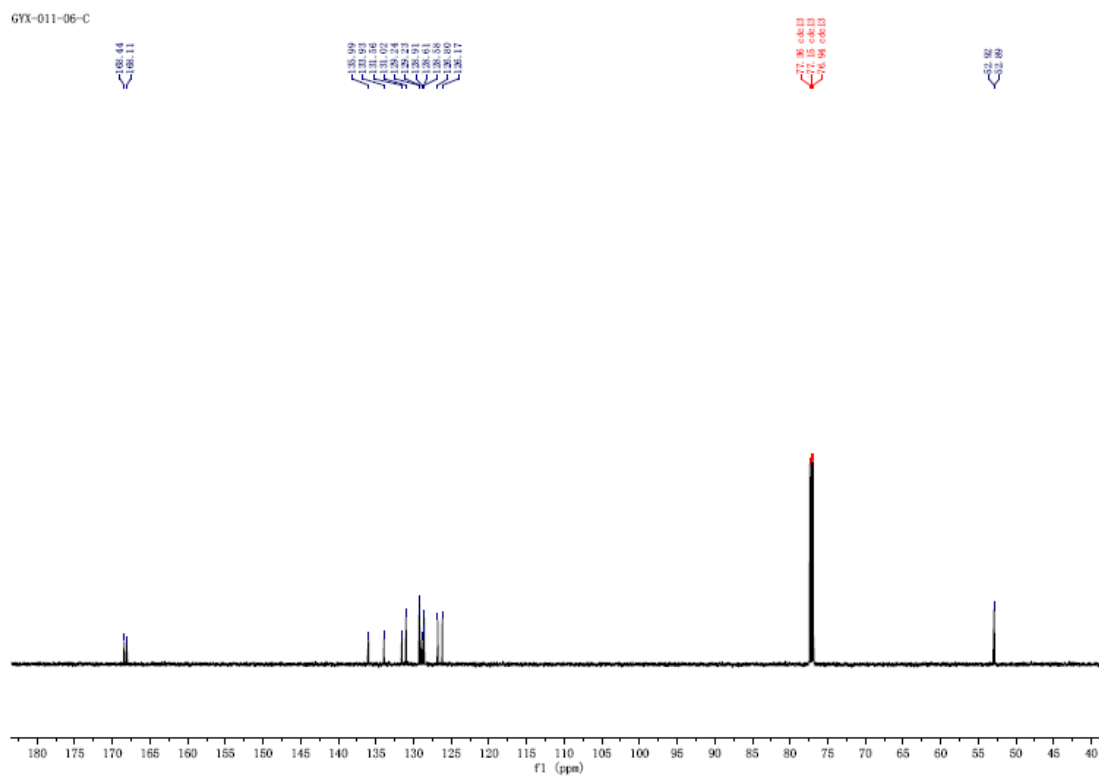
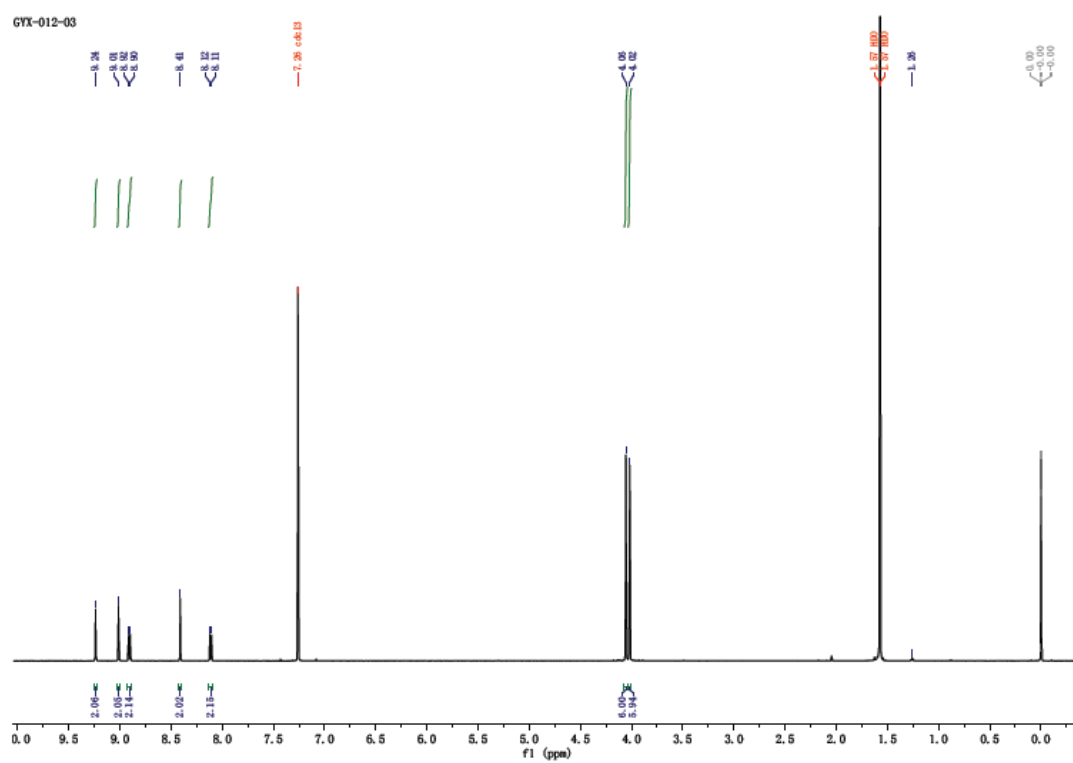


**Fig. S3-2.** (a)  $^1\text{H}$  NMR (600 MHz) and (b)  $^{13}\text{C}$  NMR (151 MHz) spectra of **6** ( $\text{CDCl}_3$ ).

(a)



(b)

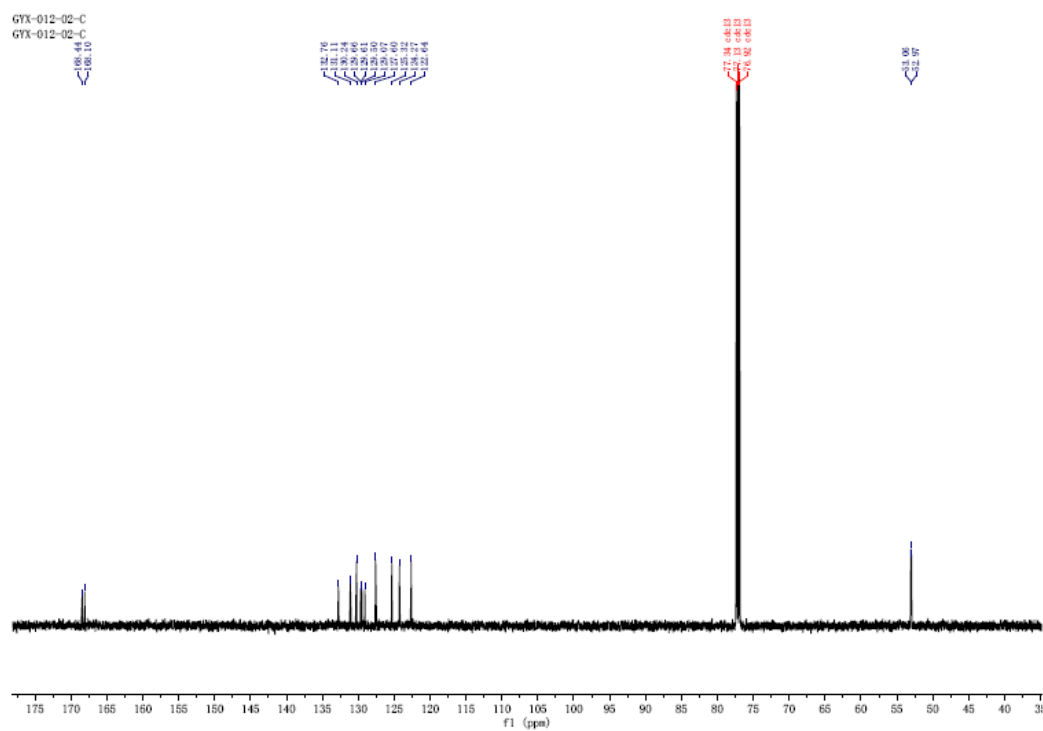


**Fig. S3-3.** (a)  $^1\text{H}$  NMR (600 MHz) and (b)  $^{13}\text{C}$  NMR (151 MHz) spectra of **7** ( $\text{CDCl}_3$ ).

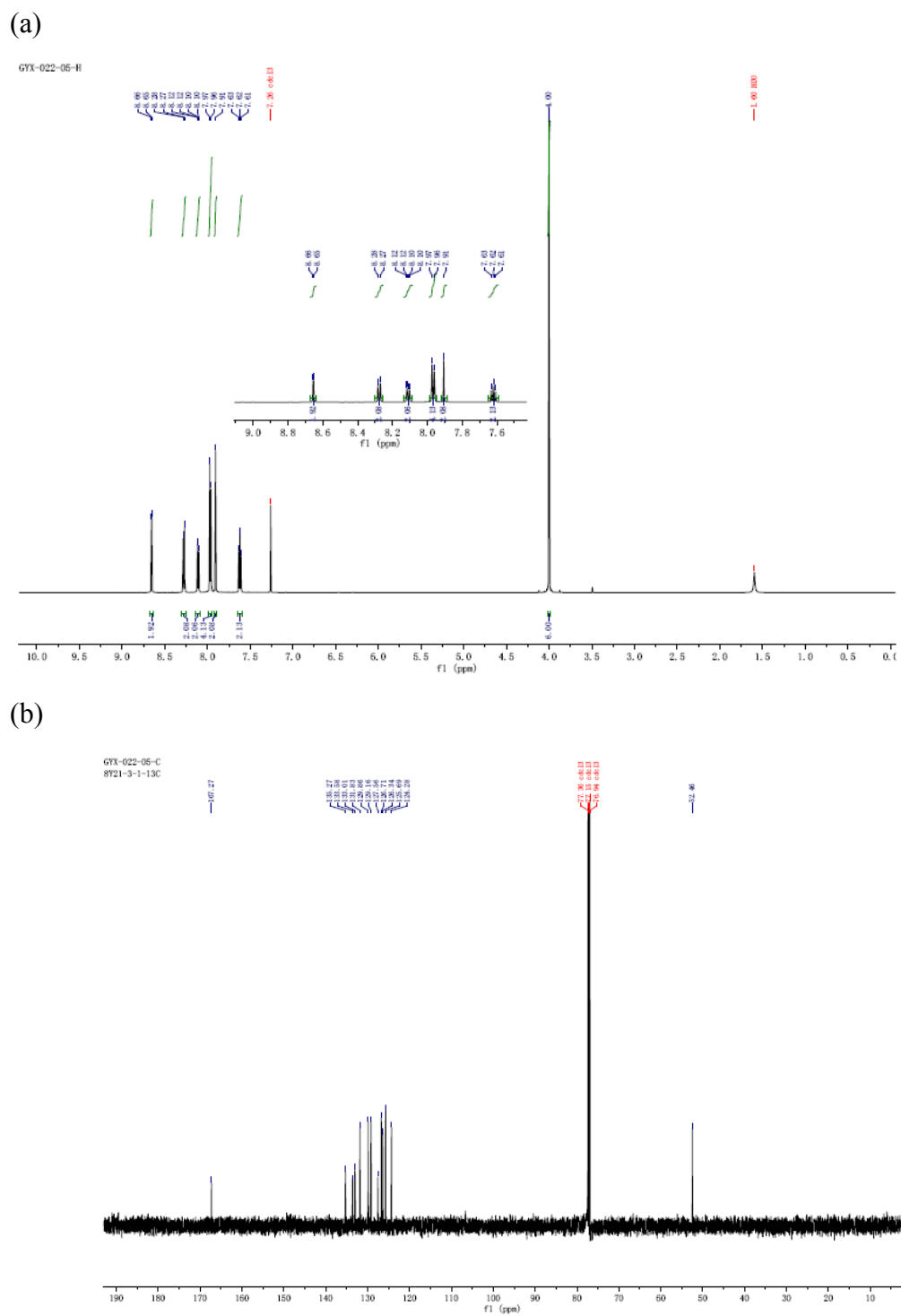


Fig. S3-4. (a)  $^1\text{H}$  NMR (600 MHz) and (b)  $^{13}\text{C}$  NMR (151 MHz) spectra of **9** ( $\text{CDCl}_3$ ).



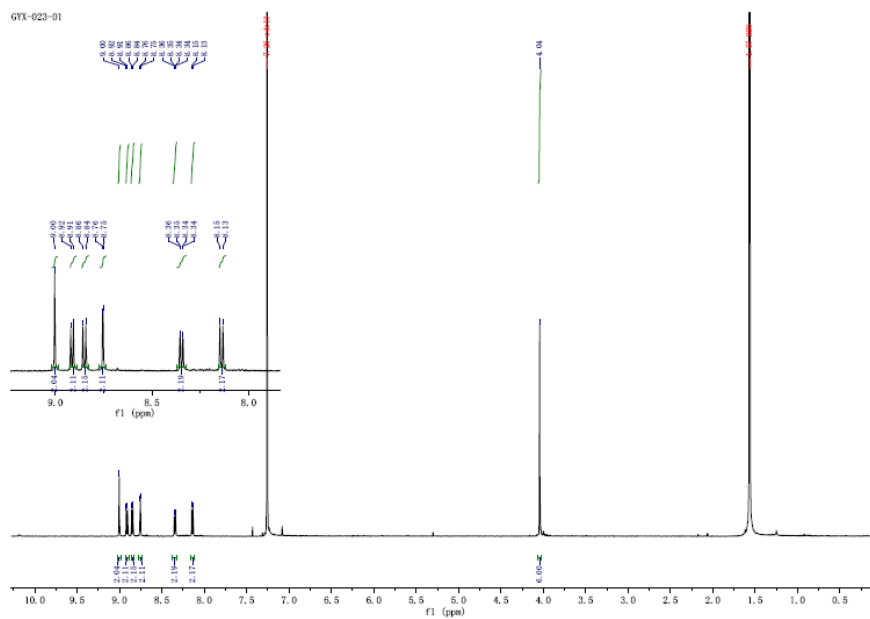


Fig. S3-5.  $^1\text{H}$  NMR (600 MHz) spectra of **10** ( $\text{CDCl}_3$ ).